



Feasibility Study of Cargo Airship Transportation Systems Powered by New Green Energy Technologies

*Jonathan R. Skuza, Yeonjoon Park, Hyun Jung Kim, and Shane T. Seaman
National Institute of Aerospace, Hampton, Virginia*

*Glen C. King and Sang H. Choi
Langley Research Center, Hampton, Virginia*

*Kyo D. Song and Hargsoon Yoon
Norfolk State University, Norfolk, Virginia*

*Kunik Lee
Department of Transportation, McLean, Virginia*

NASA STI Program . . . in Profile

Since its founding, NASA has been dedicated to the advancement of aeronautics and space science. The NASA scientific and technical information (STI) program plays a key part in helping NASA maintain this important role.

The NASA STI program operates under the auspices of the Agency Chief Information Officer. It collects, organizes, provides for archiving, and disseminates NASA's STI. The NASA STI program provides access to the NASA Aeronautics and Space Database and its public interface, the NASA Technical Report Server, thus providing one of the largest collections of aeronautical and space science STI in the world. Results are published in both non-NASA channels and by NASA in the NASA STI Report Series, which includes the following report types:

- **TECHNICAL PUBLICATION.** Reports of completed research or a major significant phase of research that present the results of NASA Programs and include extensive data or theoretical analysis. Includes compilations of significant scientific and technical data and information deemed to be of continuing reference value. NASA counterpart of peer-reviewed formal professional papers, but having less stringent limitations on manuscript length and extent of graphic presentations.
- **TECHNICAL MEMORANDUM.** Scientific and technical findings that are preliminary or of specialized interest, e.g., quick release reports, working papers, and bibliographies that contain minimal annotation. Does not contain extensive analysis.
- **CONTRACTOR REPORT.** Scientific and technical findings by NASA-sponsored contractors and grantees.

- **CONFERENCE PUBLICATION.** Collected papers from scientific and technical conferences, symposia, seminars, or other meetings sponsored or co-sponsored by NASA.
- **SPECIAL PUBLICATION.** Scientific, technical, or historical information from NASA programs, projects, and missions, often concerned with subjects having substantial public interest.
- **TECHNICAL TRANSLATION.** English-language translations of foreign scientific and technical material pertinent to NASA's mission.

Specialized services also include organizing and publishing research results, distributing specialized research announcements and feeds, providing information desk and personal search support, and enabling data exchange services.

For more information about the NASA STI program, see the following:

- Access the NASA STI program home page at <http://www.sti.nasa.gov>
- E-mail your question to help@sti.nasa.gov
- Fax your question to the NASA STI Information Desk at 443-757-5803
- Phone the NASA STI Information Desk at 443-757-5802
- Write to:
STI Information Desk
NASA Center for AeroSpace Information
7115 Standard Drive
Hanover, MD 21076-1320

NASA/TM-2014-218241



Feasibility Study Cargo Airship Transportation Systems Powered by New Green Energy Technologies

*Jonathan R. Skuza, Yeonjoon Park, Hyun Jung Kim, and Shane T. Seaman
National Institute of Aerospace, Hampton, Virginia*

*Glen C. King and Sang H. Choi
Langley Research Center, Hampton, Virginia*

*Kyo D. Song and Hargsoon Yoon
Norfolk State University, Norfolk, Virginia*

*Kunik Lee
Department of Transportation, McLean, Virginia*

National Aeronautics and
Space Administration

Langley Research Center
Hampton, Virginia 23681-2199

April 2014

Acknowledgments

This research was partially supported under the collaborative agreement (IA1-1098) between the National Aeronautics and Space Administration (NASA) Langley Research Center (LaRC) and the Federal Highway Administration, Department of Transportation. The authors appreciate the assistance of various contributors at NASA LaRC: Ashton D. Brown, Robert G. Bryant, Kenneth L. Dudley, Jay J. Ely, Kay V. Forrest, Stephen J. Hales, Jeffrey S. Hill, Joseph Kim, Sandra V. Koppen, Mel H. Lucy, John J. Mielnik, Vernet P. Mull, Truong X. Nguyen, Michael J. Scherner, Rheal P. Turcotte, Erik Vedeler, and Noel J. West.

<p>The use of trademarks or names of manufacturers in this report is for accurate reporting and does not constitute an official endorsement, either expressed or implied, of such products or manufacturers by the National Aeronautics and Space Administration.</p>

Available from:

NASA Center for AeroSpace Information
7115 Standard Drive
Hanover, MD 21076-1320
443-757-5802

Abstract

The development of transportation systems that use new and sustainable energy technologies is of utmost importance due to the possible future shortfalls that current transportation modes will encounter because of increased volume and costs. The introduction and further research and development of new transportation and energy systems by materials researchers at the National Aeronautics and Space Administration (NASA) Langley Research Center (LaRC) and the Department of Transportation are discussed in this Technical Memorandum. In this preliminary study, airship concepts were assessed for cargo transportation using various green energy technologies capable of 24-hour operation (i.e., night and day). Two prototype airships were successfully constructed and tested at LaRC to demonstrate their feasibility: one with commercially available solar cells for operation during the daytime and one with microwave rectennas (i.e., rectifying antennas) developed in-house for night-time operation. The test results indicate the feasibility of a cargo transportation airship powered by new green energy sources and wireless power technology. Future applications will exploit new green energy sources that use materials and devices recently developed or are in the process of being developed at LaRC. These include quantum well SiGe solar cells; low, mid-, and high temperature thermoelectric modules; and wireless microwave and optical rectenna devices. This study examines the need and development of new energy sources for transportation, including the current status of research, materials, and potential applications.

THIS PAGE INTENTIONALLY LEFT BLANK

TABLE OF CONTENTS

SECTION 1	INTRODUCTION	1
SECTION 2	FEASIBILITY STUDY OF CARGO AIRSHIP TRANSPORTATION USING WIRELESS POWER.....	3
SECTION 3	ADVANCES IN WIRELESS POWER TRANSMISSION	19
SECTION 4	FEASIBILITY STUDY OF CARGO AIRSHIP TRANSPORTATION USING SOLAR POWER	24
SECTION 5	RHOMBOHEDRAL EPITAXY OF CUBIC SiGe ON TRIGONAL C-PLANE SAPPHIRE.....	34
SECTION 6	FABRICATION OF RHOMBOHEDRAL SiGe ON SAPPHIRE.....	39
SECTION 7	CHARACTERIZATION OF RHOMBOHEDRAL SiGe ON SAPPHIRE	44
SECTION 8	QUANTUM WELL SOLAR CELL APPLICATIONS.....	50
SECTION 9	HIGH TEMPERATURE THERMOELECTRIC DEVICE APPLICATIONS	55
SECTION 10	LOW TO MID-TEMPERATURE THERMOELECTRICS	58
SECTION 11	THERMOELECTRIC DEVICE APPLICATIONS	75
SECTION 12	SUMMARY.....	79
SECTION 13	REFERENCES	80

LIST OF TABLES

Table 1.	Design parameters of the wireless powered cargo airship as shown in Figure 2.	5
Table 2.	Parameters of the WPT system; the power handling capacity of a Schottky diode is 100 mW for the 10, 45, and 85 GHz frequencies.....	7
Table 3.	Output power of rectenna array patches for various serial and parallel combinations.	15
Table 4.	Prototype cargo airship parameters of a scaled-down 100 ton version (Case 1) and the actual scaled-down version for tests in the reverberation chamber (Case 2)..	16
Table 5.	Rectenna circuit parameters and output voltage and power using a silicon Schottky diode (SMS621–060).....	22
Table 6.	Lifting forces and masses of the various airship components.....	25
Table 7.	Etchant composition of Secco etch-pit density test and its effects (ref. 41).....	45
Table 8.	Estimations of the TE regenerative cycle efficiencies for a three layer tandem system.....	76

LIST OF FIGURES

Figure 1.	Layout and dimensions of the WPT ground stations and the cargo airship flight corridor.	4
Figure 2.	Schematic design of the cargo airship with corresponding dimensions listed in Table 1.	5
Figure 3.	Size of the receiving rectenna array needed to capture the entire dispersed microwave beam as a function of the distance from the transmitting antenna.	8
Figure 4.	Experimental setup for the rectenna array performance test in the anechoic chamber.	9
Figure 5.	Output power of four rectenna arrays measured as a function of frequency and distance from the horn antenna in the anechoic chamber.	10
Figure 6.	Flexible dipole rectenna arrays attached to prototype cargo airship.	10
Figure 7.	HIRF Lab reverberation chamber used to test the prototype WPT cargo airship. ..	11
Figure 8.	Power, voltage, and current output of the rectenna arrays measured as a function of frequency in the reverberation chamber.	12
Figure 9.	Output power of the rectenna arrays measured as a function of input power for the 7.2 and 10.2 GHz maxima. The arrays were measured at a distance of 6 m from the rectangular horn antenna.	13
Figure 10.	The output power of the rectenna array at various incidence angles.	14
Figure 11.	Power characteristics of the rectenna array with various load resistors at 6 m from the horn antenna.	15
Figure 12.	Power output of rectenna array in a 30 percent deflated “flat” condition.	17
Figure 13.	Photos of the flight test inside the reverberation chamber with WPT.	18
Figure 14.	S11 parameter of dipole rectenna versus frequency for various widths of the antenna and a schematic diagram of a rectenna design.	20
Figure 15.	45 GHz Schottky diode.	21
Figure 16.	Power conversion efficiency of a rectenna with various Schottky diode resistances.	21
Figure 17.	V-band rectenna.	22
Figure 18.	Simulations of a Schottky diode assembly on a V-band rectenna array.	23
Figure 19.	Fabricated Schottky diode assemblies on a V-band rectenna array.	23
Figure 20.	View of the airship with its dimensions.	24
Figure 21.	View of the top of the airship with the approximation for the lift calculation.	25
Figure 22.	Bridle strap locations on the helium envelope for securing the airship during fabrication and testing (55 lb) and attaching the gondola (35 lb).	25
Figure 23.	Current-voltage (I-V) data (red) and best fit (black) for the 24-cell solar panels tested in ambient sunlight conditions.	26
Figure 24.	Dark I-V curve used to approximate the values of R_s and R_{sh}	27
Figure 25.	3-D rendered top view of the semi-production model of the solar powered cargo airship prototype.	28
Figure 26.	Propulsion gondola module with four variable angle main propellers and two fixed side propellers.	28
Figure 27.	2-D CAD view of the front side of airship with the vertical weight distribution.	29
Figure 28.	Joint and supporting aluminum blocks for servos and gears.	29
Figure 29.	Location of each motor, ESC, servo, and gear box.	30
Figure 30.	Propulsion and flight control system diagram with 14 channels.	31
Figure 31.	The fully assembled solar powered cargo airship prototype attached to its support structure.	32
Figure 32.	Scene from video of the indoor flight test of the solar airship.	32

Figure 33.	Bandgap engineering diagrams and epitaxy schemes for cubic, hexagonal, and rhombohedral crystal systems (ref. 34).	34
Figure 34.	Rhombohedral hybrid band-gap engineering diagram shown in Figure 33.	35
Figure 35.	Crystallographic alignment of a cubic (111) crystal on a trigonal (0001) substrate (ref. 36).	36
Figure 36.	Crystal structures and relationships (ref. 37).	36
Figure 37.	Rhombohedrally grown single crystalline SiGe on trigonal c-plane sapphire.	38
Figure 38.	Three-dimensional CAD design of the SOA e-beam growth chamber.	39
Figure 39.	Three-dimensional rendered CAD view of the SOA e-beam growth chamber.	40
Figure 40.	Photograph of the SOA e-beam growth chamber.	40
Figure 41.	Dual rotation substrate heater module with entry/exit flanges for load-lock assembly.	41
Figure 42.	Various components of the e-beam growth chamber.	42
Figure 43.	Fabricated rhombohedral SiGe samples on 6 inch c-plane sapphire wafers. A quarter dollar coin is shown for size comparison.	42
Figure 44.	Symmetric θ -2 θ XRD scan shows only the SiGe (111) reflection at $2\theta \sim 27.5$ degrees along with the Al_2O_3 (003), (006), (009), and (0012) reflections. SiGe (220) ϕ scan shows three strong reflections (offset by 120 degrees) with three small reflections rotated 60 degrees from them indicating greater than 99.5 percent in-plane orientation of the SiGe.	44
Figure 45.	Four Secco etch-pit density tests on rhombohedral SiGe grown on c-plane sapphire, where etch-pits (red circles) exist but line dislocations do not.	46
Figure 46.	Secco etch-pit test results.	46
Figure 47.	Photograph of ~ 100 nm thick SiGe samples with mirror-like surfaces.	47
Figure 48.	Cross-sectional SEM images of a smooth SiGe layer on c-plane sapphire in layer-by-layer growth mode and a rough SiGe layer on c-plane sapphire in SK growth mode. The SK growth mode begins layer-by-layer and transitions to coherent 3-D island growth at a critical thickness.	48
Figure 49.	AFM images of bare c-plane sapphire and different thicknesses of rhombohedral SiGe layers on c-plane sapphire.	49
Figure 50.	Quantum well structure of SiGe (left) and the mobility enhancement of electrons and holes in a QW (ref. 42 and 43).	52
Figure 51.	Energy absorption regimes of silicon and germanium solar cells with respect to the solar spectra.	53
Figure 52.	Rhombohedral SiGe on c-plane sapphire and transparent double-side polished sapphire wafer (inset).	53
Figure 53.	Comparison of a conventional silicon solar cell that receives sunlight from the front side where electrodes shadow sunlight and a rhombohedral SiGe solar cell on c-plane sapphire that receives sunlight from rear side with no obstructing electrodes.	54
Figure 54.	SiGe/Sapphire/GaN hybrid crystal structure device on a double-sided sapphire wafer with illumination from each side.	54
Figure 55.	XRD pole figures on the SiGe (220) reflection for two SiGe materials with different crystalline qualities.	55
Figure 56.	TE FoM equation and the historical development of TE materials at various operating temperature regimes (ref. 46).	56
Figure 57.	Thermal conductivity is lowered by phonon scattering at the stacking-fault interface of a twin crystal.	57
Figure 58.	Electrical mobility of fabricated twinned $\text{Si}_{1-x}\text{Ge}_x$ samples with respect to bulk SiGe. An increase in the electrical conductivity leads to an increase in ZT (ref. 47 and 48).	57

Figure 59.	The efficiency of current power generating systems and their improvement of generating efficiency assuming the additional use of TE systems with 20 percent efficiency (ref. 49).	58
Figure 60.	The Lawrence Livermore National Laboratory's finding during their 2008 study of energy use (ref. 51).....	59
Figure 61.	Optimizing ZT through carrier concentration tuning. Maximizing the efficiency (ZT) of a thermoelectric involves a compromise of increasing the Seebeck coefficient and electrical conductivity, while decreasing the thermal conductivity (ref. 52).	60
Figure 62.	Current values and expected achievements after five years of the nondimensional power generating performance index (ZT) of low temperature (red), mid-temperature (orange), and high temperature (blue) TE conversion materials (ref. 49).	61
Figure 63.	NASA developed TE material design by decorating grains with metallic nanoparticles in order to increase the Seebeck coefficient and electrical conductivity, while decreasing the thermal conductivity to increase the TE FoM. .	62
Figure 64.	Two procedures for synthesizing Bi_2Te_3 crystals (ref. 55).	63
Figure 65.	The solvothermally synthesized Bi_2Te_3 powders.	64
Figure 66.	Surface morphologies of the Bi_2Te_3 grains covered with nanoparticles.	65
Figure 67.	(a) The Seebeck coefficient, (b) the electrical conductivity, (c) the power factor, (d) the thermal conductivity, and (e) the dimensionless FoM of Bi_2Te_3 samples decorated with 0.001 wt percent / 0.05 wt percent Au or 0.05 wt percent Ag metallic nanoparticles using Bi_2Te_3 as the starting material at room temperature. (f) The dimensionless FoM of nanocomposite samples (NC1, NC2) and zone-melted (ZM) sample (ref. 57) compared with data measured for Bi_2Te_3 samples decorated with Au and Ag nanoparticles (blue and red triangles, respectively).	66
Figure 68.	Synthetic process of Ag_2Te grains whose surfaces are covered with metallic bismuth nanoparticles.	67
Figure 69.	(a) A cleavage surface SEM image of the Ag_2Te grain covered by bismuth metallic nanoparticles, (b) BSE image, (c) HAADF STEM image (red circle: EDS point analysis area), (d) EDS spectra of nanoparticle (red circle area in c), (e) HRTEM image of nanoparticles, and (f) BF TEM image of the Ag_2Te grain covered by bismuth metallic nanoparticles.	68
Figure 70.	Temperature dependencies of electrical conductivity (σ).	69
Figure 71.	Temperature dependencies of various TE parameters for a Ag_2Te sample decorated with Bi-rich metallic nanoparticles. The purple data indicated at room temperature is cited from Borca-Tasciuc et al. (ref. 61).	70
Figure 72.	Concept for TE ink for airship application.	72
Figure 73.	SEM images and photos for Bi_2Te_3 / epoxy resin, Bi_2Te_3 / polystyrene (PS), Bi_2Te_3 / PMMA, and Bi_2Te_3 / polyaniline (PAN) composites.	72
Figure 74.	Material properties of printed TE composites at 300 K (ref. 62).	74
Figure 75.	TE tandem system block diagram showing the potential energy savings assuming a 30 percent conversion efficiency of waste heat at each TE layer.	75
Figure 76.	3-D conceptual view of an advanced TE device in a tandem arrangement.	75
Figure 77.	Possible economic impacts of more efficient TE device technology.	77
Figure 78.	A new concept powertrain that recoups and converts wasted thermal energy into useful electrical energy.	78

Nomenclature

A	amps
AC	alternating current
AES	Auger electron spectroscopy
AFM	atomic force microscope
BF	bright field
BSE	backscattered electron
C	Celsius
CAD	computer aided design
CF	conflat
cm	centimeters
CMOS	complementary metal-oxide-semiconductor
CNT	carbon nanotubes
cps	counts per second
C&I	Creativity and Innovation
dB	decibels
DC	direct current
DoF	degrees of freedom
e-beam	electron beam
EDS	energy dispersive spectroscopy
EM	electromagnetic
EMF	electromotive force
ESC	electronic speed controller
fcc	face centered cubic
FE	field emission
FFT	fast Fourier transform
FM	frequency modulation
FoM	figure of merit
g	grams
GHz	gigahertz
GPS	global positioning system
h	hour
HAADF	high-angle annular dark field
HDR	high dynamic range
HF	hydrofluoric acid
HIRF	high intensity radiated fields
hp	horsepower

HRTEM	high resolution transmission electron microscope
IC	integrated circuit
IMU	inertia motion unit
I-V	current voltage
K	Kelvin
keV	kiloelectron volt
kg	kilogram
kHz	kilohertz
km	kilometers
kW	kilowatts
LaRC	Langley Research Center
lbs	pounds
LD	line dislocation
LED	light emitting diode
LEED	low energy electron diffraction
m	meters
mA	milliamps
MFP	mean free path
MHz	megahertz
mW	milliwatt
NASA	National Aeronautics and Space Administration
NC	nanocomposite
nm	nanometer
NW	northwest
OD	outer diameter
PE	polyethylene
PET	polyethylene terephthalate
PID	proportional integral derivative
PP	polypropylene
Q	amount of heat
QW	quantum well
RF	radio frequency
RFA	retarding field analyzer
RHEED	reflection high energy electron diffraction
RMS	root mean square
rpm	revolutions per minute
RTG	radioisotope thermoelectric generator

R/C	radio controller
R&D	research and development
s	second
SAED	selected area electron diffraction
SE	southeast
SEM	scanning electron microscope
SK	Stranski-Krastanov
SOA	state-of-the-art
SOI	silicon on insulator
SOS	silicon on sapphire
SSP	single side polished
STI	scientific and technical information
TDP	threading dislocation pit
TE	thermoelectric
TED	transmission electron diffraction
TEM	transmission electron microscope
TM	technical memorandum
TW	terawatt
TWT	travelling wave tube
UHV	ultrahigh vacuum
Ultra-CMOS	ultra-complementary metal-oxide-semiconductor
U.S.	United States
V	volts
VGA	video graphics array
VTOL	vertical takeoff and landing
W	watts
WPT	wireless power transmission
XRD	x-ray diffraction
ZM	zone-melted
°	degrees
,	feet
”	inches
2-D	two-dimensional
3-D	three-dimensional
A_{rec}	area of receiving antenna aperture
A_{trans}	cross-sectional area of transmitted beam
C_0	zero bias junction capacitance

D	directivity
η	efficiency
η_{beam}	beaming efficiency
η_C	Carnot efficiency
η_{TE}	thermoelectric efficiency
θ	half power beamwidth
F_C	cutoff frequency
I_{SC}	short circuit current
κ	thermal conductivity
λ	wavelength
m	mass
μm	micrometer
μV	microvolt
P	power
R	distance between transmitting and receiving antenna apertures
R_L	load resistance
R_S	series resistance
R_{SH}	shunt resistance
ρ_{air}	density of air at airship cruising altitude
ρ_{He}	density of helium
ρ_{sea}	density of air at sea level
S	Seebeck coefficient
$S^2 \sigma$	electrical power factor
σ	electrical conductivity
T_C	cold temperature
T_H	hot temperature
τ	beaming efficiency
v	speed
V	volume
V_B	breakdown voltage
V_{bi}	diode junction voltage
V_{OC}	open circuit voltage
V_0	output voltage
Z	thermoelectric figure of merit or average proton number
ZT	dimensionless thermoelectric figure of merit
Ω	Ohms

SECTION 1 INTRODUCTION

The development of radically new and sustainable transportation modes for both passengers and cargo is absolutely necessary due to (i) a continuous increase in transportation numbers and volumes from the expansion of commercial activities, (ii) a fast growing and spreading urbanization, (iii) a saturated state of current transportation systems and infrastructures, and (iv) an increasing concern for environmental issues with currently dominant petroleum-based transportation systems. Accordingly, transportation safety and mobility have become critical issues that need to be resolved using new technologies. The anticipated development of new transportation systems will require substantial future investments in entirely new energy sources and infrastructures, along with smart and intelligent transportation system networks.

The timely adoption of new green energy sources will slowly diminish the dominance of petroleum-based power plants for transportation systems. The possibility also exists to alleviate onboard power generation systems by alternatively using wireless power transmission (WPT) technology. However, green energy technologies are not yet fully developed and cannot harness sufficient amounts of energy to compete with existing petroleum-based systems. Therefore, research and development (R&D) of these technologies must be accelerated in order to offset the approximately \$1 trillion spent annually in the United States (U.S.) on fossil fuel energy consumption (ref. 1), which accounts for 82 percent of the total energy consumption in the U.S. (ref. 2). However, almost all (95.5 percent) of the energy for the transportation sector comes from fossil fuels (ref. 2), thus the transportation sector accounts for just over one-fourth of the total fossil fuel consumption in the U.S. (ref. 2). Furthermore, approximately \$300 billion of fossil fuels are imported annually from foreign countries (ref. 2). The development of new green energy technologies, not only for transportation but also for other needs, will eventually allow the U.S. to become more self-reliant for its energy needs and continue a healthy and strong economic leadership in the world.

One such new transportation system that will use these sources of clean and efficient energy are cargo airships that can easily overcome common barriers to cargo traffic. For example, rivers, valleys, canyons, and mountains require costly construction of bridges, tunnels, or roads. These cargo airships would be fully powered by green energy sources, thus alleviating reliance on fossil fuels. They would be able to primarily transport several 40 ft cargo containers, offering complementary solutions to current transportation demands and creating delivery solutions that were once previously nonexistent.

This National Aeronautics and Space Administration (NASA) Technical Memorandum (TM) discusses the feasibility of these cargo airship transportation systems using currently available green energy technologies: WPT in the X-band and solar energy using monocrystalline silicon (Si) cells. The discussion continues with the R&D of existing and new green energy technologies in order to improve their efficiencies for use on these cargo airships and other transportation systems. Langley Research Center (LaRC) has complete in-house fabrication and characterization facilities to push these technologies to their theoretical limits, which include rhombohedral SiGe (silicon germanium) to capture solar energy with quantum well (QW) solar cells and waste heat energy with high temperature thermoelectric (TE) materials combined in a tandem TE device with other low and mid-temperature TE materials decorated with metallic

nanoparticles, and an advanced WPT device in the microwave regime beyond the X-band (i.e., from the K-band through the W-band).

SECTION 2

FEASIBILITY STUDY OF CARGO AIRSHIP TRANSPORTATION USING WIRELESS POWER

The feasibility of using an airship to transport heavy cargo loads is examined and three primary design constraints are identified: (i) the propulsion system, (ii) the power supply, and (iii) the flight path. The selection of these criteria will determine further parameters of the cargo airship, such as its physical size, cargo load capabilities, etc.

An ideal propulsion system for an airship that is carrying many metric tons of cargo should have electrically powered propellers, which are highly efficient for low speed flight applications (ref. 3). These electric motors would be powered using a WPT system that would alleviate any onboard power generation systems. This concept of harvesting power wirelessly is envisioned as one of the best options to alleviate the complexity associated with hard-wired control circuitry in propulsion systems. This is accomplished through a rectifying antenna or "rectenna," which consists of a dipole antenna with a diode connected across its elements. The diode rectifies the alternating current (AC) induced in the dipole antenna from the electromagnetic (EM) waves to create direct current (DC) power.

William C. Brown developed microwave WPT technology in the 1960s (ref. 4). His research demonstrated power transmission using EM waves and the subsequent rectification to DC power. However, Nikola Tesla conceived of and demonstrated the fundamental idea for WPT (ref. 5–7), whereby he used a coil that was connected to a 60 m tower and fed by a 1300 kW, 150 kHz power source. The realization that higher frequency EM waves (i.e., microwaves) were necessary to effectively focus those waves towards the power receiver was then made. Therefore, it is important to consider high frequency amplifiers for the WPT. Albert W. Hull invented the magnetron in 1921 (ref. 8) to amplify microwaves, and in 1937 the Varian brothers (Russell H. and Sigurd F.) fabricated the klystron, which was based on the original idea by the Heil brothers (A. Arsenjewa and Oskar) (ref. 9). In 1964, Brown gave the first historical demonstration of WPT in the frequency range of 2.4–2.5 GHz for a helicopter (ref. 10). A power conversion device, called a rectifying antenna or rectenna for short, was developed and used for these helicopter demonstrations. Later, semiconductor diodes were replaced by Si Schottky diodes that raised the microwave to DC conversion efficiency from 40 percent to 80 percent. WPT was continually developed for solar power satellites in 1978 (ref. 11) for the Next Generation Space Telescope (now known as the James Webb Space Telescope) in 1996 (ref. 12) and was applied to smart actuators (ref. 13–15), and to medical applications (ref. 16–19). WPT is a proven technology; however, more studies are required to target specific applications, such as the development of rectenna elements for maximum density, conversion efficiency, and higher frequencies, the development of Schottky diodes for higher breakdown voltages, as well as the design of robust rectenna patch arrays and their integration into surfaces (e.g., airships) (ref. 20) for optimized boundary layer air flow.

EM waves are collected through a high resonance antenna and delivered to a Schottky diode to obtain high efficiencies (ref. 21) where the Schottky diode rectifies the alternating current (AC) power into DC power. Rectenna arrays can attain high power transfer capacity from radiated EM energy sources by connecting the rectennas in series, parallel, or combination of both, as well as by enlarging the receiving area. The configuration of the rectennas in the array can be altered for

specific applications. Parallel connections are preferred over serial connections for high current applications, such as operating motors that require a high level of instantaneous torque (ref. 22). This is because the current passing through a Schottky diode is only in the range of a few hundred milliamps. Consequently, the output power from a serial connection would be limited to within one watt for an electric motor with a load resistance of a few ohms. Therefore, serial and parallel connection combinations are essential to increase the current for high current operations.

The cargo airship would have rectenna arrays populated over the surface of its membrane in order to receive the transmitted wireless microwave power from ground power stations. The positioning of these ground power transmission stations would determine the flight path of the cargo airship. The altitude for the flight operation of the airship was chosen to be less than 2.5 km within a flight corridor width of 4 km between two rows of power transmission stations. Figure 1 shows the overall positioning of these ground power stations and the flight corridor. The cargo airship receives wireless power from the four nearest transmission stations, so when the airship passes through the imaginary boundary between two beaming stations, the next pair of stations take over for uninterrupted power transmission. The airship flight range would be limited to within 1 km from the midline separating the two rows of power stations as indicated in Figure 1 for stable power delivery and flight control. These conditions, along with the size of the cargo airship and WPT conditions (i.e., frequency, antenna size, rectenna array size, etc.), allow a maximum power reception distance R of approximately 4.4 km between the transmitting antennas and rectenna arrays operating at 10 GHz.

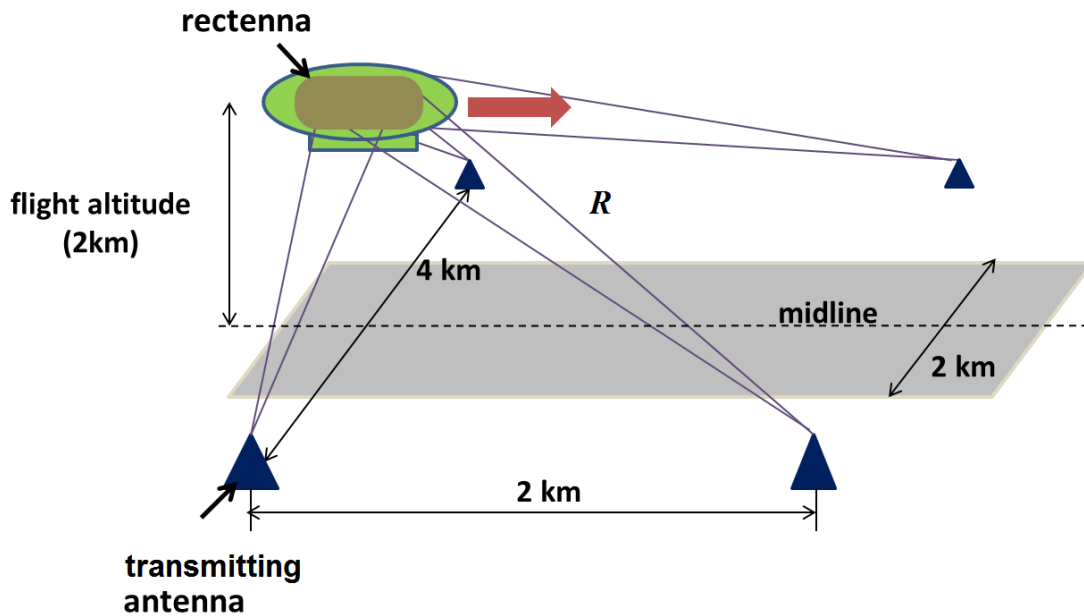


Figure 1. Layout and dimensions of the WPT ground stations and the cargo airship flight corridor.

The physical dimensions of the cargo airship and the amount of energy needed for its propulsion can be determined based on the design constraints set previously. In this preliminary study, two different scenarios of airship operation based on cargo payload were investigated: (i) 100 metric

tons and (ii) 400 metric tons. The design parameters are calculated below for the 100 metric ton payload.

The volume of the cargo airship V needed to lift a payload mass m is calculated using the reduced density of air ρ_{air} at a specified altitude and the density of helium ρ_{He} using equation (1):

$$V = \frac{m}{\rho_{air} - \rho_{He}} \quad (1)$$

A total volume of approximately $1.5 \times 10^5 \text{ m}^3$ is necessary in order to transport 100 metric tons of cargo payload at a cruising altitude of 2.5 km. The mass of the airship itself is estimated to be about 20 metric tons with the conceptual design shown in Figure 2 and the parameters listed in Table 1.

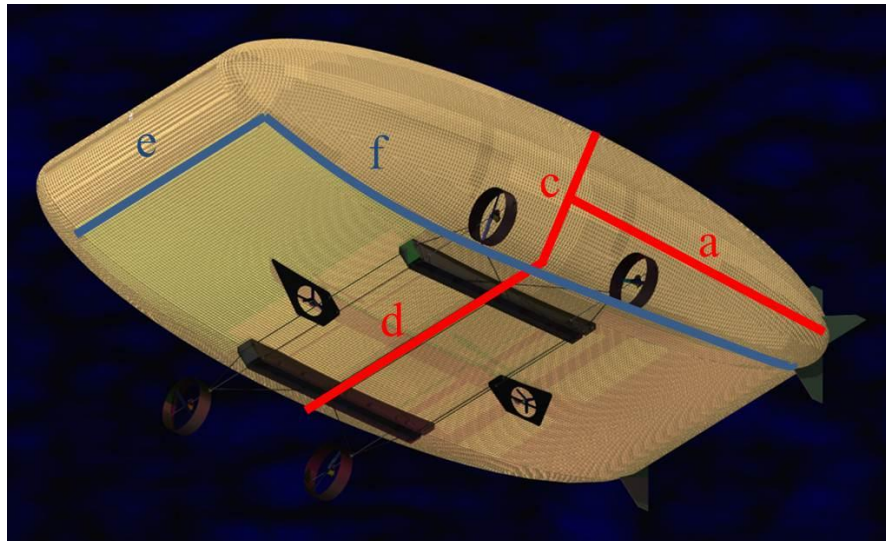


Figure 2. Schematic design of the cargo airship with corresponding dimensions listed in Table 1.

Table 1. Design parameters of the wireless powered cargo airship as shown in Figure 2.

Design Parameters		Cargo Payload	
		100 ton	400 ton
Weight of unloaded airship		20 ton	80 ton
Cruise Speed		70 km/hour	
Airship volume		$1.5 \times 10^5 \text{ m}^3$	$6.0 \times 10^5 \text{ m}^3$
Airship Dimensions	Length, $2a$	145 m	230 m
	Height, c	25 m	40 m
	Width, d	60 m	96 m
	Width of bottom rectenna area, e	35 m	56 m
	Length of bottom rectenna area, f	116 m	184 m
Required total power		825 kW	1,895 kW
Effective area for rectenna		9,656 m^2	24,515 m^2
Required power density		85 W/m^2	77 W/m^2

The propulsion power for the cargo airship was analyzed following Lorenz's study (ref. 23), where airships ranging in size from small radio-controlled ones to ones the size of the Zeppelin were analyzed as a function of their mass and maximum speed. The propulsion power P can be calculated as given in equation (2):

$$P = 3m^{0.6}v^{1.85}\left(\frac{\rho_{air}}{\rho_{sea}}\right)^{0.33-0.5\eta} \quad (2)$$

where m is the airship mass, v is the speed of the airship, ρ_{air} is the density of the air at the cruising altitude, ρ_{sea} is the density of air at sea level, and η is the efficiency of electric power propeller propulsion system (ref. 24). The required electrical power for this 120 metric ton cargo airship is 825 kW, assuming a flight speed of 70 km/h at an altitude of 2 km. The electrical to mechanical power conversion efficiency for the electric motors η was assumed to be a conservative value of 80 percent (ref. 25). The electrical power for the motors is wirelessly transmitted from the ground power stations to the rectenna arrays that are attached on the outside bottom (80 percent coverage) and sides (60 percent coverage) of the airship surface as shown in Figure 2. The power efficiency for cargo airship operation increases with the airship size and cargo payload, as can be seen from equation (2) and shown in Table 1 (ref. 23 and 26).

The overall architecture of the WPT system can now be designed since the power and power density requirements have been set for both 100 and 400 metric ton cargo airships. The cross-sectional area A_{trans} of the WPT beam can be calculated using the Goubau relationship (ref. 27) as in equation (3):

$$A_{trans} = \frac{\tau \lambda^2 R^2}{A_{rec}} \quad (3)$$

where τ is the beaming efficiency between the transmitting and receiving antenna apertures and equals three for 100 percent efficiency, λ is the wavelength of the EM waves, R is the distance between the transmitting and receiving antenna apertures, and A_{rec} is the area of the receiving antenna aperture (i.e., the rectenna arrays on the airship). The distance between the transmitting antenna and receiving rectenna arrays R meets the far-field condition leading to equation (4):

$$D = \frac{4\pi A_{trans}}{\lambda^2} \quad (4)$$

where D is the directivity. Therefore, the number of transmitting antenna arrays should be 80×80 to obtain a directivity D of 43 dB for 10 GHz operation. The half-power beamwidth θ is calculated as 1.26° using equation (5):

$$\theta \approx \sqrt{\frac{32000}{D}} \quad (5)$$

As shown in Table 2, WPT systems are outlined for different microwave frequencies of 10, 45, and 85 GHz. The power attenuation by oxygen and water molecules in the atmosphere near 45 GHz is much lower than either the K_a-band or V-band frequencies and, therefore, is regarded as an important factor for long distance WPT. The areas of the rectenna unit cells and the number of Schottky diodes can be calculated as shown in Table 2 for the 10, 45, and 85 GHz frequencies.

Power conversion efficiencies of 80, 60, and 40 percent are assumed in this study for 10, 45, and 85 GHz, respectively, based on previous research (ref. 28–30). The power transmission flux density from the 10 GHz system is calculated to be 89 W/m^2 , which meets the required powers of 85 W/m^2 and 77 W/m^2 for the operation scenario of cargo airships with respective payloads of 100 and 400 tons at cruising speeds of 70 km/h. In the case of 45 GHz, the power receiving capacity of $1,350 \text{ W/m}^2$ far exceeds the requirement of 77 W/m^2 , which means that the rectenna array area can be reduced to 6.3 percent (approximately one-sixteenth) of the size for the array needed for 10 GHz operation. Correspondingly for 85 GHz, the rectenna array area can be much further reduced to 2.6 percent (approximately one thirty-eighth) of the size compared to 10 GHz operation.

Table 2. Parameters of the WPT system; the power handling capacity of a Schottky diode is 100 mW for the 10, 45, and 85 GHz frequencies.

Frequency	10 GHz	45 GHz	85 GHz
Area of rectenna unit cell	$9.0 \times 10^{-4} \text{ m}^2$	$4.4 \times 10^{-5} \text{ m}^2$	$1.2 \times 10^{-5} \text{ m}^2$
Number of Schottky diodes per m^2	1,111	22,500	80,278
Power conversion efficiency of rectenna	80%	60%	40%
Power attenuation at the maximum distance	0.04 dB	0.35 dB	0.35 dB
Power flux density	89 W/m^2	$1,350 \text{ W/m}^2$	$3,211 \text{ W/m}^2$

The receiving area of these rectenna arrays (i.e., an antenna) can be estimated for a certain power density using the Goubau relationship (ref. 27) as in equation 3. The footprint of the microwave beam (i.e., the size of the rectenna array needed to capture the entire dispersed transmitted microwave beam) at various distances from the 0.2 m diameter transmitting antenna can be calculated for various frequencies as shown in Figure 3 assuming 100 percent efficiency. The dispersion of the microwave beam decreases as the frequency is increased as indicated in the graph, and is the reason for the dramatic increase in power flux density of higher frequency microwaves.

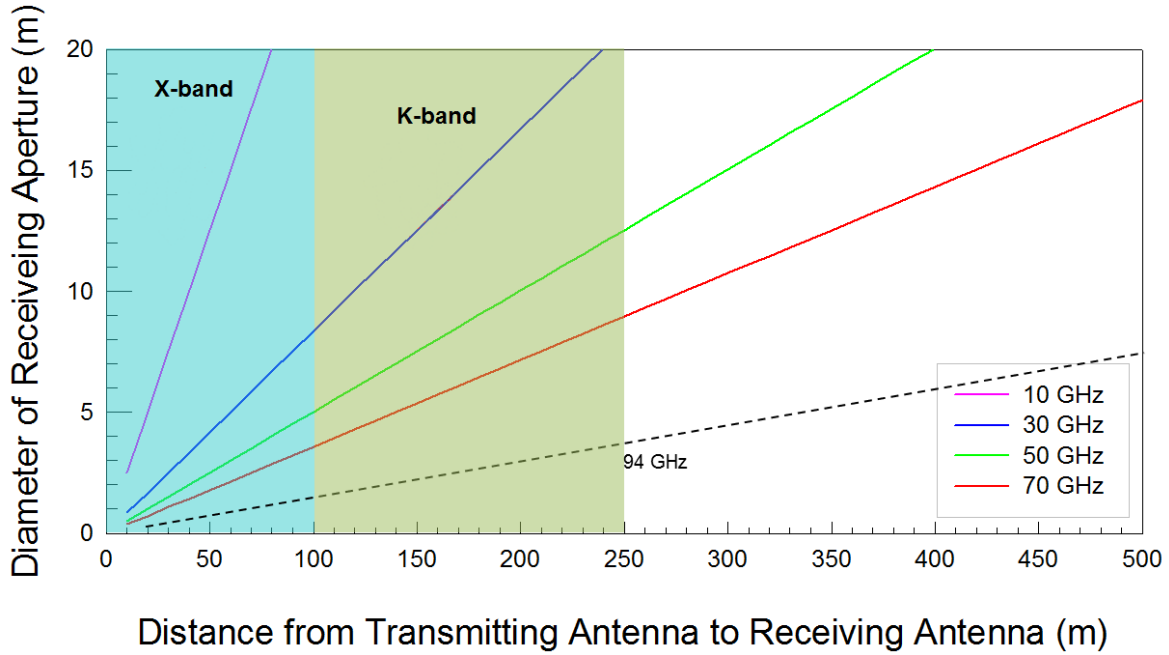


Figure 3. Size of the receiving rectenna array needed to capture the entire dispersed microwave beam as a function of the distance from the transmitting antenna.

A feasibility test using a 7.5 foot prototype cargo airship powered by novel flexible rectenna arrays optimized for 10 GHz was performed in order to evaluate the WPT system that has been previously devised and outlined. Individual X-band rectenna arrays were fabricated and tested in a $4 \times 4 \times 8$ foot anechoic chamber with a setup as shown in Figure 4. A signal generator (HP-8672A) and amplifier (VZX-6983-G5GLM, TWT, Varian) provided 200 W of microwave power input within a frequency range of 7–18 GHz. The 200 W of microwave power was delivered through a travelling-wave tube (TWT) waveguide connected to a Narda rectangular horn antenna for irradiating the rectenna arrays. The flexible rectenna arrays were connected to a power measurement system that was located outside of the anechoic chamber by means of a dual output BNC connector in order to measure the output voltage and current. The distance between the horn antenna and the rectenna arrays was varied between 10–70 inches.

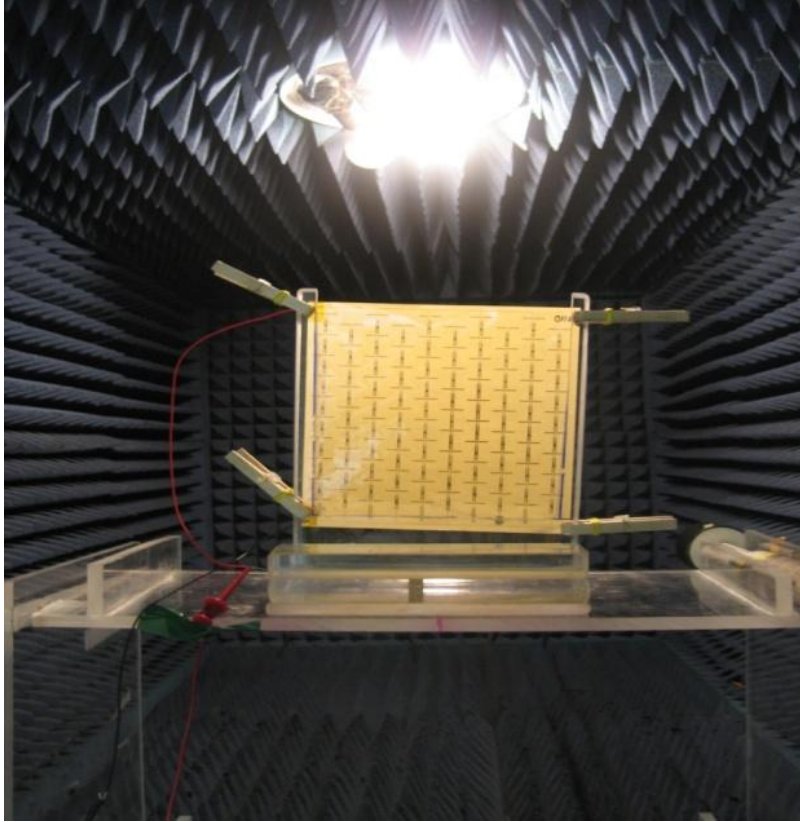


Figure 4. Experimental setup for the rectenna array performance test in the anechoic chamber.

The performance of approximately 600 rectenna arrays ($18\text{ cm} \times 19.5\text{ cm}$) optimized for 10 GHz was evaluated within this anechoic chamber as described above with typical results shown in Figure 5. Four rectennas were used in these performance tests (see inset of Figure 5), where the output power was measured as a function of frequency and distance from the horn antenna. A $3.5\ \Omega$ load resistance was used to match the resistance value of the propeller motors from the prototype cargo airship for these measurements. The 32 best performing rectenna arrays from these tests were attached to the prototype cargo airship (i.e., 16 on the port side and 16 on the starboard side) as shown in Figure 6.

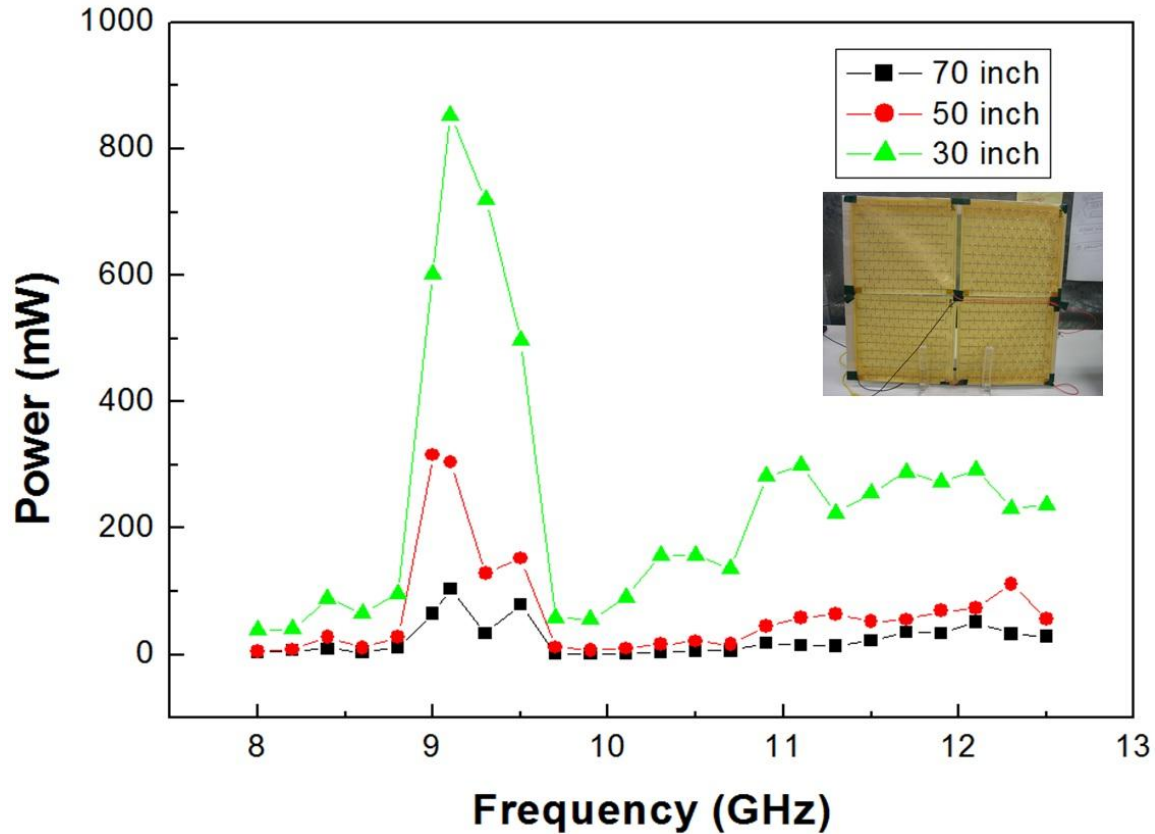


Figure 5. Output power of four rectenna arrays measured as a function of frequency and distance from the horn antenna in the anechoic chamber.



(a) Flexible dipole rectenna array.



(b) Prototype cargo airship.

Figure 6. Flexible dipole rectenna arrays attached to prototype cargo airship.

A $14.1 \text{ m} \times 6.9 \text{ m} \times 2.9 \text{ m}$ reverberation chamber in the High Intensity Radiated Fields (HIRF) Laboratory of NASA LaRC was used for the testing of the WPT prototype cargo airship (see Figure 6 and Figure 7). This electromagnetically screened chamber is made of quarter inch thick

steel walls, floor, and ceiling that minimally absorb EM waves down to 120 dB in the 80 MHz to 18 GHz range. The low absorption of the metal causes the radiated fields to reflect off of the chamber surfaces numerous times, thus creating standing waves and making the EM wave distribution inhomogeneous. However, it is presumed that the rectenna arrays on the airship will face the intensity of impinging waves averaged by every direction throughout the chamber. In addition, two rectangular horn antennas with a 45 degree angle were installed to enhance the uniformity of these radiated fields.

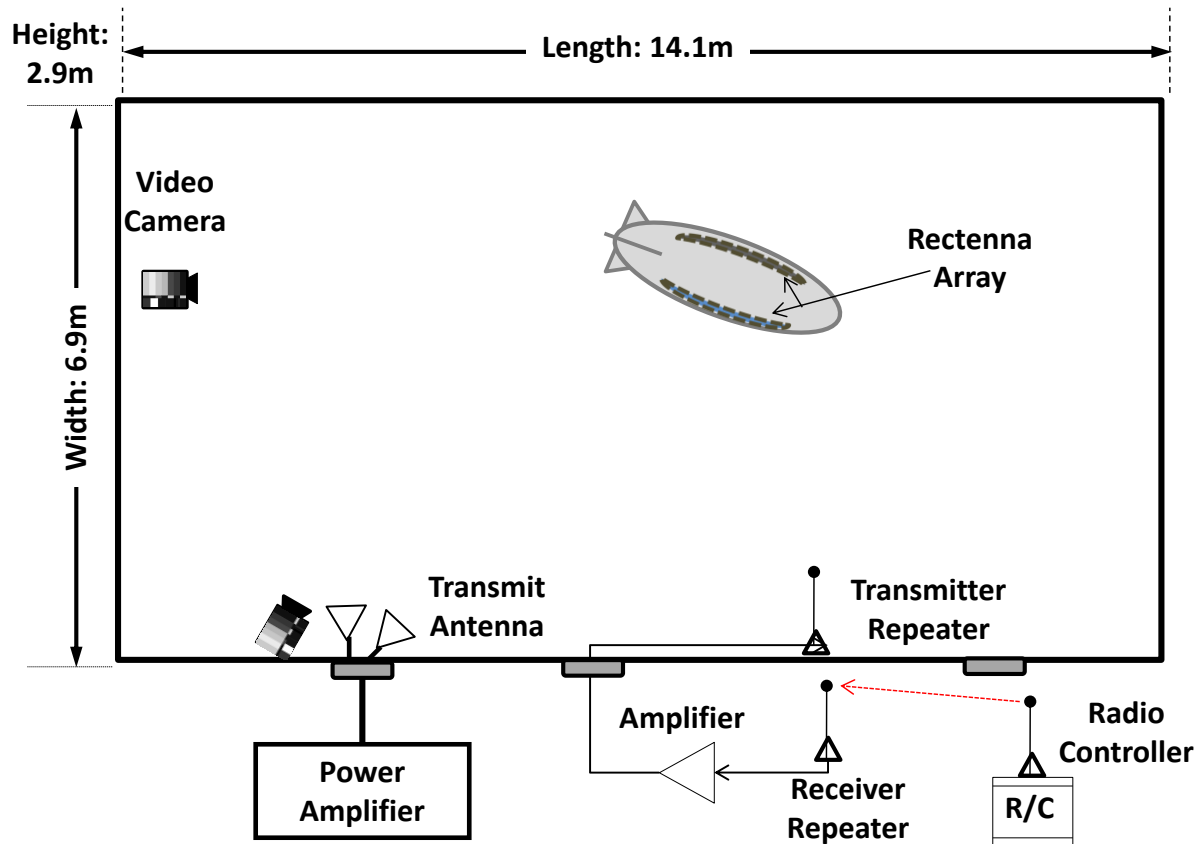


Figure 7. HIRF Lab reverberation chamber used to test the prototype WPT cargo airship.

The rectenna arrays attached to the prototype cargo airship were tested in the reverberation chamber prior to the test flights. Different frequency maxima along with a diminished power output (50 mW averaged power) of the rectenna arrays were found as compared to tests in the anechoic chamber (Figure 8). Two strong maxima were observed at 7.2 and 10.2 GHz with a power output of approximately 8 W, 9–10 V, and 800–900 mA. The multiple resonances could have been due to the rectangular shape of the horn antenna, and the decreased power output was most likely due to multiple reflections of the EM waves inside the reverberation chamber that caused changes in the polarization angles (i.e., the EM waves are unpolarized). Therefore, the aligned orientation of the linearly polarized dipole antennas of the rectennas within each array did not absorb the incoming EM waves as effectively as in the anechoic chamber tests where completely polarized EM waves were used.

The rectenna arrays attached to the prototype cargo airship were placed perpendicularly at a distance of 6 m from the rectangular horn antenna, and their output power was measured as the input power was varied from 20–200 W (Figure 9). The output power varied linearly versus input power for both 7.2 and 10.2 GHz with a 3–4 percent overall efficiency.

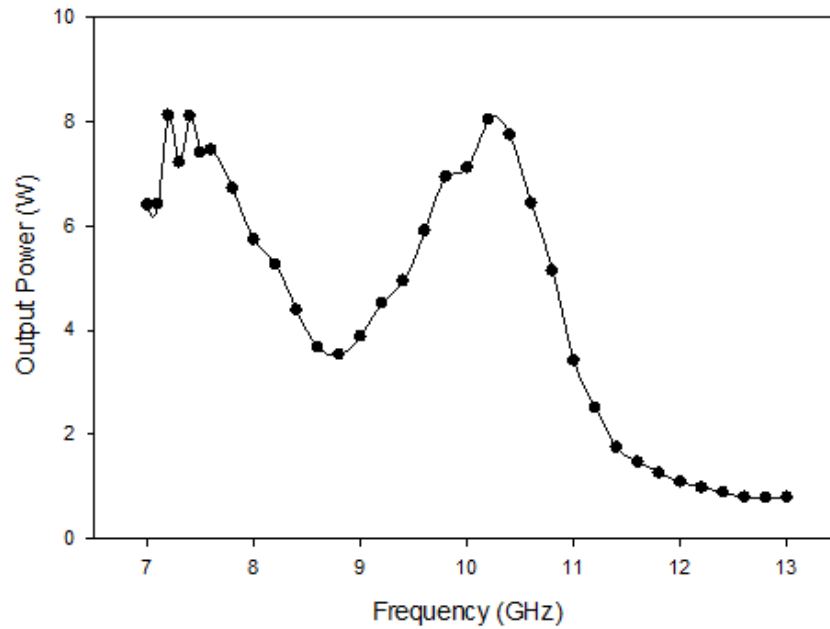


Figure 8. Power, voltage, and current output of the rectenna arrays measured as a function of frequency in the reverberation chamber.

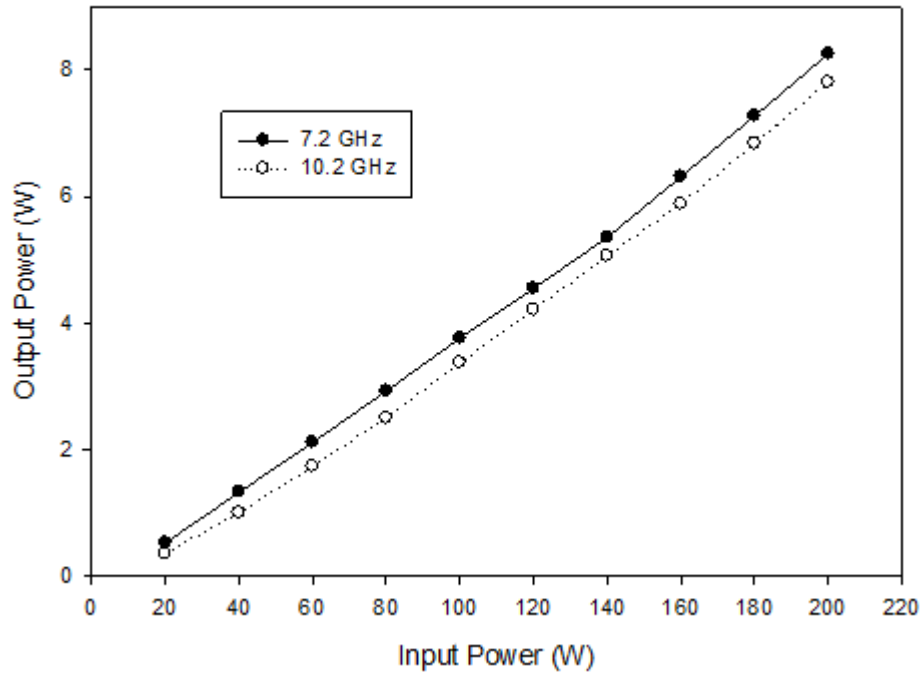


Figure 9. Output power of the rectenna arrays measured as a function of input power for the 7.2 and 10.2 GHz maxima. The arrays were measured at a distance of 6 m from the rectangular horn antenna.

The output power was also measured from the rectenna arrays on both sides of the airship (i.e., the port side facing away from the horn antenna and the starboard side facing towards it as shown in Figure 7). The output power of the port side was 88–95 percent of the starboard side when the airship was located 6 m from the horn antenna. This result demonstrates that microwave power propagating through the airship and reflecting off the reverberation chamber walls was converted into electrical energy. This interesting result warrants further investigation since it will influence the airship design, including materials selection and dimensions.

Another important factor that influences airship design is the output power of the rectenna arrays with respect to the incident angle of the transmitted microwave beam, which is determined by Lambert's cosine law. The output power was measured as the airship was rotated around its vertical axis from 0–120 degrees as shown in Figure 10, where the rectenna arrays are perpendicular to the microwave beam at zero degrees. The output power varied from 9.86 W at 0 degrees to 6.12 W at 90 degrees, about a 40 percent drop.

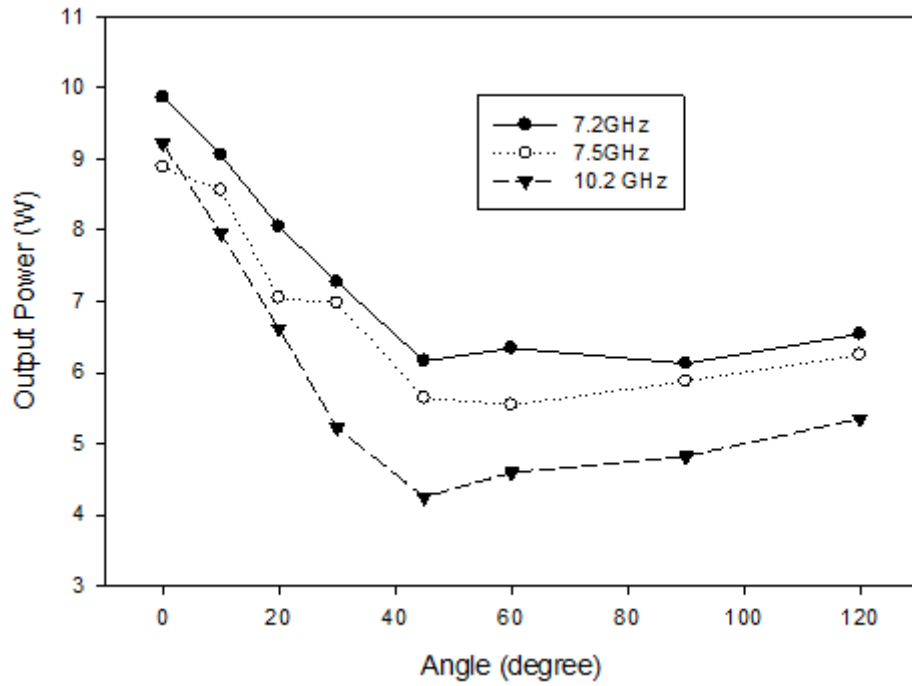


Figure 10. The output power of the rectenna array at various incidence angles.

The power characteristics of the rectenna arrays must also be evaluated for ideal operation of the airship motors (i.e., high current output at a low load resistance). Various resistor loads were used to determine the I-V characteristics of the rectenna arrays at various frequencies as shown in Figure 11, where a maximum power output of 1.7 W with a 19 Ω load resistance was found. Output power was maximized when impedance was matched at ideal load conditions, and, therefore, investigations of serial and parallel rectenna connections are needed.

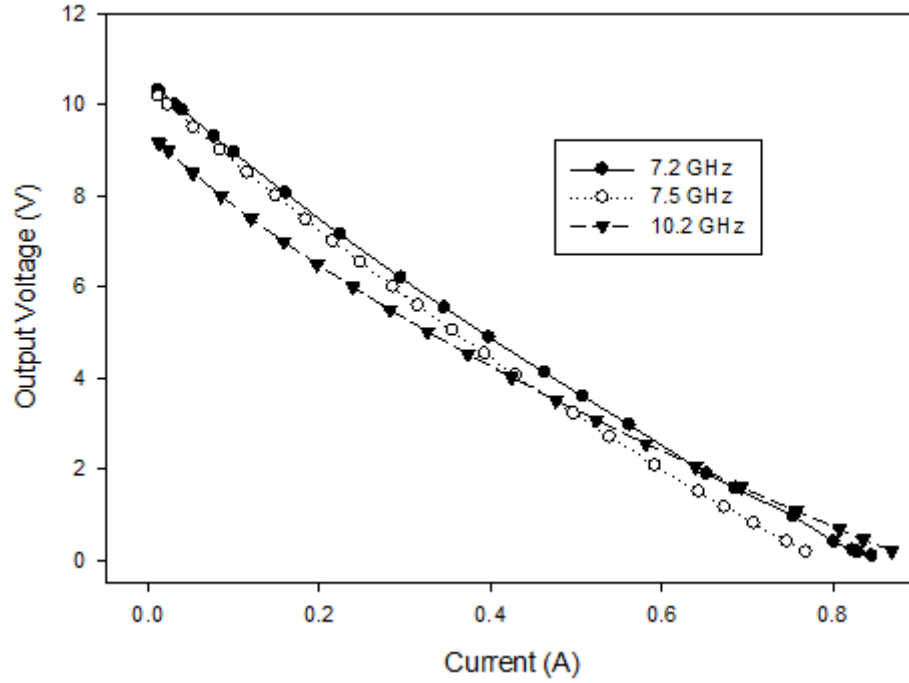


Figure 11. Power characteristics of the rectenna array with various load resistors at 6 m from the horn antenna.

The power requirements of the prototype cargo airship motors is approximately 4.8 V and 0.7 A to power three propellers (two for forward/backward motion and one for lateral movement). One rectenna array patch produces 4 V and 0.18 A at an average distance of 2 m from the 200 W horn antenna. Table 3 lists the various electrical connections of the rectenna array patches in serial and parallel combinations to maximize the needed output. Parallel connections are more desirable in order to increase the amount of current, since the maximum current flow capacity of the Schottky diodes is limited to 20 mA. Therefore, five serial connections of eight parallel patches were chosen to maximize the output power from the rectenna arrays.

Table 3. Output power of rectenna array patches for various serial and parallel combinations.

Parameters	Total Power	Power per Patch
4 serial connections of 4 parallel patches	0.496 W	31 mW
6 serial connections of 4 parallel patches	0.601 W	25 mW
6 serial connections of 6 parallel patches	1.284 W	36 mW
12 serial connections of 3 parallel patches	0.787 W	22 mW
4 serial connections of 8 parallel patches	1.320 W	41 mW
5 serial connections of 8 parallel patches	1.618 W	40 mW

Although the overall size and performance of a full-size 100 ton cargo airship was scaled down to approximately 2 percent of its size for tests in a reverberation chamber, the same design parameters discussed previously for a full-sized cargo airship were applied to the prototype cargo airship. The parameters of this scaled down version are shown as Case 1 in Table 4. A commercial ellipsoid airship with a diameter of 1.1 m and a length of 2.3 m was selected, as shown in Case 2, to match the scaled-down dimensions for the actual reverberation chamber tests. The electric power propulsion system was designed for a slow flight speed of 10 km/h in order to operate within the relatively small size of the chamber and was approximately 3 percent of the values for Case 1. Single rectenna patches at a frequency of 10.5 GHz delivered an averaged output power of 470 mW, which surpassed the required power of 190 mW for the Case 2 prototype airship.

Table 4. Prototype cargo airship parameters of a scaled-down 100 ton version (Case 1) and the actual scaled-down version for tests in the reverberation chamber (Case 2).

Parameters	Case 1	Case 2
Cruise Speed	70 km/h	10 km/h
Airship volume	1.31 m ³	
Diameter of airship	0.94 m	1.12 m
Length of airship	2.82 m	2.25 m
Required power	759 W	21 W
Effective area for rectenna	4.25 m ²	4.02 m ²
Required power density	179 W/m ²	5.2 W/m ²
Power on a rectenna patch	6.4 W	0.19 W

The output power of the rectenna arrays was investigated for the case of a partially deflated or “flat condition” of the airship because of the possibility of a leak. The output power was expected to change because of a change in the exposure area of the rectenna arrays to the microwave beam. This condition was tested by measuring the output power in a fully inflated airship and comparing it to a 30 percent flat condition as shown in Figure 12. This flat condition was measured by an equilibrium weight of helium buoyancy force. The measured output power of the rectenna arrays in the flat condition was less than 15 percent of the normal condition in the frequency range of 9–10 GHz. In the other frequency ranges, the output power slightly increased as compared to the normal fully inflated condition. These results indicate little concern about losing output power in a flat condition of the airship. In general, these test results show that WPT is a promising technology to deliver power to a cargo airship under various foreseen conditions.

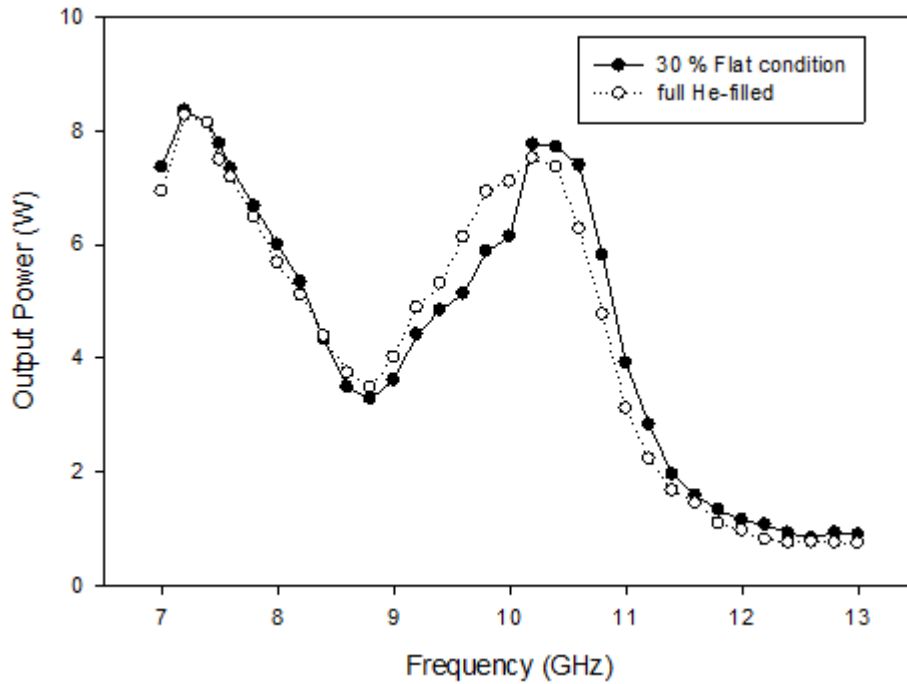
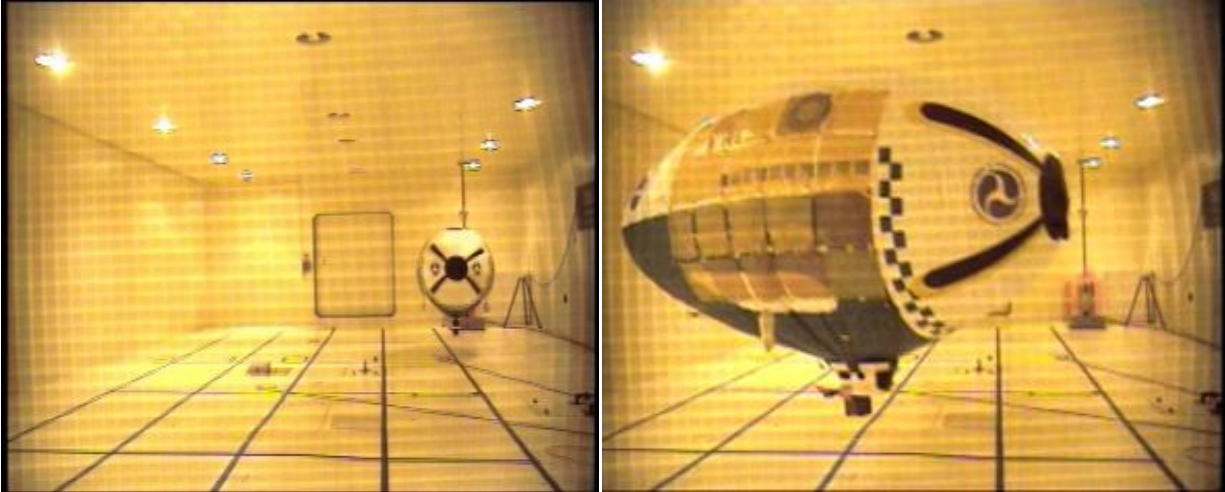


Figure 12. Power output of rectenna array in a 30 percent deflated “flat” condition.

Flight testing of the prototype cargo airship inside of the reverberation chamber in the HIRF lab was performed using 400 W of continuous wave power at 10.5 GHz as shown in Figure 13. A radio frequency controller (R/C) was added to the gondola for airship control and a four-channel frequency modulation (FM) receiver was added to receive 78 MHz control signals from the remote driver. Pulse position modulated signals from the R/C transceiver were delivered to a servo motor, while two SPY motor control units were used to control two thrust motors for propulsion and a tail fan for turning. No batteries were used and electric power was only supplied from the rectenna array. Flight tests under WPT rectenna arrays were monitored and recorded by two digital cameras installed in the reverberation chamber. A HIRF lab movie clip demonstrated the speed and control of the cruising airship in the chamber. Even though the power conversion efficiency in the reverberation chamber was far less than the one measured in the anechoic chamber, the prototype airship presented full control with a maximum speed around 10 km/h aided by the wind-free conditions inside the chamber.



(a) Nose view.

(b) Side view.

Figure 13. Photos of the flight test inside the reverberation chamber with WPT.

The power flux density received by a rectenna array is an important factor for the design of a WPT cargo airship. Therefore, it is essential to design higher frequency rectennas in the V-band, W-band, and optical-band regions. Therefore, V-band rectennas with enhanced efficiencies have been fabricated and optimized for cargo airship transportation applications beyond the X-band.

SECTION 3

ADVANCES IN WIRELESS POWER TRANSMISSION

In conventional rectenna design, parallel rectenna distribution employs direct connections on a single plane, where the electrical power distribution lines directly connect the antenna to the adjacent rectenna. This approach can reduce the complexity of power line distribution, as long as the input impedance is well matched to the resonance frequency of the dipole antenna. This design scheme of connecting the AC and DC circuits along the transmission line can also be effective based on the assumption that output filters with shunt capacitors can sufficiently block EM wave transmission. This approach can be applied by employing discrete capacitors with large capacitance values at low frequencies.

However, when the operation frequency increases beyond the X-band, the physical layout of the rectenna does not allow the placement of discrete chip capacitors because of the small layout space. The size of a capacitor becomes comparable to the wavelength of the operation frequency that can generate higher order harmonics and furious wave modes. Within the layout area limit, discrete chip bonding is often difficult and the cost of chip bonding significantly increases. If a planar capacitor is employed following the conventional rectenna design, the low capacitance from a planar structure does not effectively block the EM wave propagation. Instead, EM waves may leak through the blocking capacitor and couple with the other rectenna circuit elements located next to the dipole antenna. Specifically, the coupling of dipole antennas with Schottky diodes is a critical factor in rectenna performance. The nature of EM wave dispersion due to this coupling can be a significant barrier, dropping power conversion efficiency in rectenna operation. Even a small shift of antenna resonance frequency can significantly drop the efficiency of the rectenna.

Thus, to improve the rectenna performance, a new rectenna design for the V-band was performed using IE3D software. Figure 14 shows an S11 parameter of a dipole rectenna with an impedance of $68\ \Omega$ on a flexible duroid board. At 45 GHz, a 15–20 dB level of S11 is calculated with the widths of the dipole rectenna from 25–200 μm . A coupled stripline was placed on the board for the design of passive elements including low pass filters and a short capacitor. The characteristic impedance of the design was matched with the input impedance ($120\ \Omega$) and bonding pad layout of the Schottky diode.

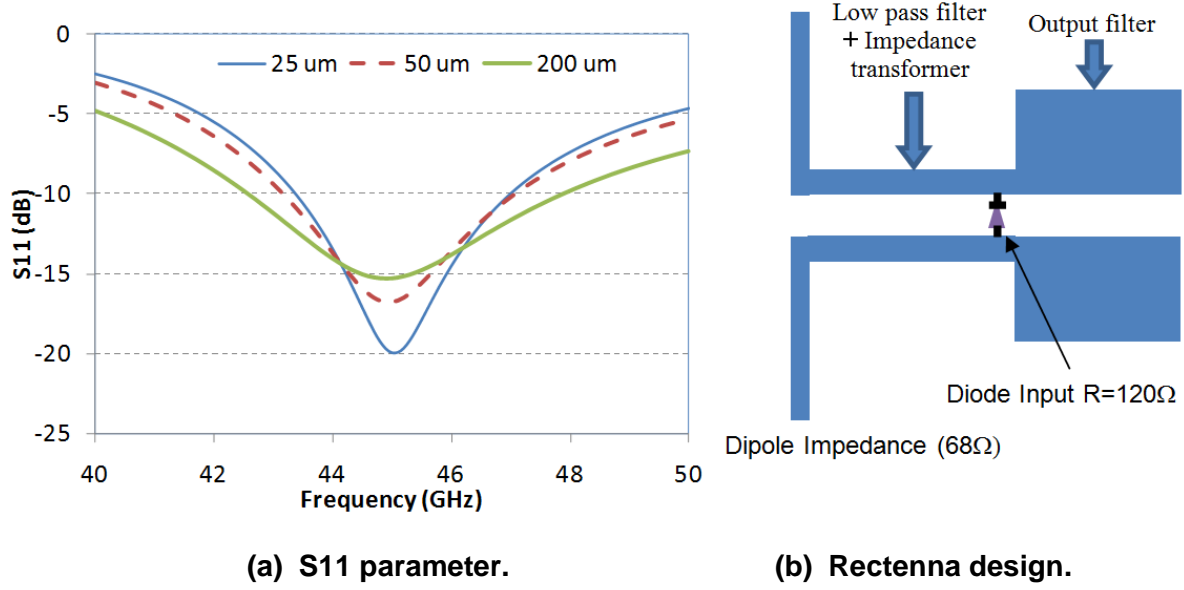


Figure 14. S11 parameter of dipole rectenna versus frequency for various widths of the antenna and a schematic diagram of a rectenna design.

Figure 15 shows schematic and circuit designs of a Schottky diode based on the silicon integrated circuit (IC) fabrication process. Based on the design, the power conversion efficiency was calculated with respect to the Schottky diode series resistance (R_S) at 45 GHz as shown in Figure 16. Based on the circuit analysis and simulation result, a dual layer of a V-band rectenna design was adopted as shown in Figure 17. This design provides a significant size reduction and suppressing parasitic impedance. A closed form of the power conversion efficiency can be derived from the rectifying circuit model (Figure 14 and Figure 17) and the fundamental frequency input (45 GHz). This simple form of analysis assumes that there is no power loss by higher order harmonics, the diode forward voltage drop is constant during the forward biasing period, and there are no insertion and return losses from the antenna and filter design. Details of the theoretical analysis can be found in references 28 and 29. Thus, the power conversion of the 45 GHz rectenna is calculated as 40 percent by following this analysis and using the parameters of the silicon Schottky diode (SMS7621-060) that are shown in Table 5. This power conversion can be increased to a 60 percent level if the series resistance and the junction capacitance values are lowered as shown in Figure 16.

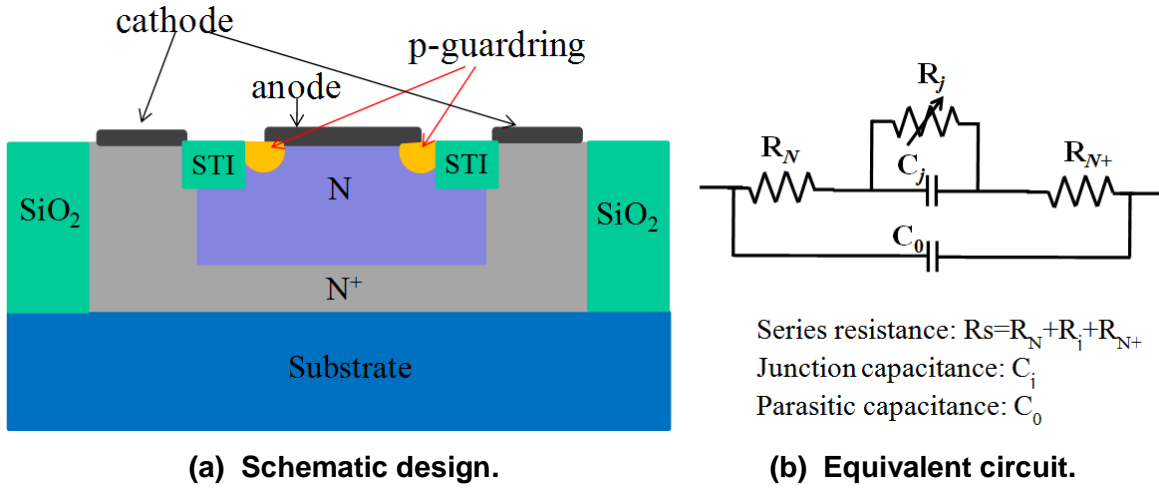


Figure 15. 45 GHz Schottky diode.

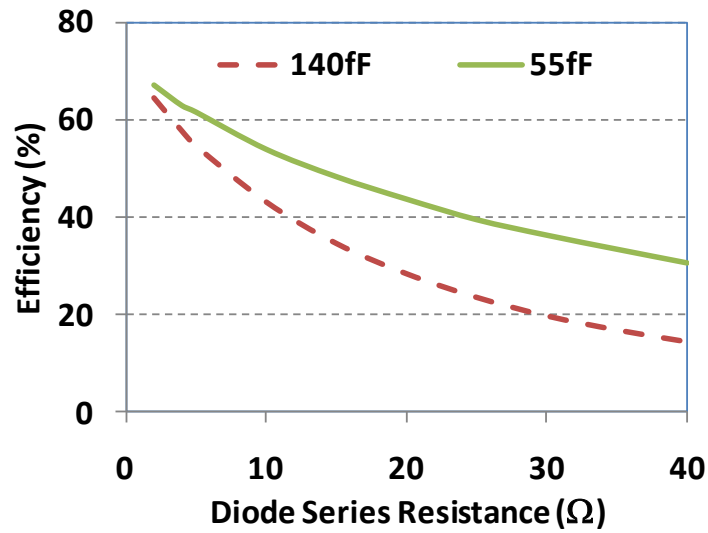


Figure 16. Power conversion efficiency of a rectenna with various Schottky diode resistances.

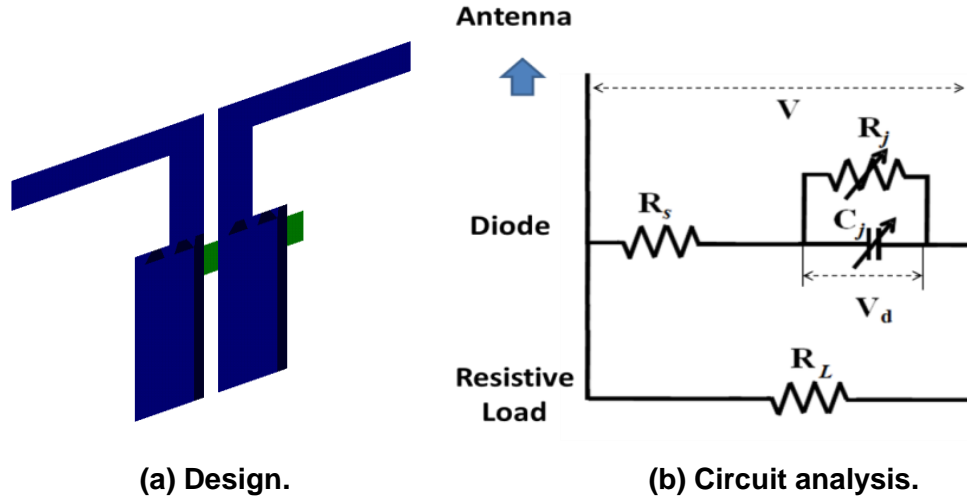


Figure 17. V-band rectenna.

Table 5. Rectenna circuit parameters and output voltage and power using a silicon Schottky diode (SMS621–060).

Parameters	Values
Breakdown voltage, V_B	3 V
Diode Junction Voltage, V_{bi}	0.51 V
Series Resistance, R_s	12.5 Ω
Zero Bias Junction Capacitance, C_0	130 fF
Cutoff Frequency, F_C	189 GHz
Load Resistance, R_L	109 Ω
Output Voltage, V_0	1.4 V
Output Power, P	18 mW

This V-band rectenna design has been further optimized based on IE3D software simulations as shown in Figure 18 and then fabricated as shown in Figure 19. This progress on V-band rectenna arrays now opens the door to higher frequency bands, such as the W-band, with the possibility of continuing towards the optical band.

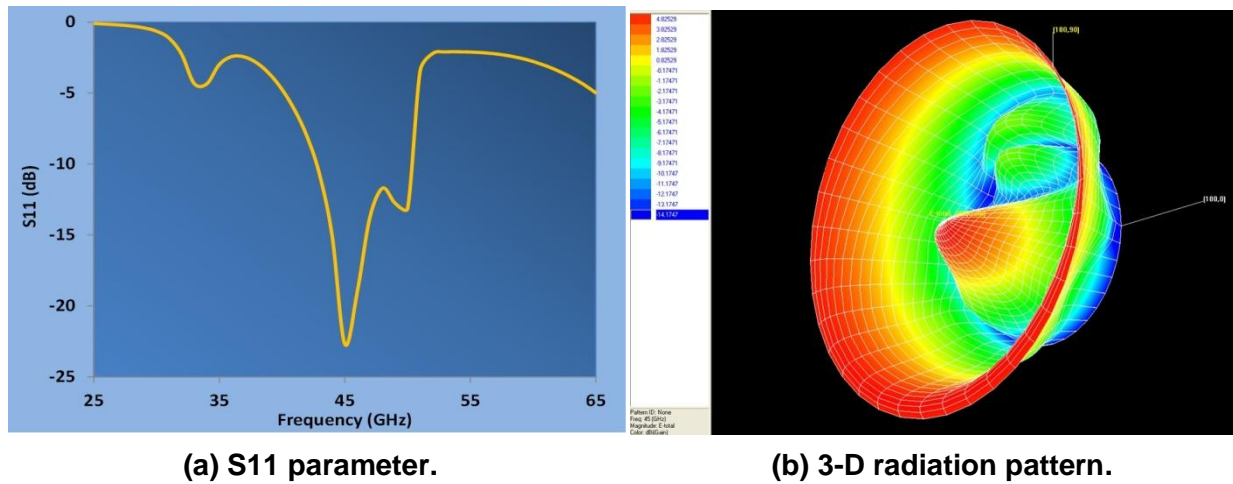


Figure 18. Simulations of a Schottky diode assembly on a V-band rectenna array.

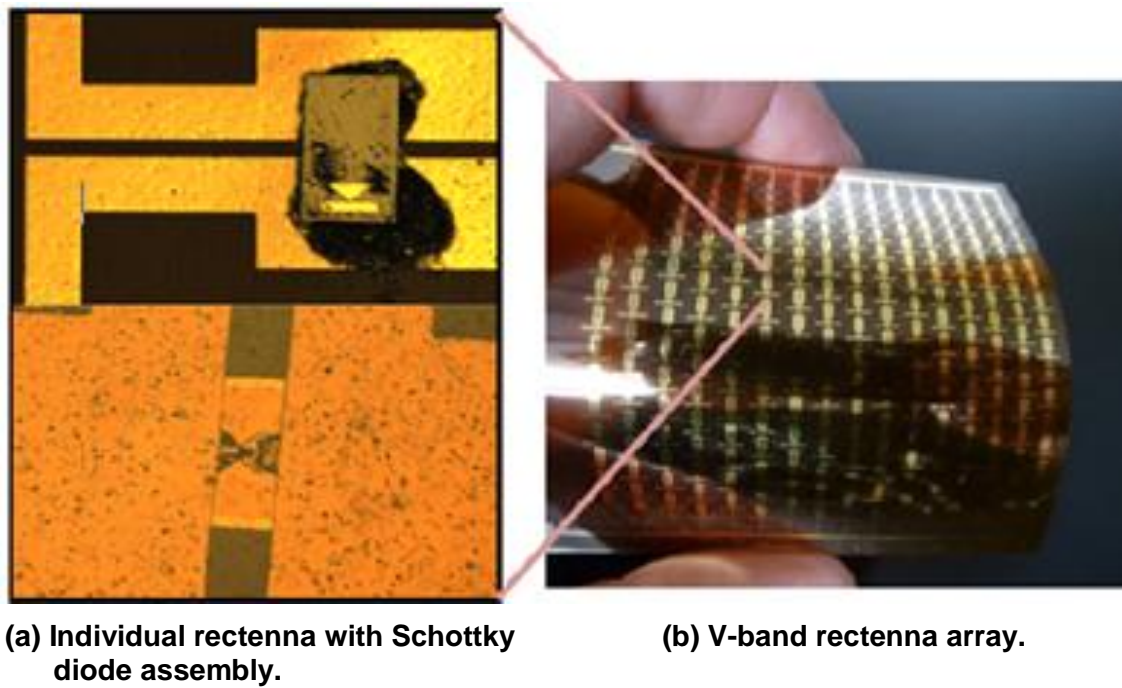


Figure 19. Fabricated Schottky diode assemblies on a V-band rectenna array.

SECTION 4

FEASIBILITY STUDY OF CARGO AIRSHIP TRANSPORTATION USING SOLAR POWER

A solar powered airship prototype was designed, built, and flight-tested at NASA LaRC in order to study size-scaling effects, in-air cargo manipulation, photovoltaic power conversion, and the storage/delivery of electrical power from solar cells and batteries. Solar power may be combined with the wireless power technology discussed in the previous sections to provide uninterrupted power to a cargo airship. This airship prototype was designed with a 20 foot length, a payload capacity of 3 kg (neutral buoyancy with no energy consumption) or 13 kg (maximum energy consumption), a solar recharge capacity of 1 kW, a maximum power delivery of 10 kW (13.4 hp) from batteries, and a multi-rotor propulsion system controlled by a simple avionics computer equipped with wireless video transmission. This study shows that this solar powered airship prototype provides very efficient cargo delivery solutions to overcome many transportation obstacles.

The prototype airship was designed to have a single helium envelope consisting of two cylindrical-like components separated by a middle section. This configuration offers more lift than the conventional (i.e., cigar-shaped) airship design, while still featuring a slender, aerodynamic shape. It also offers more surface area for solar cells on the top surface of the helium envelope, as well as for the gondola and cargo containers on the lower surface. The dimensions of the airship were determined by calculating the lift necessary for a neutrally buoyant and 100 percent cargo container payload configuration. These dimensions, as shown in Figure 20, were determined by taking into consideration such factors as: the helium envelope material and corresponding attachments, the solar cell array for power generation, and the gondola for propulsion control and cargo manipulation.

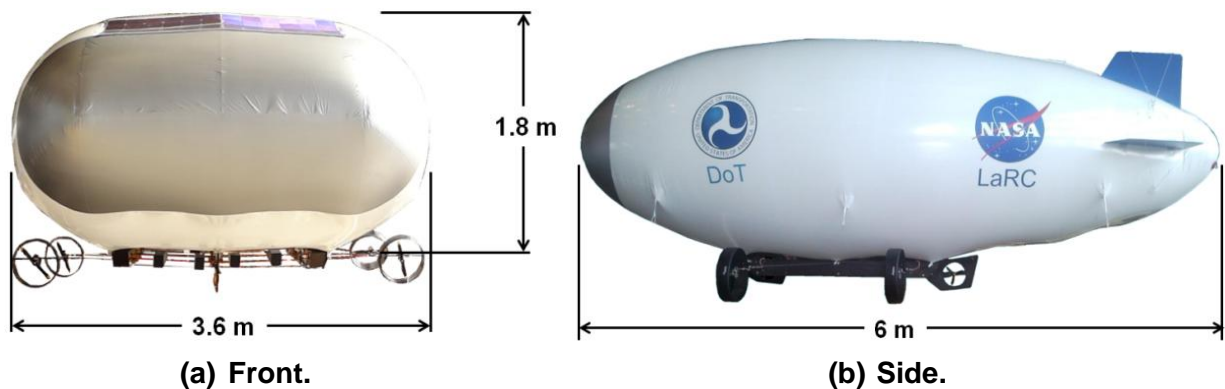


Figure 20. View of the airship with its dimensions.

The volume of the helium envelope for the lift calculation was approximated using two oblate spheroids plus a midsection as shown in Figure 21. The resulting calculation yields a helium volume of $\sim 25 \text{ m}^3$ that can provide $\sim 25.6 \text{ kg}$ of lift. Table 6 lists the known masses of the envelope material (3.5 mil polyurethane) and other components.

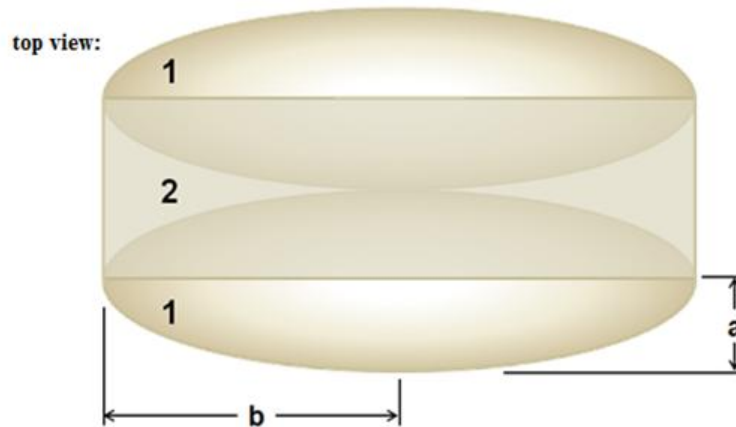


Figure 21. View of the top of the airship with the approximation for the lift calculation.

Table 6. Lifting forces and masses of the various airship components.

Specification	Approximation
Total volume	25 cu meters (882 cu ft)
Lifting force	25.6 kg (56.5 lbs)
Total surface area	50 sq meters (13.5 ft)
Envelope material weight	6 kg (13 lbs)
Weight of fins, patches, etc.	2.8 kg (6 lbs)
Weight of solar cells, wire, etc.	8.3 kg (18 lbs)
Weight of gondola w/ cargo	9.9 kg (21.8 lbs)
Total weight without helium	27 kg (59.5 lbs)
Total lifting force	-1.4 kg (-3 lbs)

The fins and bridle patches were secured to the helium envelope using vinyl cement. The bridle patches served as attachment points for the gondola (8–35 lb patches) and for tethering the airship during fabrication and testing (6–55 lb patches) as shown in Figure 22.

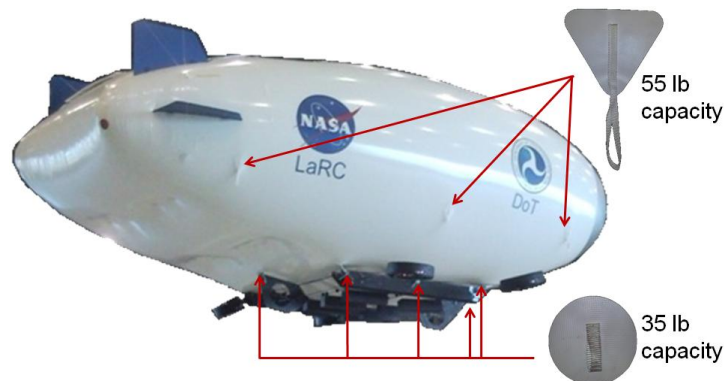


Figure 22. Bridle strap locations on the helium envelope for securing the airship during fabrication and testing (55 lb) and attaching the gondola (35 lb).

A negative buoyancy of 1.4 kg was determined to be acceptable because the actual lifting force varies with atmospheric changes (i.e., temperature and pressure). These variables can be accounted for on a full-sized cargo airship by a ballonnet that functions to maintain the shape and lift of the airship as its volume changes because of temperature and pressure gradients.

Commercially available off the shelf silicon solar cells were used, along with other materials, to fabricate the solar cell panels for the cargo airship. Thirty-two solar panels were constructed to power the airship with each panel measuring approximately $0.33 \text{ m} \times 0.95 \text{ m}$ with a mass of 215 g. Each panel consisted of twelve grade B monocrystalline silicon solar cells ($200 \text{ }\mu\text{m}$ thick) secured to a 9.5 mm thick rigid polystyrene backing material with a spray adhesive. This rigid and lightweight backing material was commercially available off the shelf and had a density of 21.5 g/m^3 . Two of these 12-cell panels were connected in series, such that 24 solar cells provided 12–13 volts in an open circuit configuration (V_{OC}) and up to 8.8 amps in a short-circuit configuration (I_{SC}). The current-voltage (I-V) curves for each of these 24-cell panels were tested in ambient sunlight conditions with the irradiance measuring near 1000 watts/m^2 (Figure 23). The maximum power generated by these 24-cell panels was approximately 35–40 watts at 7–8 volts and 5 amps. Four of these 24-cell panels are connected in parallel allowing the current from each 24-cell panel to be summed, such that approximately 20 amps can be delivered to the motors. This results in approximately 600 watts of electrical power that can be generated from the sun under ambient conditions.

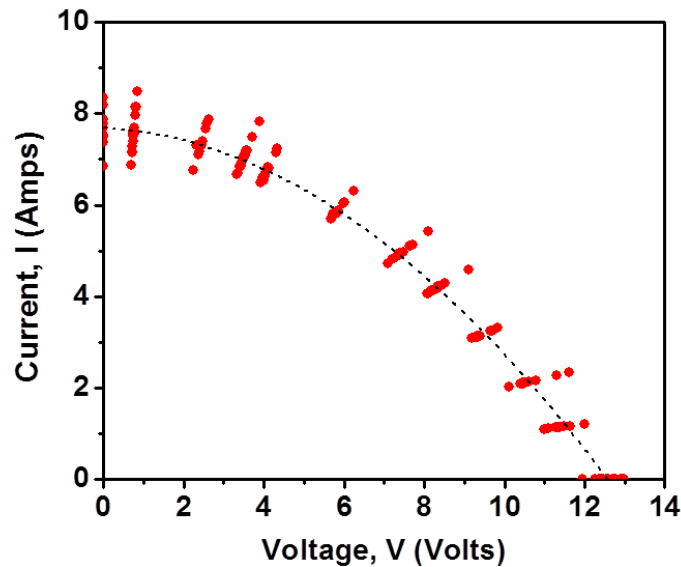


Figure 23. Current-voltage (I-V) data (red) and best fit (black) for the 24-cell solar panels tested in ambient sunlight conditions.

These grade B monocrystalline silicon solar cells have an advertised efficiency of 17 percent with 4 watts of peak power. However, the measurements of these cells under ambient conditions show that there are substantial losses due to series (R_s) and shunt (R_{sh}) resistances, as can be evidenced from the I-V data shown in Figure 23. Measurements under ambient sunlight conditions show that the efficiency is closer to 7 percent with a peak power near 1.7 watts. Dark I-V curves, shown in Figure 24, can be used to approximate the values of R_s and R_{sh} , which are $0.2 \text{ }\Omega$ and $30 \text{ }\Omega$, respectively.

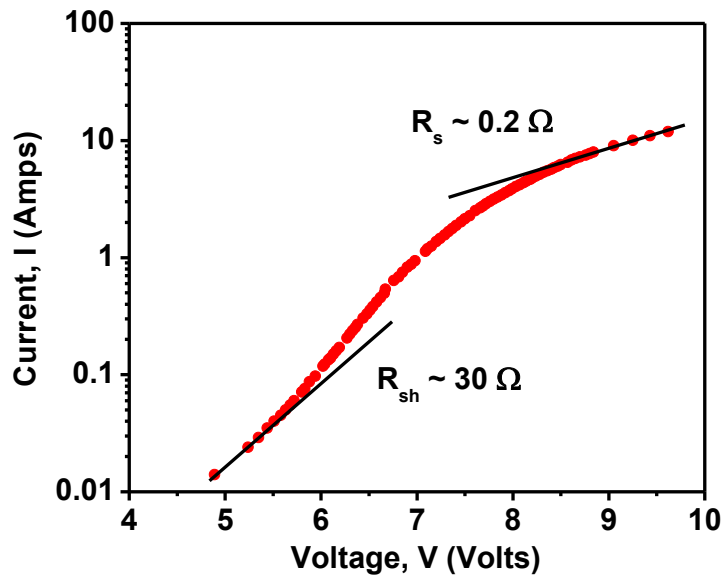


Figure 24. Dark I-V curve used to approximate the values of R_s and R_{sh} .

The solar cell panels were attached to the airship using vinyl cement and hook and loop strips. Each 12-cell solar panel had a mass of 215 g, which included the rigid polystyrene backing material, spray adhesive, monocrystalline silicon solar cells, tabbing wire, and solder. These 32 panels (6.9 kg) were connected in parallel with 0.1 kg of busbar wire and were attached to the polyurethane envelope of the airship with 0.7 kg of hook and loop strips. This yielded approximately 7.7 kg of mass on top of the airship. An additional 0.625 kg of wire to distribute the power generated by the solar panel assembly ran down the side of the airship to the motors.

The design of the propulsion modules and gondola required assessments of the cargo airship's structural design, weight distribution, remote control and avionics integration, and programming development for the flight dynamics and controls.

The gondola and propulsion modules were designed with a three-dimensional (3-D) computer-aided design (CAD) program where a 3-D rendered view of the semi-production model is shown in Figure 25. The four main propulsion propellers are shrouded and attached to a rotatable arm that is controlled by a high torque servo and gear set as shown in Figure 26. The main propeller can rotate forward at 100 percent of the maximum revolutions per minute (rpm) and backward at 50 percent of the maximum rpm with programmable electronic speed controllers (ESCs). The high torque servo allows at least 180 degrees of rotation (i.e., ± 90 degrees rotation from the forward 0 degree direction). Each of the four main propellers has independent angle and propulsion control, such that eight degrees of freedom (DoF) are possible: four rotation angles and four rpm controls. Two side propellers are also fixed on the front and rear pins, which allow a roll motion, a hover left/right motion, and a clockwise/counterclockwise motion when coupled with the four main propellers, thus allowing a total of ten DoF. Eight cargo trailers are suspended from cargo lift pulleys that allow the cargo containers to be raised and lowered in the vertical direction.

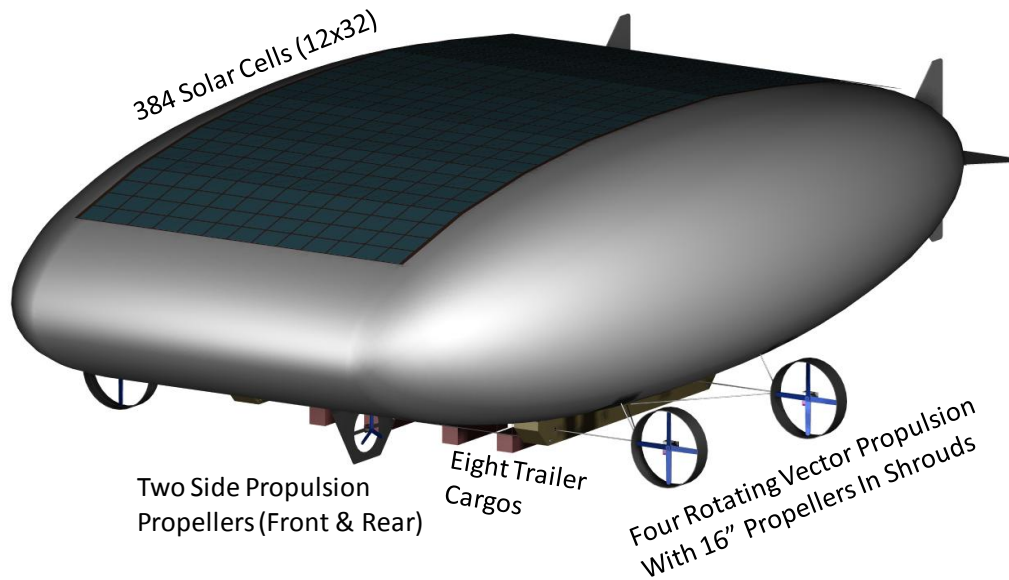


Figure 25. 3-D rendered top view of the semi-production model of the solar powered cargo airship prototype.

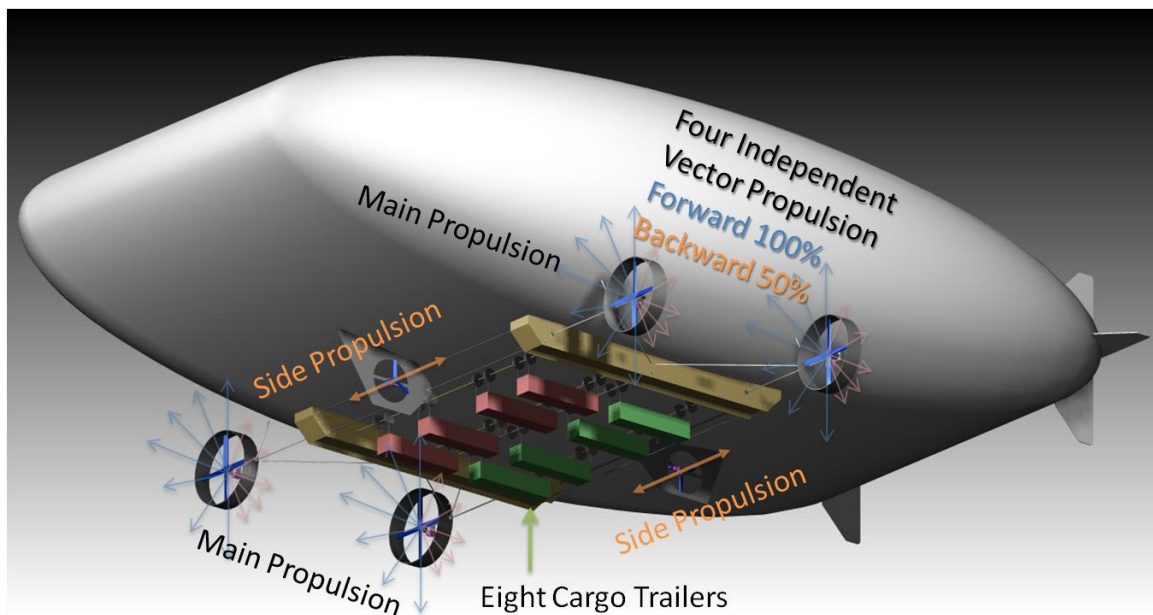


Figure 26. Propulsion gondola module with four variable angle main propellers and two fixed side propellers.

Figure 27 shows a two-dimensional (2-D) CAD view of the front of the cargo airship prototype with the vertical weight distribution. The mass of the solar panels is slightly less than 7 kg, the airship membrane is approximately 5.5 kg, and the gondola is 8–10 kg, depending on the cargo mass. The large solar cell mass on the top surface of the cargo airship raises the center of mass towards the center of the airship body. However, the center of the mass will be lowered as the airship size becomes larger because the lifting force is proportional to the volume (i.e., radius cubed r^3), whereas the mass of the solar cells is proportional to the area (i.e., radius squared r^2).

Therefore, as the size of the airship becomes larger, the mass percentage of the solar cells becomes smaller while the mass percentage of the propulsion gondola and cargo containers becomes larger. Thus, the center of the mass will become lower, offering greater stabilization as the size of the airship is increased.

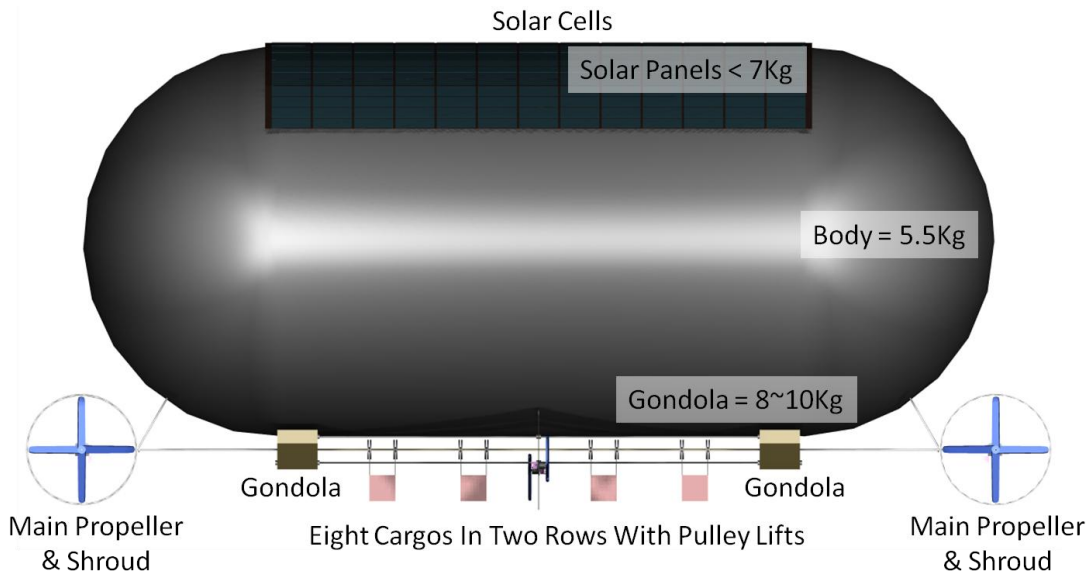


Figure 27. 2-D CAD view of the front side of airship with the vertical weight distribution.

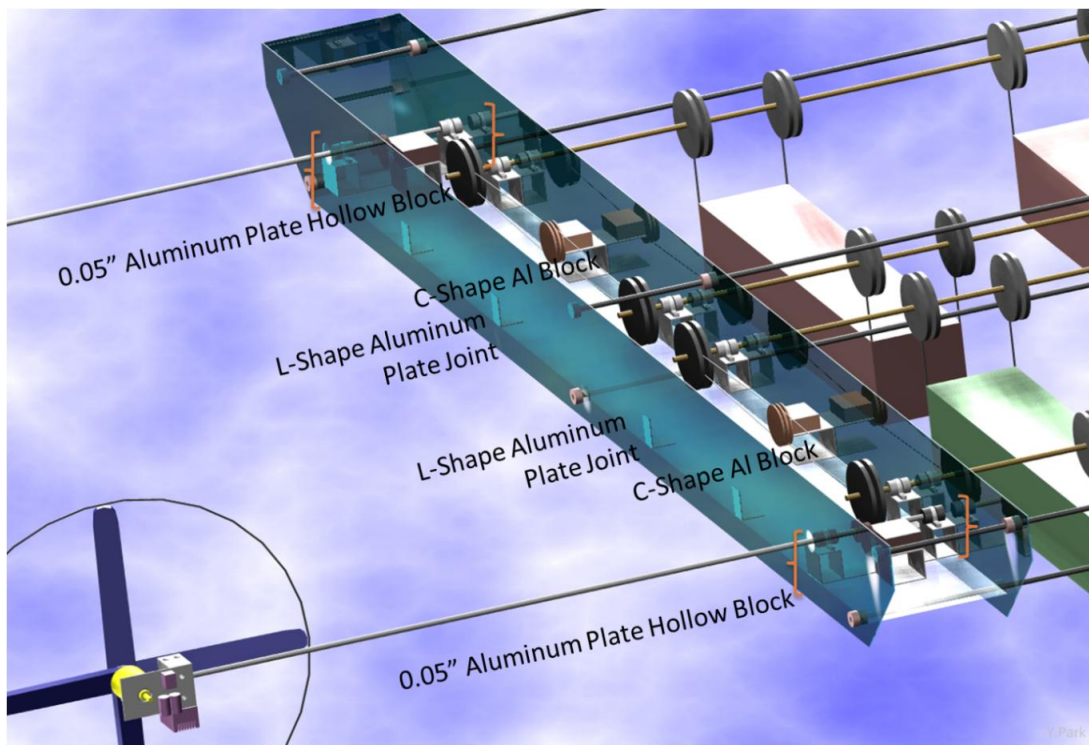


Figure 28. Joint and supporting aluminum blocks for servos and gears.

The propulsion modules and gondola were originally designed with approximately 260 components and estimated to be between 8 kg (no cargo) and 10 kg (full cargo). However, they were fabricated with about 300 components, including extra propeller shrouds and supporting rods during final modifications. The actual final mass of the propulsion gondola was 9.9 kg without any cargo. All of the joints and supporters for the servos, pulleys, and gears were made with L-, C-, and D-shaped aluminum plates for high strength with minimal mass as shown in Figure 28. Figure 29 shows the location and mounting schemes for the motors, servos, and ESCs. Brushless outrunner motors with rare-earth neodymium iron borate (NdFeB) magnets that can operate at up to 180°C were used as the main propulsion motors. These motors are rated at 840 W, 60 A maximum current, and 1110 rpm per volt at no load and were able to deliver 1.1 kg of thrust at 220 W and 1500 rpm with the selected propeller.

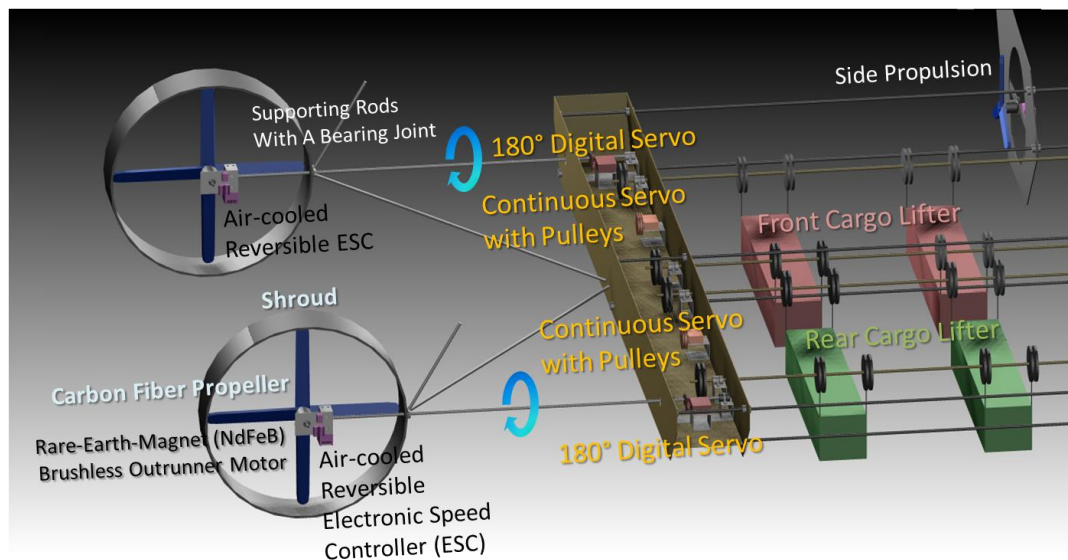


Figure 29. Location of each motor, ESC, servo, and gear box.

The control software for the cargo airship prototype was developed for 10 DoF vector propulsion using a programmable 14-channel 2.4 GHz transmitter (Futaba 14MZ with TM-14 radio) that has a microcomputer running on the Windows CE operating system with dual internal processors. The servo motion, control and mixing, propulsion control, cargo lift operations, and camera movements were controlled via a custom-designed program on the transmitter. All 14 channels (12 analog and 2 digital) were controlled individually by the custom-designed program as diagramed in Figure 30. This custom-designed software enables a transformable propulsion system that can start with a vertical takeoff and landing (VTOL) mode, then transform into a hovercraft mode, and finally transform into a quad-copter mode for maximum cargo manipulation during hovering.

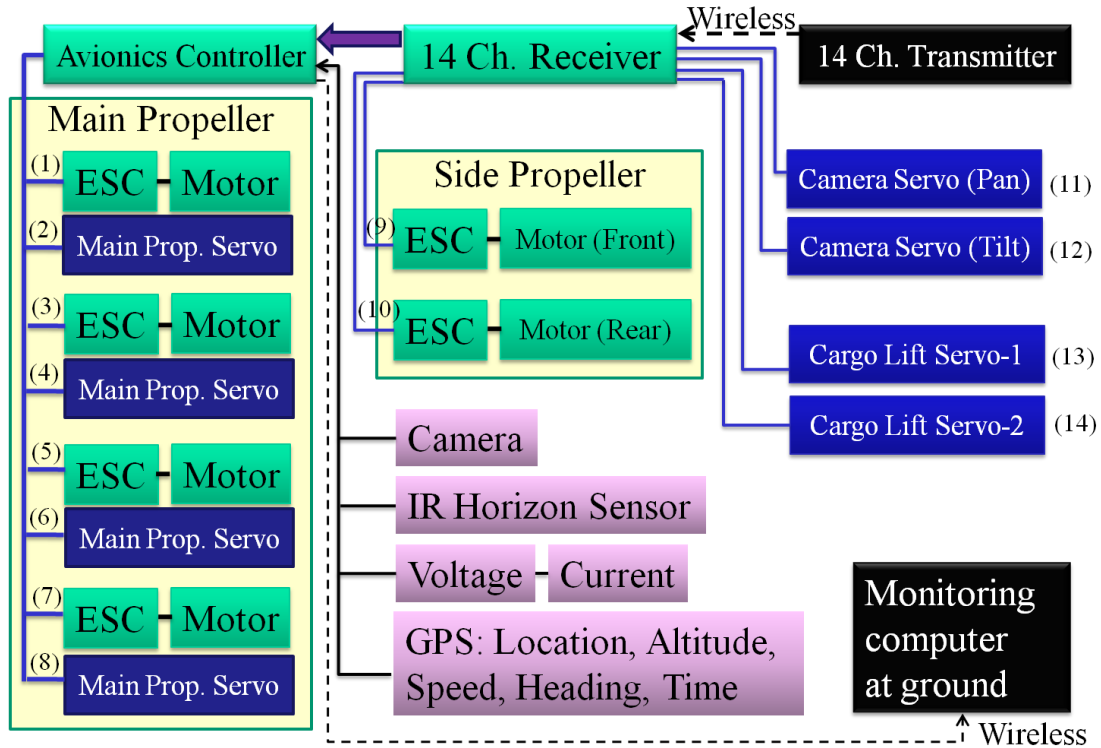


Figure 30. Propulsion and flight control system diagram with 14 channels.

The cargo airship prototype has basic avionics with a global positioning system (GPS), 900 MHz wireless camera with pan and tilt, and various sensors. This avionics system supports the wireless display of GPS position with longitude and latitude, heading with a compass display, speed, altitude, time, voltage, current, motor temperature, satellite reception, and line-of-sight distance from the takeoff point. An additional inertia motion unit (IMU) with a 3-D accelerometer was installed for the artificial horizon display, which allows for precise determination of the attitude of the airship for better pitch, yaw, and roll data.

The first internal flight test was conducted on October 4, 2011, and the final demonstration flight was made on October 26, 2011, with NASA LaRC and DoT members in attendance. The flight tests were made inside a large hangar at NASA LaRC using four lithium-ion batteries to power the cargo airship prototype, since solar energy was not available. However, these batteries were completely removed to demonstrate the full operation of the airship with solar power while it was attached to its structure as seen in Figure 31. Outdoor flight tests of the airship did not occur because the wind conditions (speed and direction) at this time of year were not within the limits imposed because NASA LaRC is located next to Langley Air Force Base. Nevertheless, all of the important factors were measured under direct ambient sunlight in a tethered airship control mode: (i) total propulsion thrust and power, (ii) electrical power generation, delivery, and consumption, (iii) 10 DoF vector propulsion control, and (iv) avionics operations. Figure 32 shows the indoor flight test inside the hangar at NASA LaRC where the basic flight dynamics (i.e., yaw, pitch, and roll) and flight modes (i.e., VTOL, hovercraft, and quad-copter) were examined along with cargo manipulation. The indoor flight tests and outdoor propulsion tests of the solar powered cargo airship prototype were recorded and are available. These tests of a solar

airship proved the unprecedented excellent propulsion control for maximum cargo manipulation and very high propulsion thrust from direct sunlight without batteries.



Figure 31. The fully assembled solar powered cargo airship prototype attached to its support structure.



Figure 32. Scene from video of the indoor flight test of the solar airship.

Additional measurements and testing can be performed on the airship by installing an onboard data acquisition microcomputer with a long-range wireless modem such as an RF modem that has a range of 14–40 miles or a satellite modem with almost unlimited global coverage. An onboard microcomputer was installed on the solar cargo airship for data collection and video processing. However, the automatic flight control of motors and servos based on the data from sensors (e.g., GPS, altitude, and attitude) was not used because of regulations and certification requirements.

Two of the most critical advancements that are needed for cargo airships at this time are further stability control and power generation capabilities. Better stability control from electronic control systems will be needed as the physical size and cargo carrying capacity of these cargo airships get larger and larger. Their huge surface area makes them susceptible to high winds and other unfavorable weather conditions and will need to be addressed. Also, more efficient power

generation sources will be needed to keep these control systems operational without the need for energy storage. One possible technology that is explored in the next section and related to the solar powered cargo airship is NASA-developed crystalline rhombohedral SiGe on trigonal sapphire substrates. This technology offers the possibility of increased efficiency as discussed in the next section.

SECTION 5

RHOMBOHEDRAL EPITAXY OF CUBIC SiGe ON TRIGONAL C-PLANE SAPPHIRE

New green energy sources with high efficiencies are needed to meet growing energy demands. One of these potential green energy sources is a quantum well (QW) solar cell that relies on the material development of rhombohedral SiGe. Conventional silicon solar cells have approximately a 30 percent theoretical limit of efficiency assuming perfect p-n junctions (ref. 31), although the highest recorded efficiency measures only at 25 percent (ref. 32). Polycrystalline silicon tends to be less efficient than monocrystalline silicon, showing that the crystallographic quality affects performance (ref. 33). Silicon has a cubic crystal structure, which is one of the two crystal structures into which most semiconductors in today's industry are categorized. The cubic crystal structure encompasses Group IV materials (Si, Ge, C, etc.) in the diamond structure, and Group III-V semiconductors (GaAs, GaP, InP, AlAs, etc.) and Group II-VI semiconductors (CdSe, HgTe, etc.) in the zinc-blende structure as shown in the cubic bandgap engineering diagram in Figure 33. This group of cubic materials has encompassed a multi-trillion dollar market since the invention of the transistor in 1947.

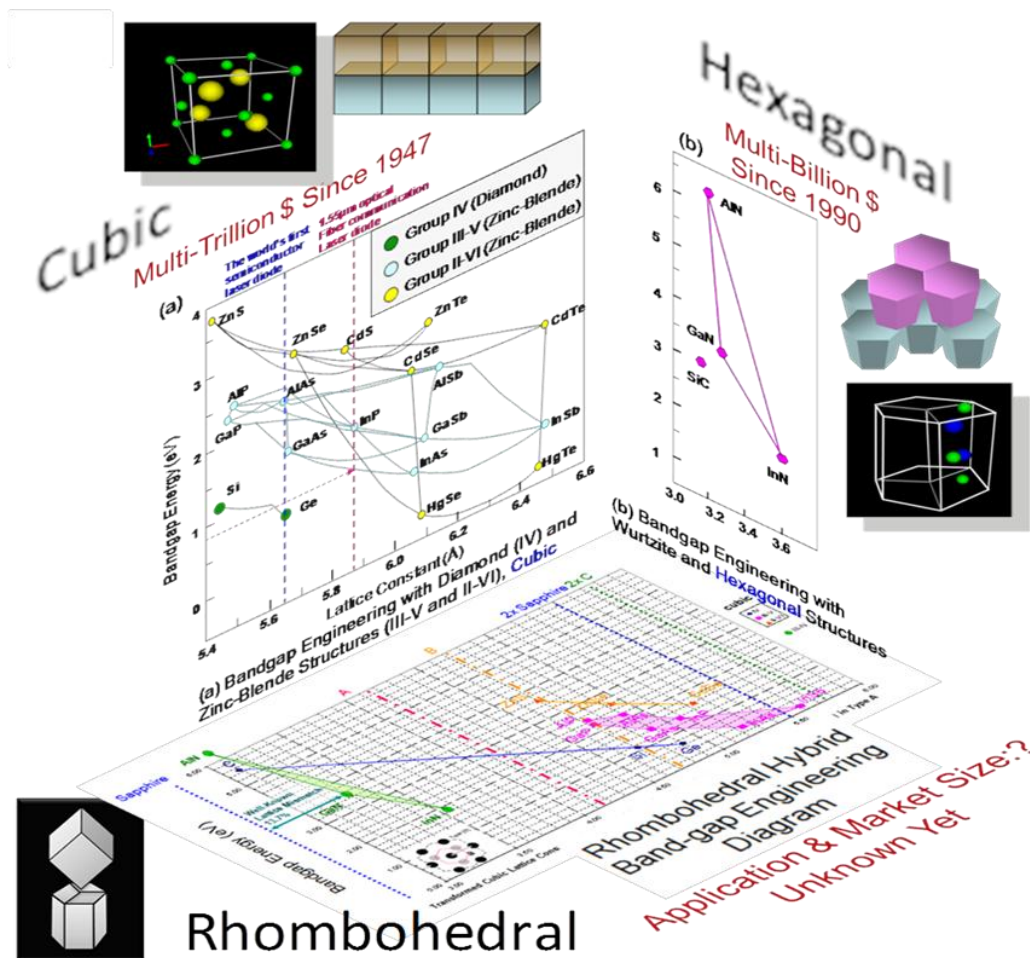


Figure 33. Bandgap engineering diagrams and epitaxy schemes for cubic, hexagonal, and rhombohedral crystal systems (ref. 34).

The other category for semiconductors is the hexagonal crystal structure, which encompasses the wide bandgap III-Nitrides (GaN, AlN, InN), the ZnO group, and the SiC high temperature semiconductors. These hexagonal semiconductors are used in light emitting diodes (LEDs), laser diodes, and high temperature semiconductor sensors, which have formed a multi-billion dollar market since the 1990s. However, these two groups of semiconductors (cubic and hexagonal) have not been integrated into a singular crystal form because of their differences in structure.

That is, until recently, when the NASA LaRC team developed unprecedented crystalline rhombohedral SiGe on trigonal sapphire substrates (ref. 34–36). This innovative epitaxial technology creates a third bandgap engineering diagram (Figure 33 and Figure 34) that opens up a new horizon for hundreds of novel hybrid crystal structures between cubic semiconductors (Si, Ge, GaAs, InP, etc.) and trigonal crystals such as sapphire. Since this new hybrid crystal structure can make hundreds of new semiconductor materials and thousands of new device structures possible, it is expected to have various applications in order to match market demands in the near future.

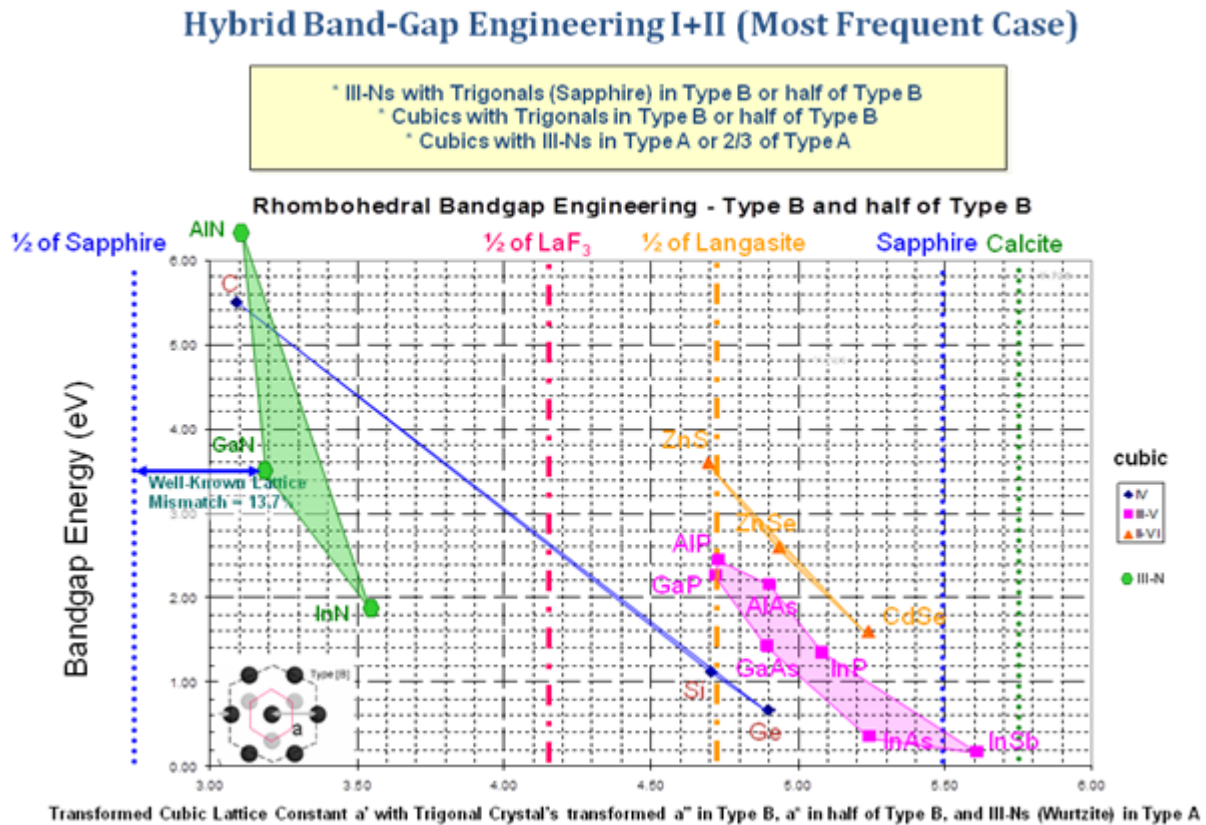


Figure 34. Rhombohedral hybrid bandgap engineering diagram shown in Figure 33.

Sapphire has a trigonal symmetry with a rotation of 120 degrees and is commonly described in hexagonal axis coordinates. LaRC's rhombohedral epitaxy uses an alignment of the [111] crystallographic direction of cubic SiGe on top of the [0001] crystallographic direction of the sapphire basal plane (c-plane) as shown in Figure 35 and Figure 36. This new epitaxial configuration follows the cubic—rhombohedral—trigonal symmetry while conventional epitaxy

technology follows the cubic—tetragonal—orthorhombic symmetry as shown in Figure 36. Single crystal growth in this new configuration was thought to be impossible because of the formation of a high density of twin defects.

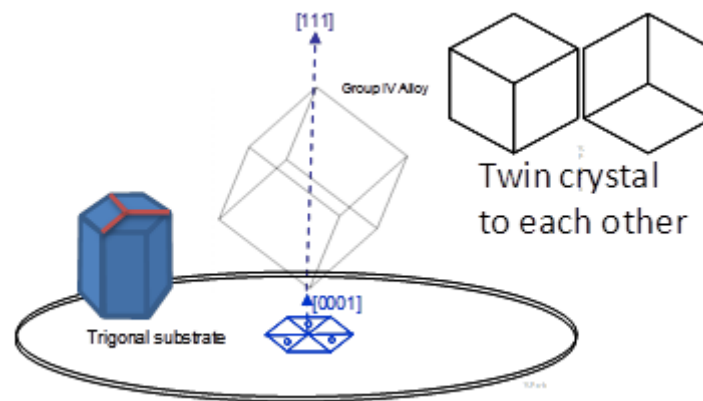
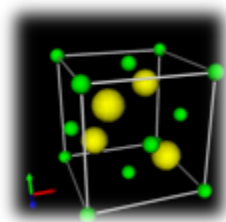
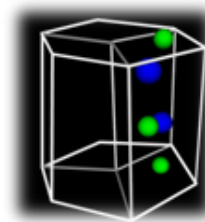


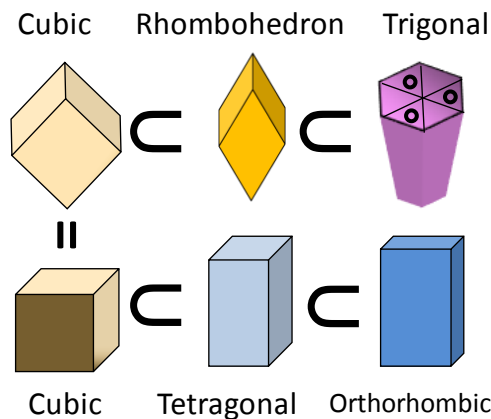
Figure 35. Crystallographic alignment of a cubic (111) crystal on a trigonal (0001) substrate (ref. 36).



(a) Cubic structure of SiGe.

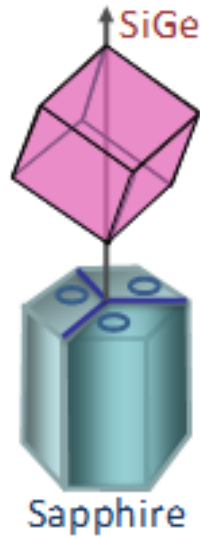


(b) Trigonal structure of sapphire.

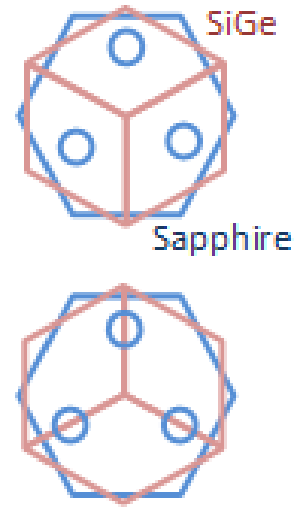


(c) Crystal symmetry relations of cubic, tetragonal, orthorhombic, rhombohedral, and trigonal structures.

Figure 36. Crystal structures and relationships (ref. 37).



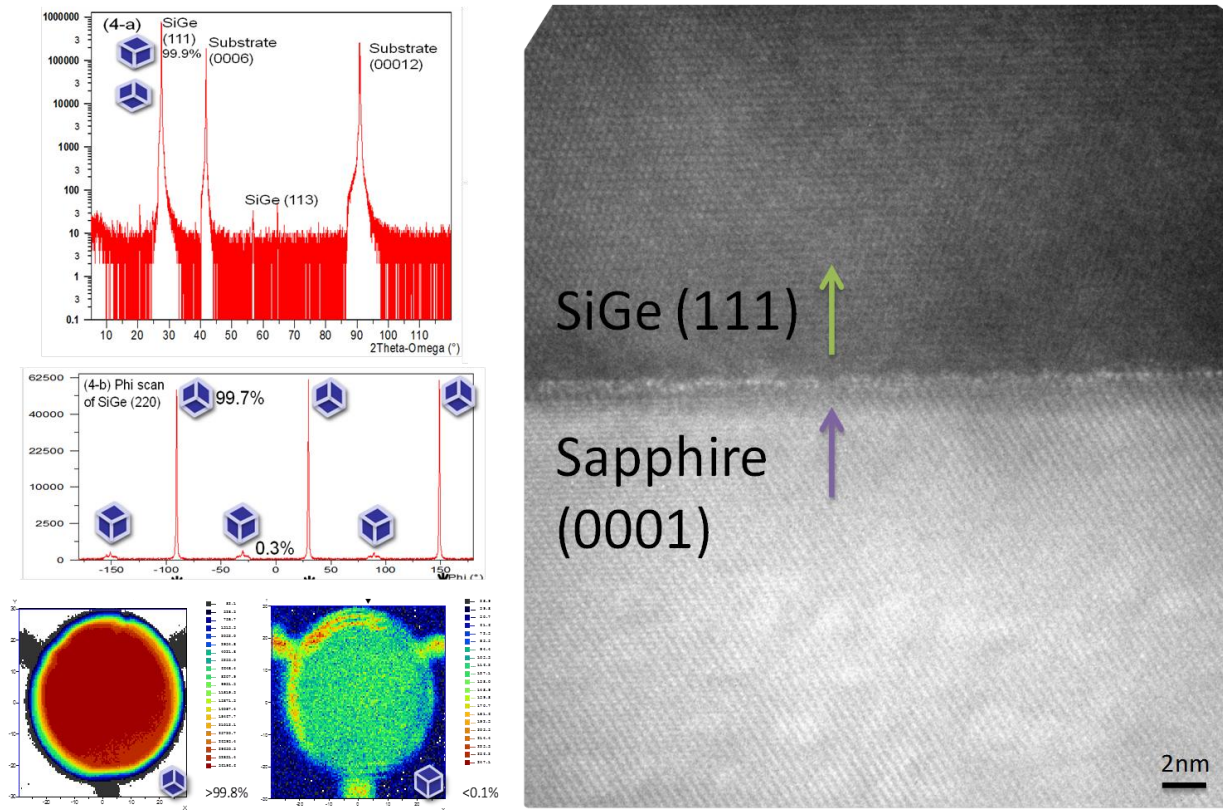
(d) Rhombohedral epitaxy of SiGe on sapphire.



(e) Two possible in-plane orientations.

Figure 36. Concluded.

Two new x-ray diffraction (XRD) methods were invented by the LaRC team to solve this problem of characterizing these twin defects (ref. 38 and 39). XRD is a scattering phenomenon whereby x-ray energy photons interact with the charge density of electrons within a material. If these electrons are bound to atoms that are arranged in a periodic way within a crystal, then constructive and destructive interference will occur along certain directions. This interference can be used to probe structural information from the crystalline sample. Figure 37 shows various XRD data for rhombohedrally grown SiGe on c-plane sapphire: (i) a symmetric θ - 2θ scan demonstrating nearly single-crystalline (111) oriented SiGe, (ii) a ϕ scan of the SiGe (220) reflection demonstrating nearly no twinning, and (iii) spatial wafer maps of the majority and minority twinning demonstrating that twin defects exist only at the edge of the wafer. Transmission electron microscope (TEM) images (Figure 37) confirm an almost perfect atomic resolution lattice structure for this rhombohedrally grown SiGe on c-plane sapphire.



(a) XRD methods.

(b) Atomic resolution TEM image. (ref. 40).

Figure 37. Rhombohedrally grown single crystalline SiGe on trigonal c-plane sapphire.

Therefore, a state-of-the-art (SOA) electron-beam (e-beam) growth chamber was designed by the LaRC team to facilitate and enhance the materials research on rhombohedral SiGe and other new material systems for green energy applications (e.g., SiGe QW solar cells and TE devices).

SECTION 6 FABRICATION OF RHOMBOHEDRAL SiGe ON SAPPHIRE

This SOA growth chamber enables physical vapor deposition growth with atomic precision and chemical control. Figure 38–Figure 40 show the CAD design, rendered CAD view, and photographs of the SOA e-beam growth chamber, respectively.

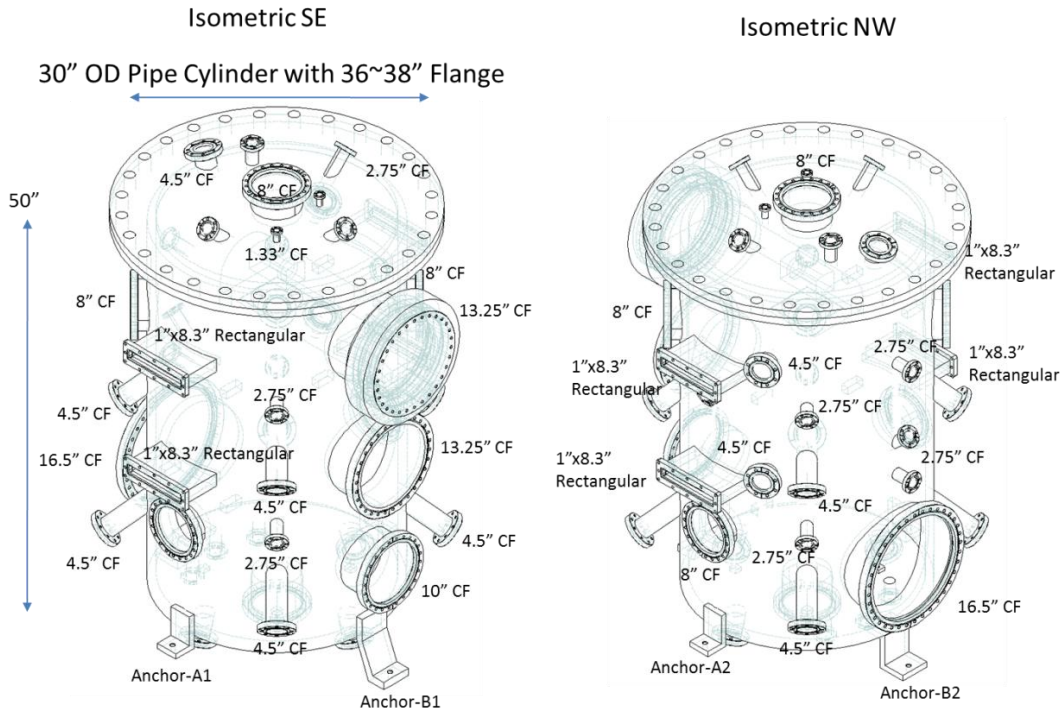


Figure 38. Three-dimensional CAD design of the SOA e-beam growth chamber.

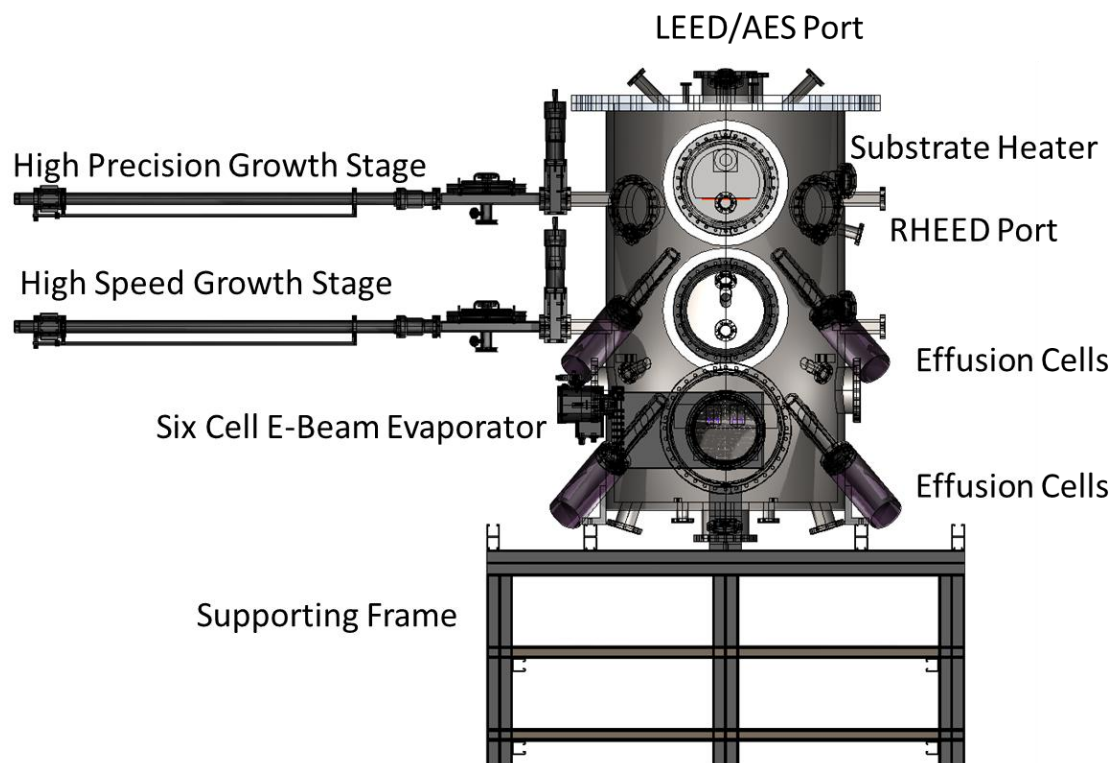


Figure 39. Three-dimensional rendered CAD view of the SOA e-beam growth chamber.

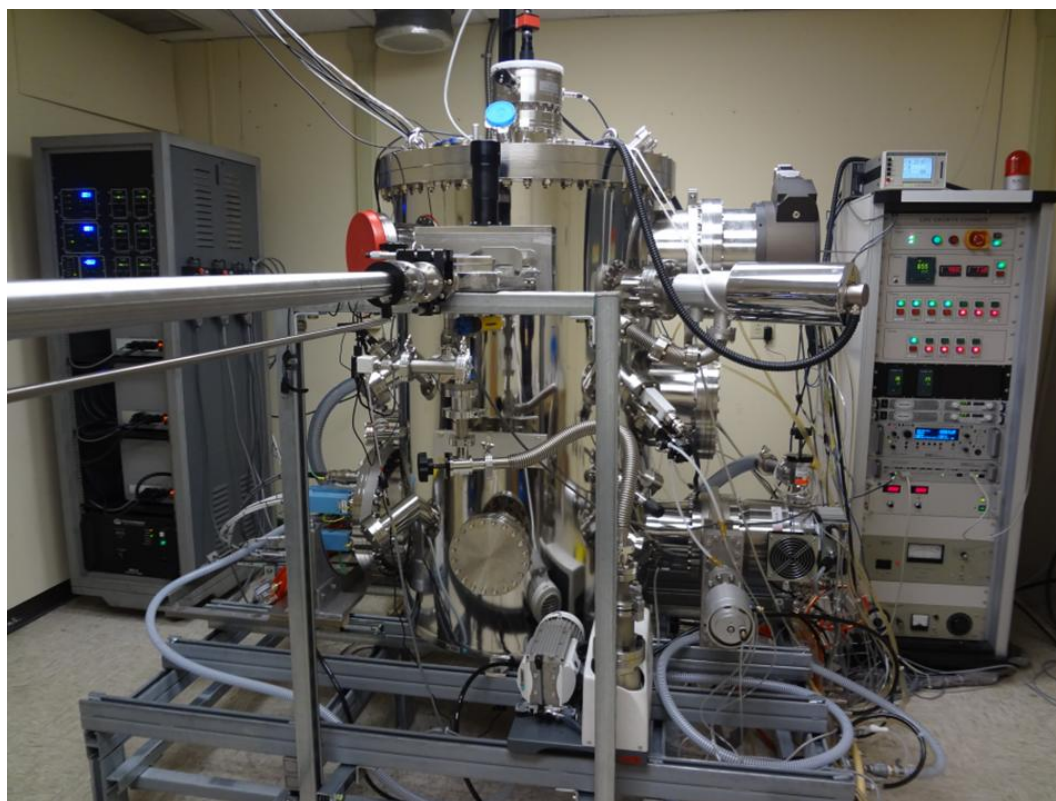


Figure 40. Photograph of the SOA e-beam growth chamber.

The growth chamber has a two-angle (in-plane and vertical) rotatable substrate heater, as shown in Figure 41, that can reach temperatures of up to 1200° C (Figure 42a). It has a continuous 360 degree in-plane rotation with variable speeds to accommodate uniform deposition of up to 6 inch wafers (Figure 43) and a vertical ± 180 degree rotation made possible with a ferro-fluid sealed rotatable 13.25 inch conflat (CF) flange. Growth capabilities on 6 inch wafers are important because most industrial companies will move from 4 inch wafers to 6 inch wafers within a few years. The vertical rotation allows *in-situ* characterization of the wafer with low energy electron diffraction (LEED). The substrate heater can accommodate 6 inch wafers through an 8 inch load-lock port that is connected to the growth chamber with 8.3 inch square flanges. Several automated wafer delivery and process systems may be installed and connected by using these 8.3 inch square flanges as entry and exit ports.

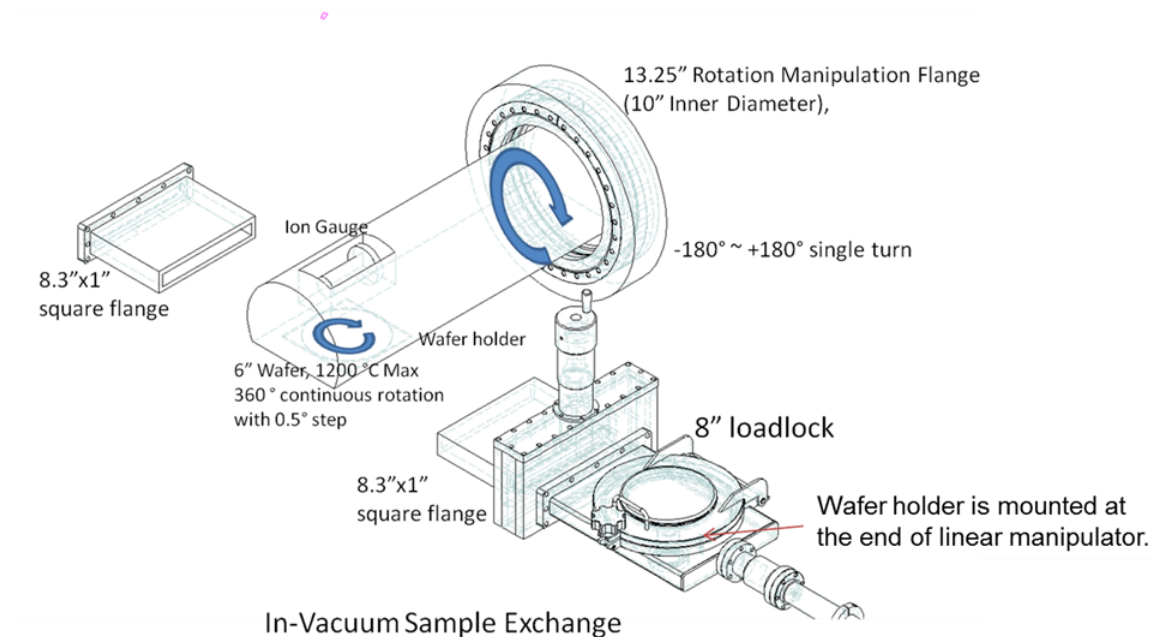
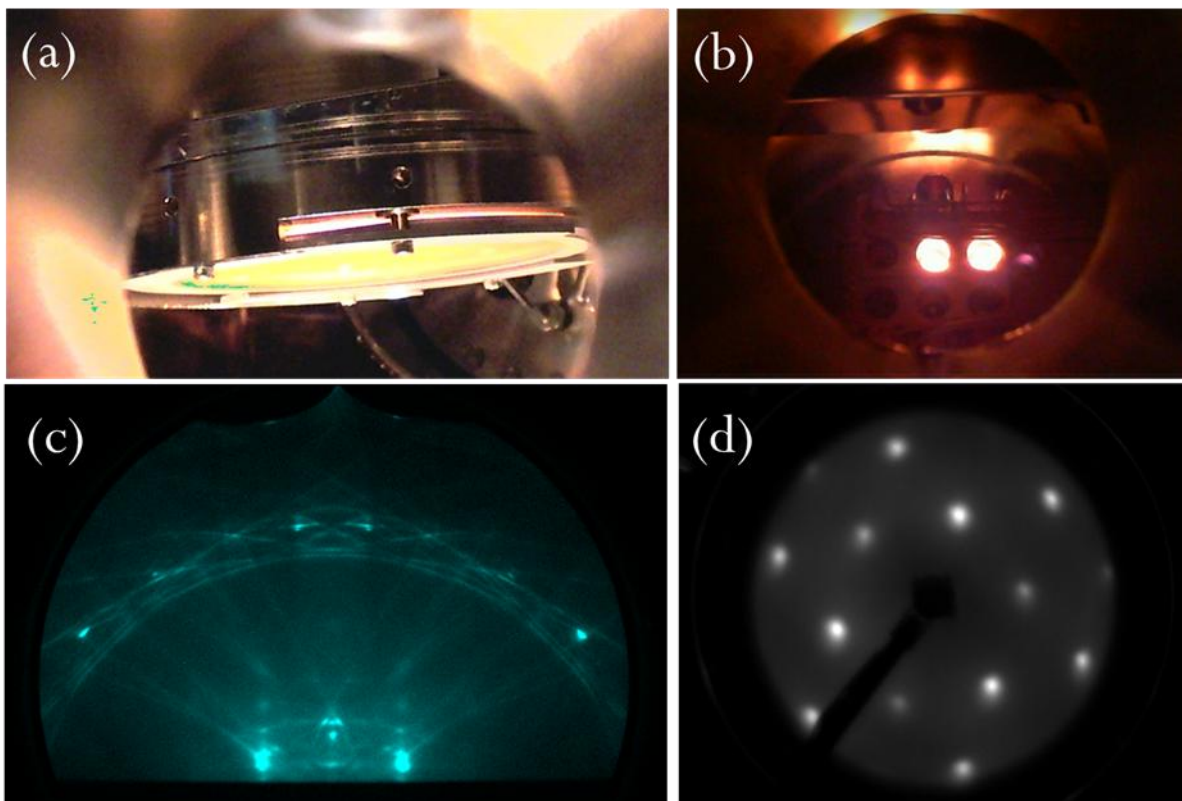


Figure 41. Dual rotation substrate heater module with entry/exit flanges for load-lock assembly.



(a) Six inch substrate heater. (b) 10 keV six-cell e-beam evaporator.
 (c) RHEED pattern of sapphire (0001). (d) LEED pattern of sapphire (0001).

Figure 42. Various components of the e-beam growth chamber.

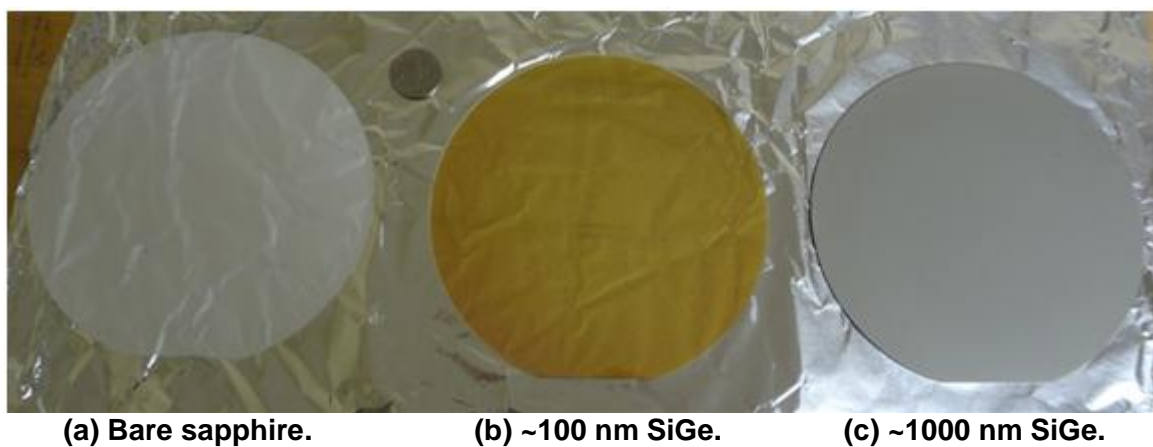


Figure 43. Fabricated rhombohedral SiGe samples on 6 inch c-plane sapphire wafers. A quarter dollar coin is shown for size comparison.

Deposition of materials was performed in an ultra-high vacuum (UHV) chamber capable of achieving base pressures in the 10^{-8} Torr range. The UHV chamber is equipped with a six-cell

electron-beam evaporator that can produce a physical vapor molecular beam flux of up to 4000° C by direct e-beam heating (Figure 42b). In addition to the e-beam evaporator, the growth chamber has two dopant effusion cells, one for high temperature (up to 2400° C) and one for low temperature materials (up to 1350° C). The sample growth was monitored with 14-bit high dynamic range (HDR) cameras that were installed outside of the UHV chamber. *In-situ* characterization of the sample growth was possible with 30 keV reflection high energy electron diffraction (RHEED), LEED, and retarding field analyzer (RFA) Auger electron spectroscopy (AES) instruments for atomic surface structure monitoring, growth rate monitoring, and chemical analysis (Figure 42c and d). The upper 13.25 inch CF flange port is for atomic precision material growth with *in-situ* characterization (RHEED, LEED, etc.), while the lower stage was designed with a very short distance from the six-cell e-beam evaporator in order to achieve a very high growth rate of up to 278 nm/s.

The chamber was designed for expansion capabilities to accommodate effusion cells, direct current (DC) and radio frequency (RF) plasma sources, and sputtering sources to allow multiple methods of depositing materials, such as GaN growth with a nitrogen plasma. Different assisted growth techniques are possible, such as direct e-beam heating and ion-beam assisted sputter deposition. The *in-situ* monitoring capabilities may also be expanded to include glancing angle ellipsometry and quartz thickness monitors. The material sources in the six-cell e-beam evaporator are not limited to only Si and Ge, but can support high temperature refractory metals such as tungsten, zirconium, and hafnium.

Although very high quality rhombohedral SiGe layers on c-plane sapphire wafers with 99.7 percent single crystal quality have been previously obtained by the NASA LaRC team (ref. 35), the reproducibility of similar high quality epitaxial layers had been difficult to achieve prior to the upgrade to the six-cell e-beam growth chamber with its tight process control. These instabilities arise from the difficulty of controlling the growth parameters, in particular the sapphire wafer substrate temperature, because of its transparent nature in the infrared (IR) and visible spectra. This causes most of the heating due to IR light to be lost because it passes directly through the sapphire wafer causing the actual temperature of the sapphire wafer surface to be much lower than the temperature measured by the thermocouple of the substrate heater. Therefore, backside carbon-coated sapphire wafers are similarly prepared to absorb heat, thus, maintaining accurate temperatures during the SiGe growth. This has allowed very reliable fabrication of highly single crystalline (>99.5 percent) SiGe layers in consecutive growth runs with identical growth parameters.

SECTION 7

CHARACTERIZATION OF RHOMBOHEDRAL SiGe ON SAPPHIRE

XRD data of these highly single crystalline (>99.5 percent) SiGe layers on c-plane sapphire wafers are shown in Figure 44. A symmetric θ - 2θ scan, which probed the surface normal direction of the sample, showed only the SiGe (111) reflection at $2\theta \sim 27.5$ degrees along with the Al_2O_3 (003), (006), (009), and (0012) reflections. No other SiGe reflections, such as the (220), (311), or (400), appeared in the symmetric scan, verifying that all of the crystallites were oriented in the [111] direction. The in-plane orientation of the crystallites was measured with a ϕ scan of the SiGe (220) reflections. Three strong reflections offset by 120 degrees in the ϕ scan indicated the majority in-plane orientation of the SiGe, and three small peaks indicated the 60 degrees rotated (twinned) minority in-plane orientation. The intensity was plotted in a log-scale, and the twin crystal's peak was very weak compared with the majority single crystal's peak. The majority percentage of the SiGe crystallites can be determined by comparing the integrated areas under each peak. Single crystalline SiGe layers greater than 99.5 percent were fabricated in these growth runs according to these XRD measurements shown in Figure 44. The best sample grown to date is >99.8 percent single crystalline.

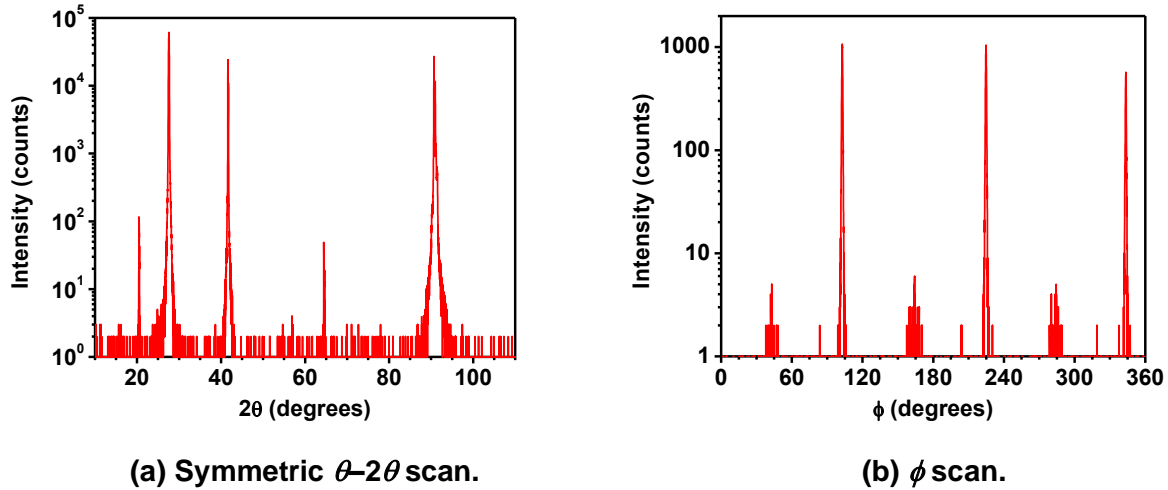


Figure 44. Symmetric θ - 2θ XRD scan shows only the SiGe (111) reflection at $2\theta \sim 27.5$ degrees along with the Al_2O_3 (003), (006), (009), and (0012) reflections. SiGe (220) ϕ scan shows three strong reflections (offset by 120 degrees) with three small reflections rotated 60 degrees from them indicating greater than 99.5 percent in-plane orientation of the SiGe.

In addition to the crystalline quality of the SiGe samples, the amount of defects present in the sample is utterly important to device performance. The industry standard to determine the amount of defects is a Secco etch-pit density measurement (ref. 41) that uses an etchant composition of solvent, hydrofluoric acid (HF), and $\text{K}_2\text{Cr}_2\text{O}_7$ oxidizer as shown in Table 7. It reveals line defects or dislocations (LDs) as pits and point defects as shallow pits or hillocks. Although a Secco etch works on all crystallographic orientations, the etching effect on {111} wafers is slightly different from that of {100} wafers.

Table 7. Etchant composition of Secco etch-pit density test and its effects (ref. 41).

Composition (Mol %)			Results on {100}	
H2O + CH3COOH (HAc) (Solvent)	HF	CrO3 + HNO3 (Oxidizer)	Line defects	Point defects
67.6	32.2	0.17	Pits	Shallow pits or hillocks

A Secco etch was performed on SiGe layers on c-plane sapphire. Figure 45 shows that rhombohedral SiGe grown on c-plane sapphire has a very small number of etch pits ($\sim 10^2$ per cm^2) indicated by red circles and no LDs (i.e., no cross-hatch pattern) after Secco etching for three seconds. On the contrary, SiGe grown on Si (100) wafers typically show a high density of etch pits and LDs on the order of about 10^4 per cm^2 . Figure 46 shows a comparison of a Secco etch pit test between a typical $\text{Si}_{65}\text{Ge}_{35}$ film on a Si (100) wafer and rhombohedral $\text{Si}_{22}\text{Ge}_{78}$ on a c-plane sapphire wafer. The rhombohedral $\text{Si}_{22}\text{Ge}_{78}$ grown on c-plane sapphire has a threading dislocation pit (TDP) density of 1.9×10^2 per cm^2 , no visible line defects, and no cross-hatch patterns, while $\text{Si}_{65}\text{Ge}_{35}$ on a Si (100) wafer has a TDP density of 3.9×10^4 per cm^2 , LD density of 1.73×10^4 per cm^2 , and many cross-hatch patterns. Therefore, rhombohedral SiGe on c-plane sapphire has approximately 200 times less defect densities than conventional SiGe on Si (100) wafers as measured with Secco etching tests.

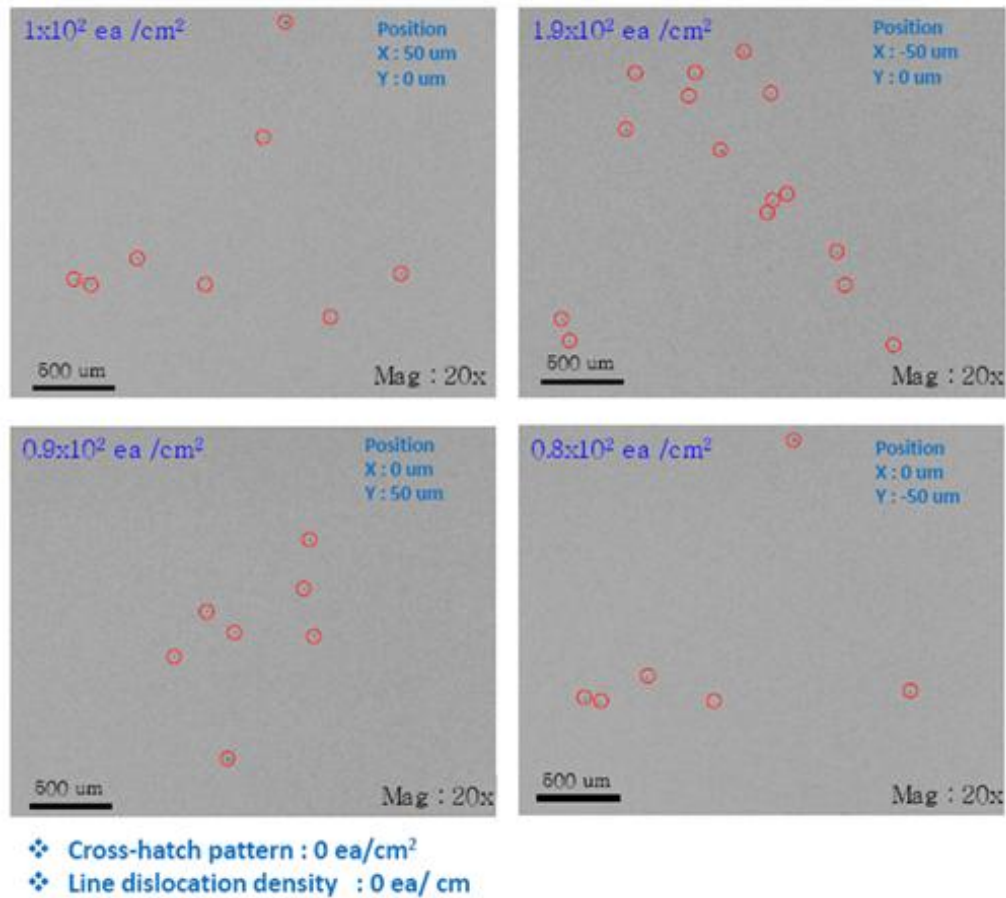
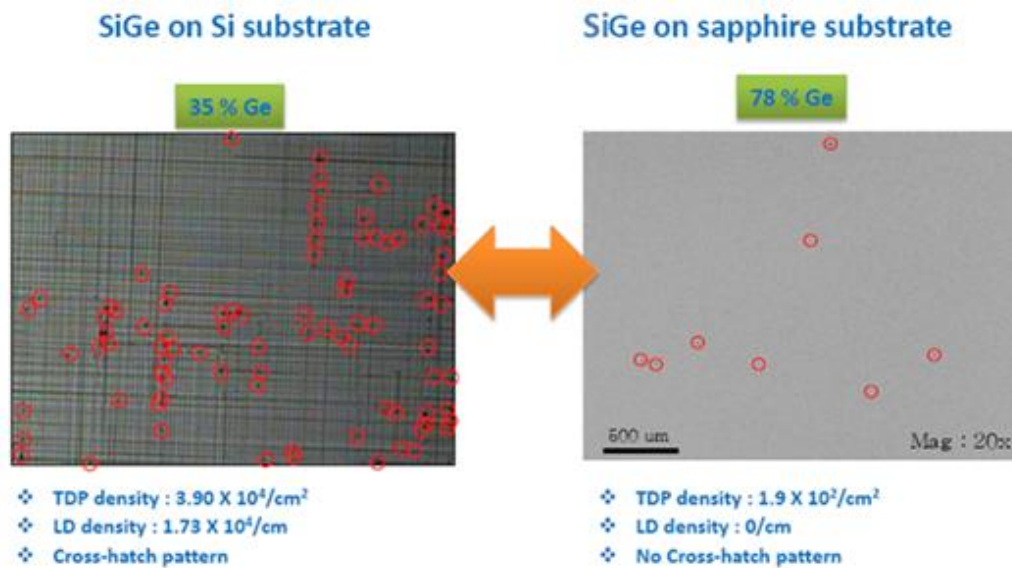


Figure 45. Four Secco etch-pit density tests on rhombohedral SiGe grown on c-plane sapphire, where etch-pits (red circles) exist but line dislocations do not.



(a) Si₆₅Ge₃₅ on Si(100) wafer.

(b) Si₂₂Ge₇₈ on c-plane sapphire.

Figure 46. Secco etch-pit test results.

Another important parameter to achieve for device applications (particularly electronic micro-device and solar cell fabrication) of rhombohedral SiGe on c-plane sapphire is a uniform and smooth surface. Figure 47 shows the mirror-like surfaces of 100 nm thick SiGe on 2 and 4 inch c-plane sapphire wafers. Planar TEM real-space and reciprocal-space images (not shown) indicate that these SiGe samples are single crystalline and oriented along the [111] direction.

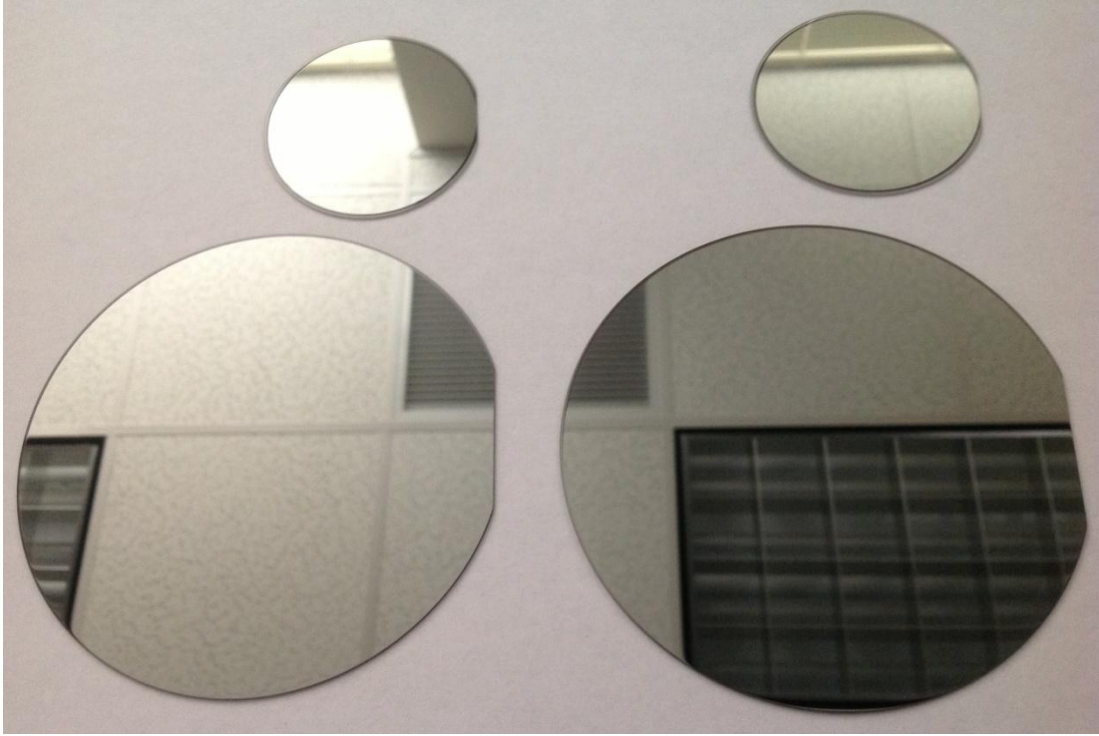
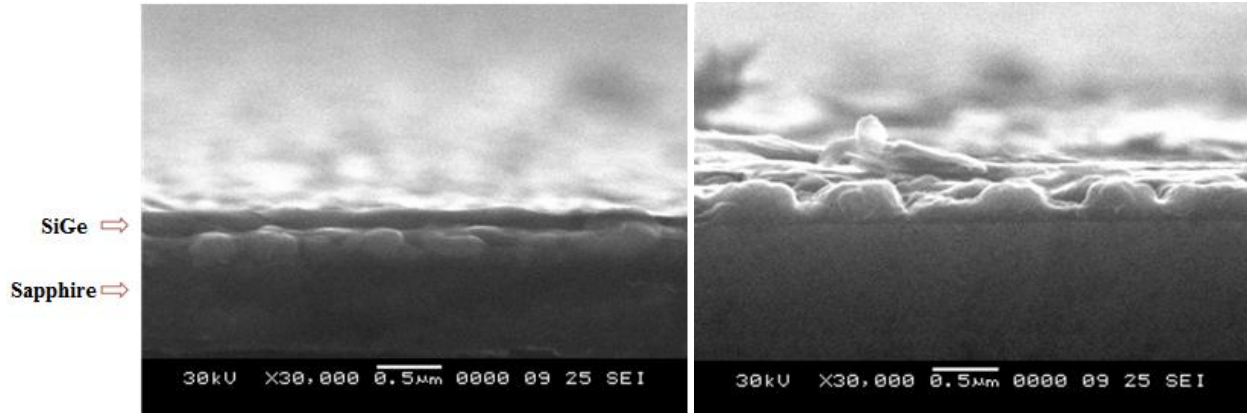


Figure 47. Photograph of ~100 nm thick SiGe samples with mirror-like surfaces.

The growth of rhombohedral SiGe on c-plane sapphire has been shown to follow the Stranski-Krastanov (SK) growth mode through cross-sectional scanning electron microscope (SEM) analysis. In the SK growth mode, the epitaxial layer grows in a layer-by-layer (Frank-Van der Merwe) growth mode until the layer thickness reaches some critical thickness. Coherent 3-D island growth begins after this critical thickness is reached and the film becomes a rough surface (Figure 48). The critical thickness where this transition from 2-D layer-by-layer growth mode to 3-D island growth mode occurs is determined by epitaxial strain from the lattice mismatch between the epitaxial layer (i.e., SiGe) and substrate (i.e., sapphire) and can be tailored by the Si and Ge concentrations.



(a) Layer-by-layer growth mode.

(b) SK growth mode.

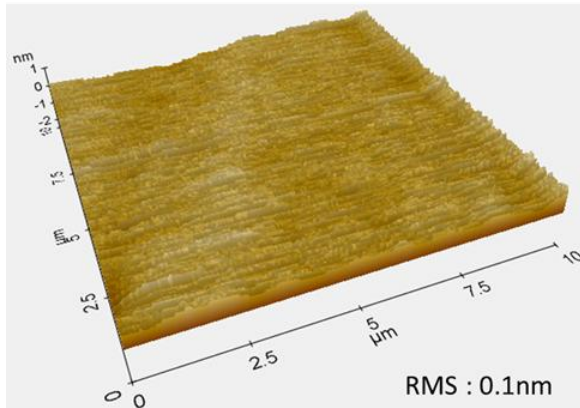
Figure 48. Cross-sectional SEM images of a smooth SiGe layer on c-plane sapphire in layer-by-layer growth mode and a rough SiGe layer on c-plane sapphire in SK growth mode. The SK growth mode begins layer-by-layer and transitions to coherent 3-D island growth at a critical thickness.

The coherent 3-D island formation is a result of accumulated strain on the hillocks of atomic lattices in 2-D layer-by-layer growth. The residual stress from the lattice mismatch between SiGe and c-plane sapphire distorts the 2-D flat layer causing a slight bending of the atomic lattices. More bending occurs upon the distorted lattice sites as the deposition continues, and the SiGe layer becomes thicker. The 3-D island growth starts at the critical thickness where the formation of a 3-D island requires less energy than the formation of a distorted 2-D flat layer.

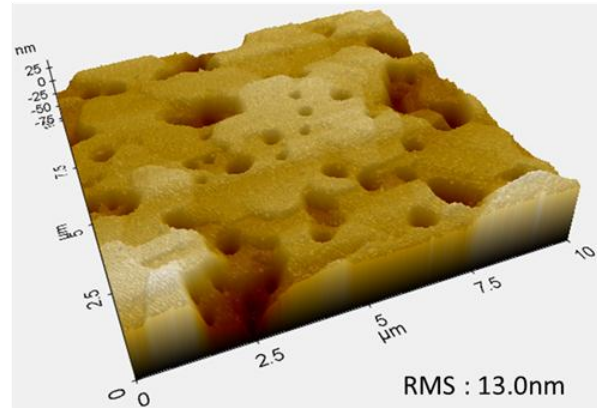
Therefore, it is important to control the SiGe composition to reduce the lattice mismatch with the c-plane sapphire and maintain an appropriate molecular beam flux rate to ensure smooth layer-by-layer growth. SK growth theory shows that the epitaxial layer can grow very thick in a smooth layer-by-layer growth mode in the nearly lattice-matched condition.

Atomic force microscope (AFM) measurements show the surface morphology and root mean square (RMS) roughness of a thin 100 nm $\text{Si}_7\text{Ge}_{93}$ film and a several micrometers thick $\text{Si}_{16}\text{Ge}_{84}$ film (Figure 49). The RMS roughness of the thinner $\text{Si}_7\text{Ge}_{93}$ film was 8.1 nm as compared to 13 nm for the thicker $\text{Si}_{16}\text{Ge}_{84}$ film. The 8.1 nm roughness arises from the small 3-D islands forming on top of the layer-by-layer growth.

Sample Name : SG 504

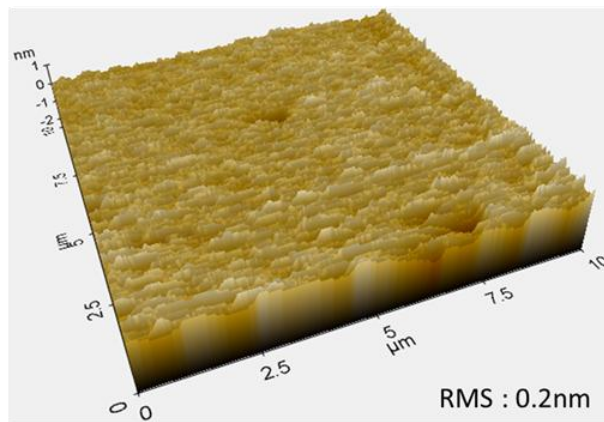


c-Al₂O₃

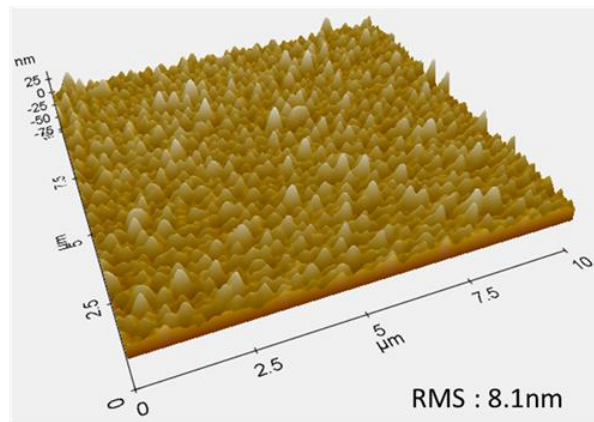


Si₁₆Ge₈₄ on c-Al₂O₃
(Thickness of SiGe : several μ m)

Sample Name : SG 607



c-Al₂O₃



Si₇Ge₉₃ on c-Al₂O₃
(Thickness of SiGe : \sim 100nm)

Figure 49. AFM images of bare c-plane sapphire and different thicknesses of rhombohedral SiGe layers on c-plane sapphire.

SECTION 8

QUANTUM WELL SOLAR CELL APPLICATIONS

The conventional silicon-on-sapphire (SOS) technology developed during the 1980s uses the epitaxy of Si on r-plane (1-102) sapphire. SOS became crucial in devices using silicon-on-insulator (SOI) wafers because sapphire is one of the best insulators. The SOS wafer provides electrically separated regions because of the insulating properties of the sapphire itself, as opposed to other typical devices where the regions are electrically separated using reverse bias between the substrate and device area. The space charge region (carrier depletion region) in the reverse bias case is very thin (micrometer range), and, thus, the capacitance between a device and the substrate is high and causes the device to have a leakage current at high frequency operating speeds. On the contrary, sapphire is very thick and has an ultra-small capacitance thereby reducing parasitic capacitance and leakage currents at high operating frequencies. Peregrine Semiconductor, who patented ultra-complementary metal-oxide-semiconductor (Ultra-CMOS) SOS technology, built numerous RF ICs such as RF switches, digital step attenuators, phase-locked loop frequency synthesizers, prescalers, mixers/up-converters, and video graphics arrays (VGAs) with fully depleted MOS transistors, and used only a 95 nm thick silicon layer on sapphire in a PE42612 switch. The remaining silicon thickness after the poly-silicon gate stack with oxidation and recession was only 75 nm.

In rhombohedral SiGe on c-plane (0001) sapphire, the SiGe layer can be grown in layer-by-layer mode from sub-100 nm to a few hundred nanometers of thickness. Therefore, thin rhombohedral SiGe films on c-plane sapphire have many commercial applications as SOI wafers in addition to solar cell applications. While the carrier mobilities of SOI are limited by the silicon material, the mobilities of SiGe on c-plane sapphire can be a few times higher than those of silicon due to the high carrier mobilities of germanium (p-type Si: $430 \text{ cm}^2/\text{V}\cdot\text{s}$, p-type Ge: $2200 \text{ cm}^2/\text{V}\cdot\text{s}$, n-type Si: $1300 \text{ cm}^2/\text{V}\cdot\text{s}$, n-type Ge: $3000 \text{ cm}^2/\text{V}\cdot\text{s}$ at 10^{16} per cm^3 doping density). Therefore, RF devices that are made with rhombohedral SiGe on c-plane sapphire can potentially run a few times faster than RF devices on SOS wafers.

Today, SOS wafers find many applications in the following areas:

- analog-to-digital converters
- monolithic digital isolation buffers
- SOS-CMOS image sensor arrays
- patch-clamp amplifiers
- energy harvesting devices
- 3-D integration with no galvanic connections
- temperature sensors

Rhombohedral SiGe on c-plane sapphire will have these similar applications in the beginning. However, c-plane sapphire can easily accommodate wide-bandgap III-Nitride devices such as GaN, AlN, and InN. Thus, it is possible to build a hybrid crystal of cubic zinc-blende or diamond structures (group IV, III-V, II-VI semiconductors) and hexagonal wurtzite structures (group III-Nitride, ZnO semiconductors). Actually, c-plane (0001) sapphire is the most common substrate on which to grow GaN LED devices today. This unique capability to fabricate hybrid crystals on trigonal substrates such as sapphire can enable a new horizon of thousands of unprecedented applications with new novel devices beyond the application areas of SOS wafers.

In order to realize these applications and fabricate solar cells and other electronic devices, it is necessary to form p-n junctions. Boron and phosphorous, which are typical p-type and n-type dopants in silicon, can be used in SiGe to control the doping concentration. Effusion cells installed on the e-beam growth chamber are very efficient methods to inject dopants in solid phase epitaxial growth. While phosphorous has a very high vapor pressure at a low temperature range (300°C), boron requires very high temperatures (1700°C) in order to evaporate it. Two hot-lip effusion cells, a low temperature cell for phosphorous and a high temperature cell for boron were installed to avoid cold spot deposition at the opening of the crucible. Since the dopant vapor from effusion cells has an exponential dependence on the temperature, very tight temperature control with proportional-integral-derivative (PID) feedback is required. A delicate fine tuning with PID feedback control was performed to allow stable doping control.

This research is ongoing and now partly supported by NASA LaRC under the Creativity and Innovation (C&I) program to develop QW solar cell devices, where these p-n junctions are now being fabricated and studied. They are explained in more detail here.

Silicon and germanium have different energy levels in their conduction and valence bands. Therefore, if these two materials meet each other in a layer-by-layer structure, each layer can collect electrons and holes separately in QWs as shown in Figure 50. Generally, the mobility of a semiconductor decreases as the doping density becomes higher because the ionized dopant atoms scatter the mobile electrons and holes. Since this leads to a low mobility that equates to longer times for carriers to reach the electrodes, higher current losses occur because of thermal lattice vibrations and electron-hole recombination processes. Once the QWs are formed with an intrinsic layer or low-doped layer, electrons and holes can be separated from the higher-doped regions. The right side of Figure 50 shows that the mobility in a QW can be increased 10 times compared with a high-doped layer. Also, germanium has three times higher electron and hole mobilities than silicon. Therefore, QWs with low-doped layers can enhance the power conversion efficiency of new QW solar cells above the current theoretical limit of 25 percent for pure silicon solar cells. Figure 51 shows the absorption spectra of silicon and germanium. While silicon solar cells can absorb in the wavelength regime up to 1100 nm, germanium solar cells can use more of the solar spectrum, up to 1800 nm.

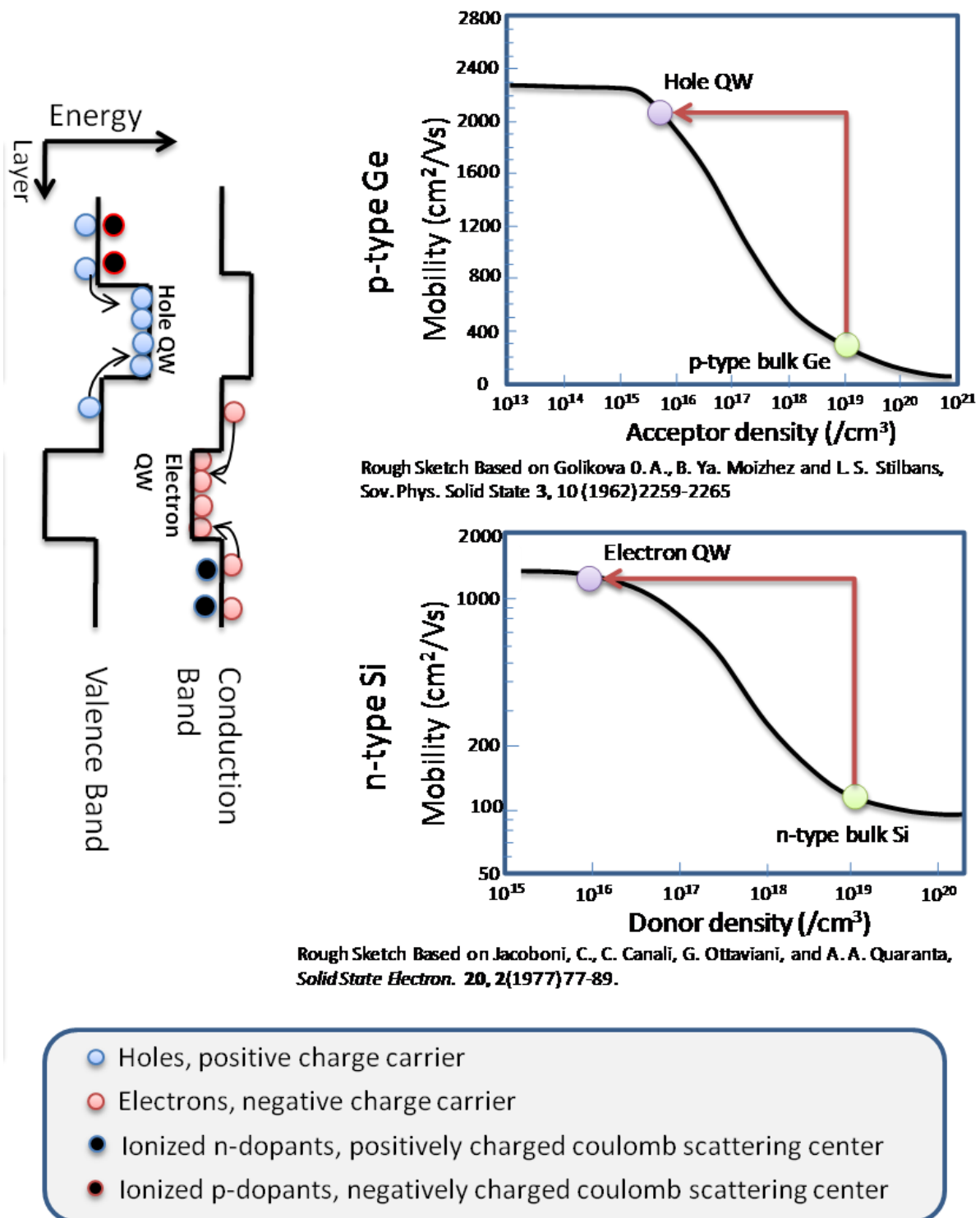
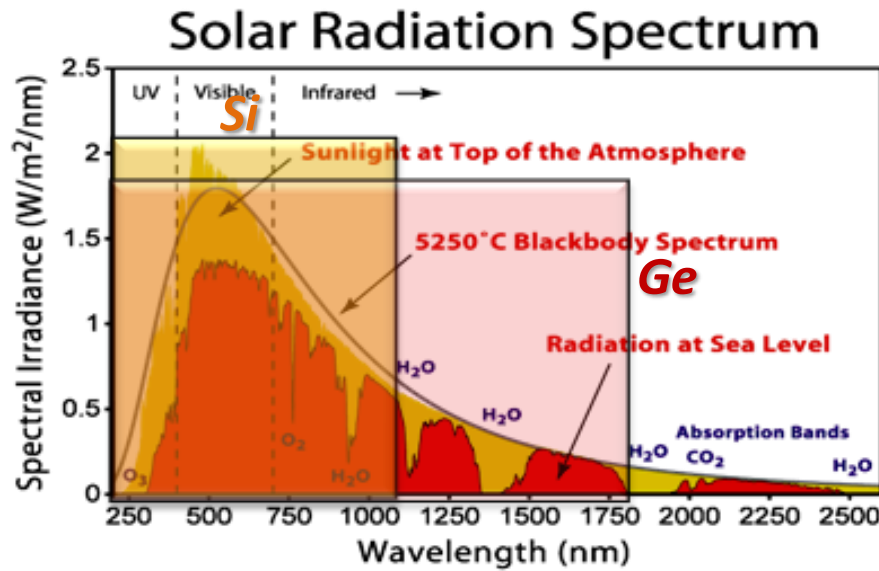


Figure 50. Quantum well structure of SiGe (left) and the mobility enhancement of electrons and holes in a QW (ref. 42 and 43).



*From American Society for Testing and Materials (ASTM) Terrestrial Reference Spectra

Figure 51. Energy absorption regimes of silicon and germanium solar cells with respect to the solar spectra.

Sapphire wafers are completely transparent in the visible spectrum as shown in the inset of Figure 52. Therefore, the rhombohedral SiGe solar cell can use both the front and rear surface of the transparent sapphire to absorb light, whereas conventional solar cells only use one surface for light absorption (Figure 53). If the light enters from the rear side of the transparent sapphire substrate, the metal electrodes on the front side do not block the light. Therefore, a high density of metal electrodes can be fabricated to reduce the carrier diffusion length and minimize the thermal loss of current. Also, special treatments of the sapphire surface, such as the deposition of an anti-reflection coating, are possible in order to absorb more direct sunlight and ambient light, thus maintaining a higher light collection efficiency.

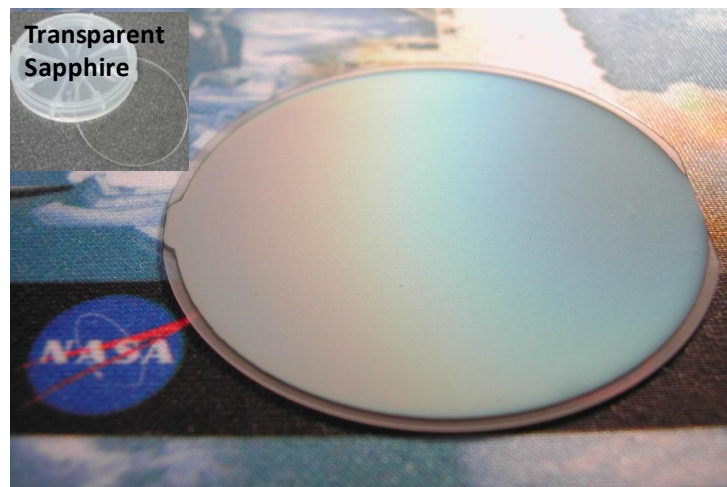


Figure 52. Rhombohedral SiGe on c-plane sapphire and transparent double-side polished sapphire wafer (inset).

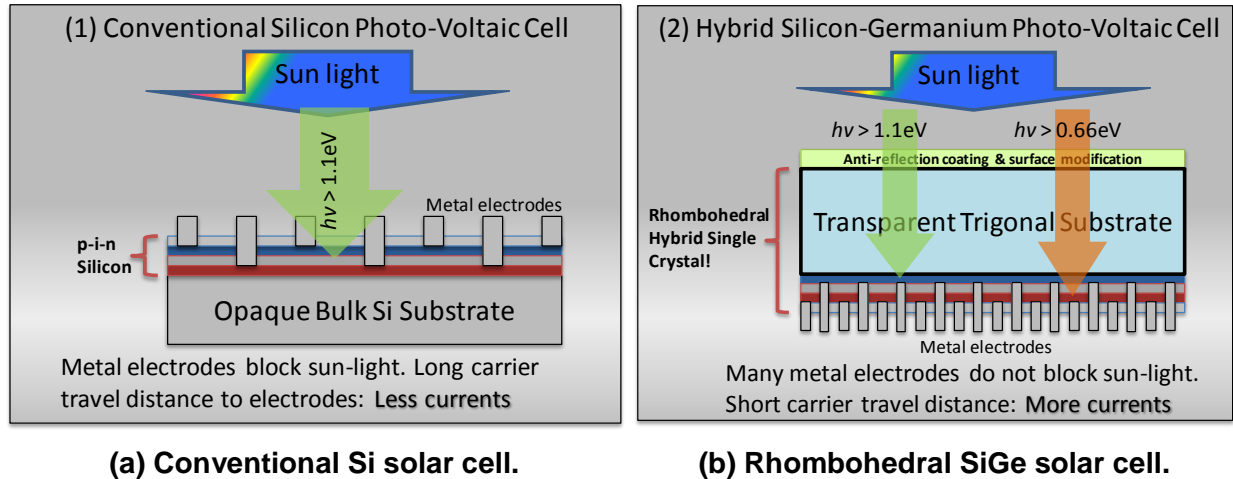


Figure 53. Comparison of a conventional silicon solar cell that receives sunlight from the front side where electrodes shadow sunlight and a rhombohedral SiGe solar cell on c-plane sapphire that receives sunlight from rear side with no obstructing electrodes.

In addition, while SiGe is grown on one side of the sapphire wafer, a GaN layer can be grown on the opposite side (Figure 54). This double-sided super-heteroepitaxial hybrid crystal that was developed at LaRC can be used in many new hybrid crystal structure devices. For example, this hybrid device can absorb sunlight from the photovoltaic (solar cell) side in the daylight and illuminate colored light from the GaN LED structure on the opposite side of the sapphire wafer at night.

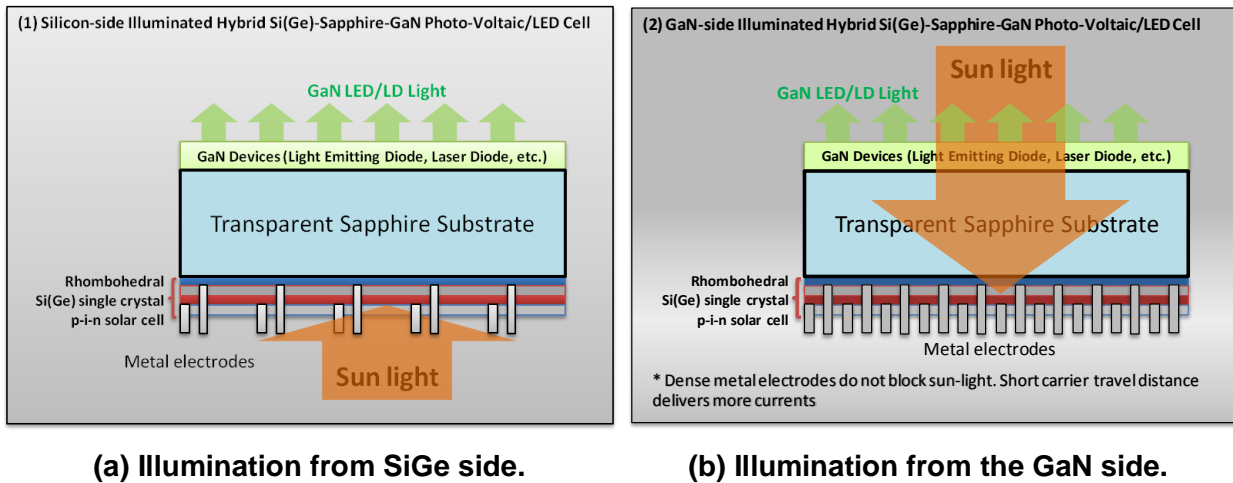


Figure 54. SiGe/Sapphire/GaN hybrid crystal structure device on a double-sided sapphire wafer with illumination from each side.

SECTION 9

HIGH TEMPERATURE THERMOELECTRIC DEVICE APPLICATIONS

In addition to QW solar cells, rhombohedral SiGe also finds energy harvesting applications in TE devices (please see the next section for a detailed background on TEs). SiGe materials are one of the most frequently used TE materials for radioactive thermoelectric generators (RTGs) because of their high operating temperatures ($>1000^{\circ}\text{C}$) that can achieve a large electric power output per kg (ref. 44 and 45) and were used in many of NASA's deep space explorers (e.g., Voyager I, II, and Cassini). Rhombohedral SiGe has the potential to further improve the efficiency of these high temperature TE devices.

The crystalline quality of rhombohedral SiGe on trigonal c-plane sapphire can be well controlled via the deposition conditions as discussed in the previous section, thus suiting rhombohedral SiGe for many versatile applications. Figure 55 shows two XRD pole figures of this material with two different crystalline qualities: a highly twinned SiGe material (left) and a nearly single crystalline SiGe material (right). The single crystalline SiGe film has applications in semiconductor devices (e.g., QW solar cells) because of its high mobility, while a highly twinned SiGe film has applications in high temperature TE devices because of its phonon scattering properties.

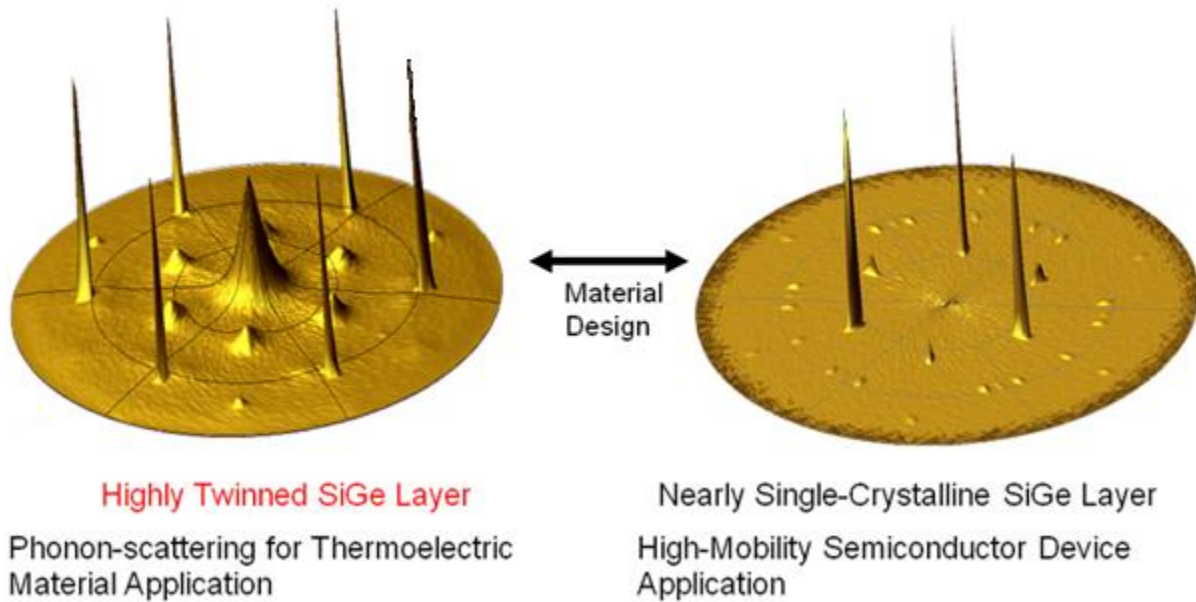


Figure 55. XRD pole figures on the SiGe (220) reflection for two SiGe materials with different crystalline qualities.

The efficiency of TE materials is measured by a TE figure of merit (FoM) that is defined by the equation in Figure 56. The FoM is the dimensionless quantity ZT , which is proportional to the Seebeck coefficient (S) squared, the electric conductivity (σ), and inversely proportional to the thermal conductivity (κ). This allows the TE FoM to be increased by optimizing these three

parameters. Figure 56 shows the increase of the FoM for a number of different materials with various operating temperature regimes.

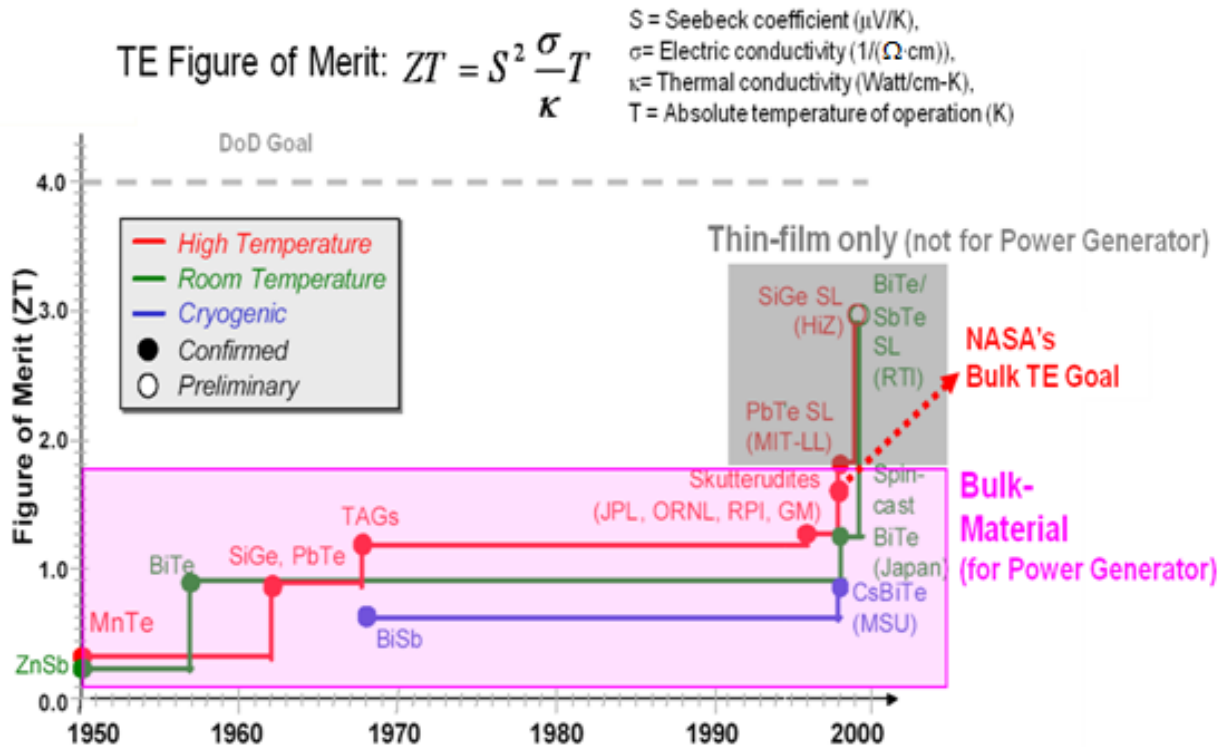


Figure 56. TE FoM equation and the historical development of TE materials at various operating temperature regimes (ref. 46).

The Seebeck coefficient is an intrinsic property of a material that is difficult to modify, therefore a more efficient TE material can be engineered by increasing the electric conductivity (σ) and decreasing the thermal conductivity (κ). This can be achieved with highly twinned SiGe, where the transfer of electric carriers along the [111] direction occurs without much boundary scattering, while off-axis phonon propagation is blocked because of twin boundaries as shown in Figure 57. Therefore, an increase in the ZT factor (FoM) can be achieved by scattering phonons at this twin boundary plane. Measurements show that the rhombohedral $\text{Si}_{15}\text{Ge}_{85}$ TE material samples show much higher carrier mobility, as well as very low thermal conductivity as shown in Figure 58. These fabricated twinned $\text{Si}_{15}\text{Ge}_{85}$ samples had 2.5 times higher electrical conductivity than bulk $\text{Si}_{15}\text{Ge}_{85}$ at the same doping concentration.

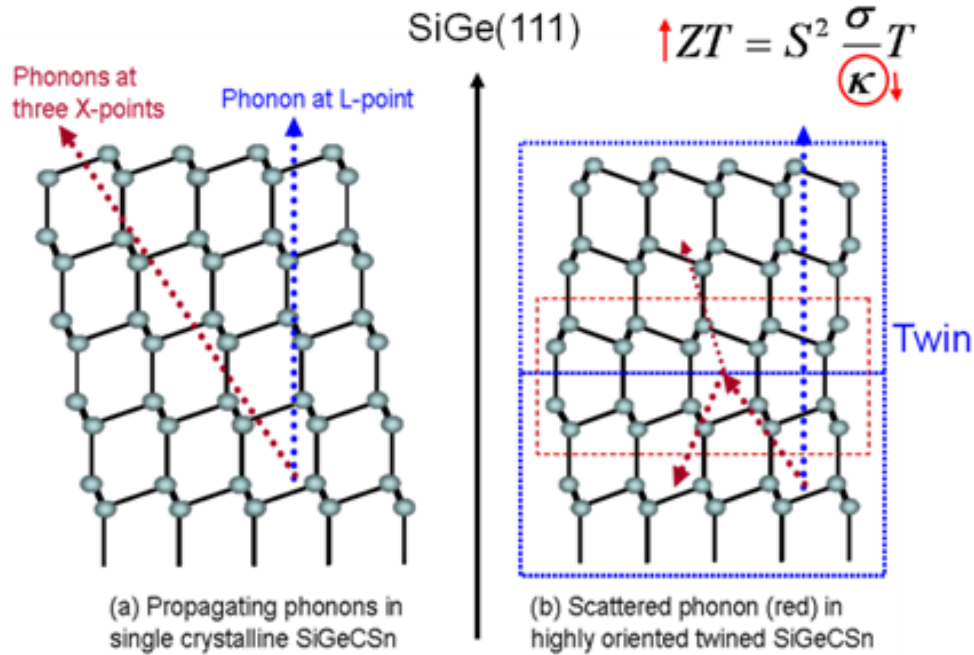


Figure 57. Thermal conductivity is lowered by phonon scattering at the stacking-fault interface of a twin crystal.

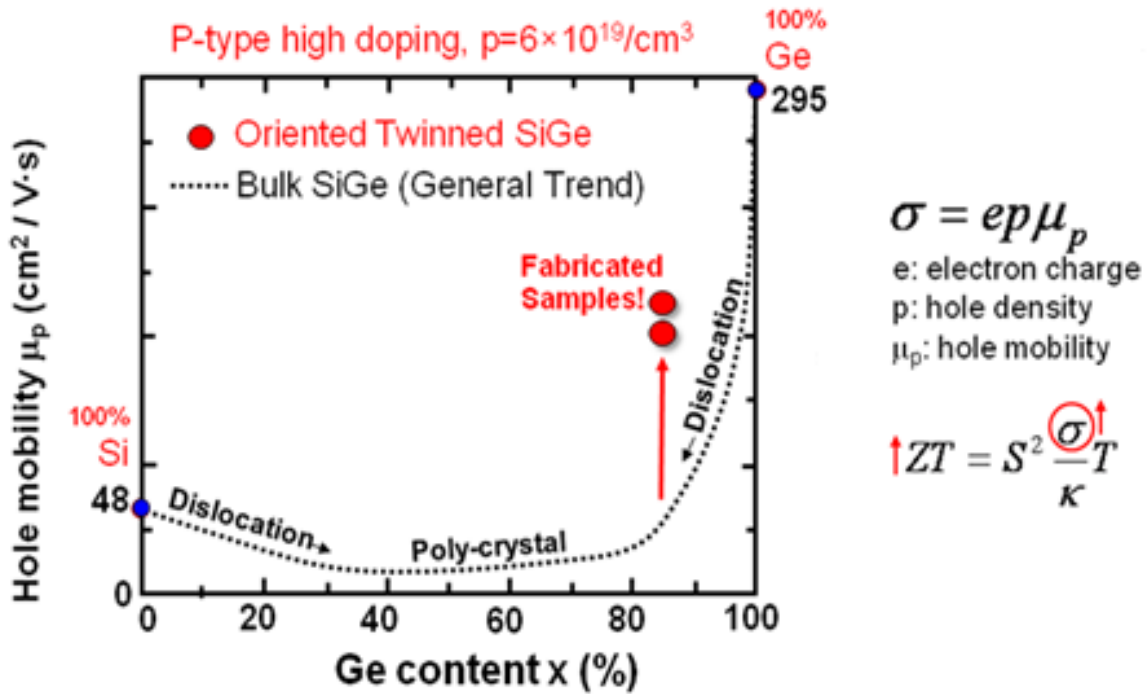


Figure 58. Electrical mobility of fabricated twinned $\text{Si}_{1-x}\text{Ge}_x$ samples with respect to bulk SiGe. An increase in the electrical conductivity leads to an increase in ZT (ref. 47 and 48).

SECTION 10

LOW TO MID-TEMPERATURE THERMOELECTRICS

The utilization efficiency of fossil fuels has virtually reached its limits (ref. 49). Therefore, the recovery of energy from waste heat using a TE conversion system is the only means of achieving further increases in energy use efficiency with fossil fuels. Figure 59 shows the current efficiency of various power generating systems and the improvement in efficiency assuming the additional use of a TE generating system with an efficiency of 20 percent (ref. 50).

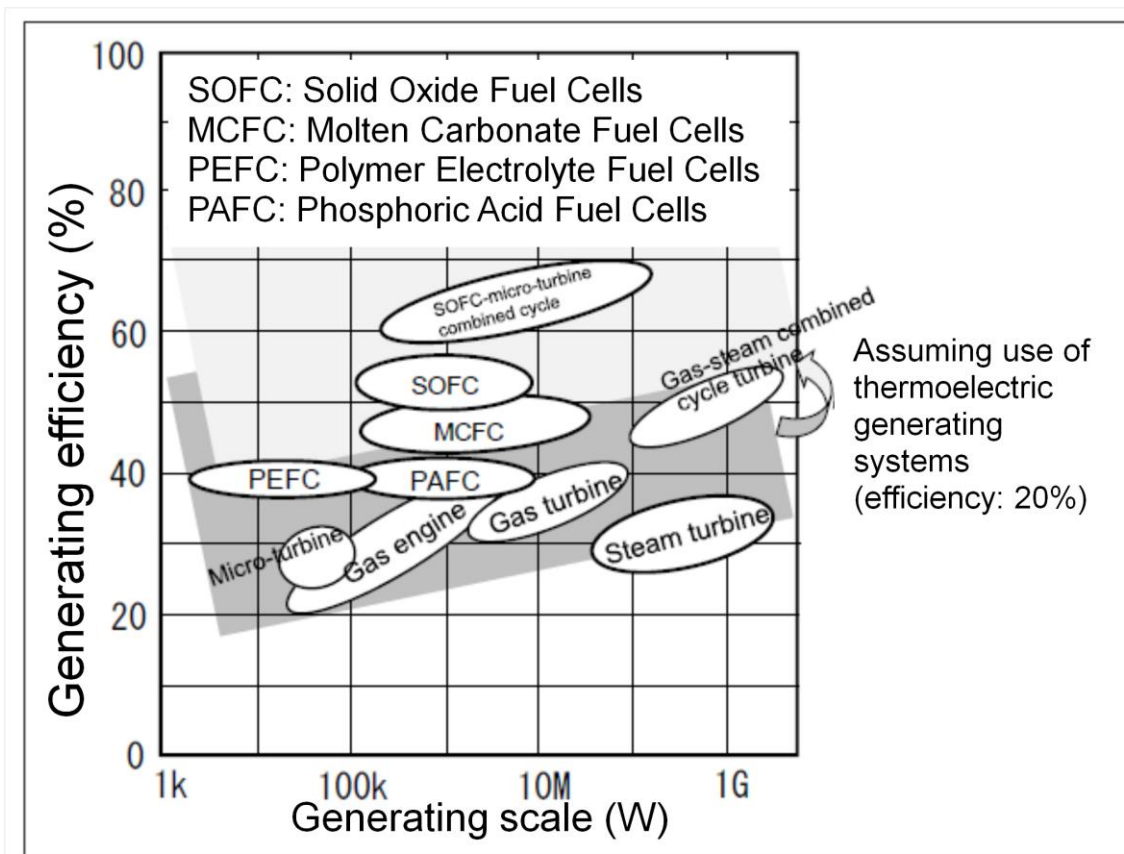


Figure 59. The efficiency of current power generating systems and their improvement of generating efficiency assuming the additional use of TE systems with 20 percent efficiency (ref. 49).

Generating efficiency from the combustion of fossil fuels as a heat source is 40–60 percent when a gas and steam turbine are used in combined cycle power generation. This means that up to 60 percent of the energy from the combustion of fossil fuels (equivalent to approximately 15 TW) is waste heat (Figure 60; ref. 51). In the case of automobiles with a reciprocating engine that uses fossil fuels, the energy consumed for power is on the order of 30 percent with up to 70 percent of the energy being wasted as heat. This does not mean that all of this waste heat is simply discharged into the atmosphere without use; part of this heat is used in maintenance and control of the power generating system and as a heat source for hot water, heating, etc. Nevertheless, the amount of thermal energy that is discarded without use is quite large. If this waste heat energy

can be recovered effectively then an increase in the total efficiency of these power generating systems can be expected.

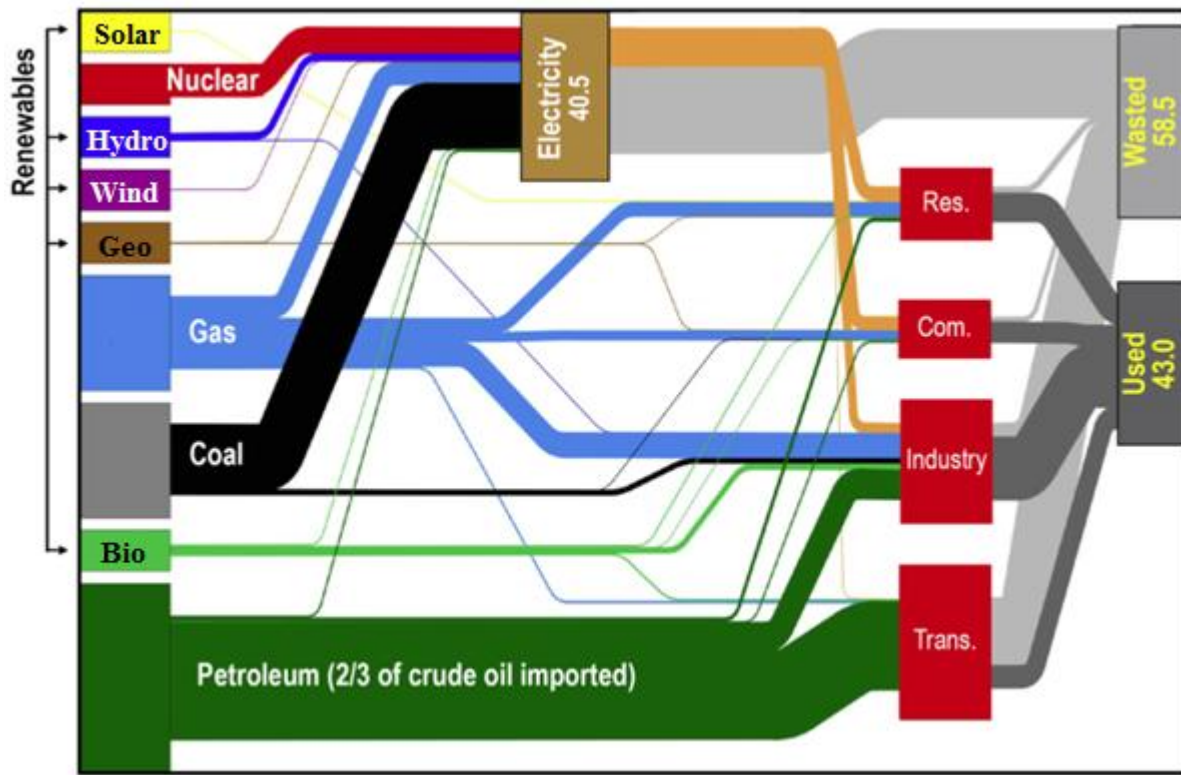


Figure 60. The Lawrence Livermore National Laboratory's finding during their 2008 study of energy use (ref. 51).

Development of TE materials that convert thermal energy to electrical energy with high efficiencies is being promoted as a technology for use in realistic applications. However, the efficiency results of TE materials and systems to date have not reached a level that can support a TE power generation market, including cost competitiveness, with other types of power generating systems.

TE power generating modules are comprised of two types of elements: a p-type semiconductor element that has more holes than electrons and an n-type semiconductor element that has more electrons than holes. The electrons in the high temperature region are activated when heating in the n-type semiconductor causes them to diffuse to the low temperature region. This generates a thermal electromotive force (EMF) and the high temperature side reaches a high electric potential. The case is reversed for the p-type semiconductor where the holes in the high temperature region are activated when heated. These holes migrate to the low temperature region generating a thermal EMF, and the low temperature side achieves a high electric potential. A current flow occurs between the n-type and p-type semiconductor elements when they are combined, thus allowing power generation. The power generating performance of TE conversion materials is expressed by the figure of merit (FoM) Z in the following equation: $Z = S^2 \sigma / \kappa$, where S is the Seebeck coefficient ($\mu\text{V/K}$), σ is the electrical conductivity ($\Omega \cdot \text{cm}$), and κ is the thermal conductivity ($\text{W/cm} \cdot \text{K}$). The dimensionless power generating performance index ZT is a

value obtained by multiplying Z by the absolute temperature T (K). High efficiency TE conversion materials, where ZT is large, are obtained when S and σ are large and κ is small.

The TE efficiency η_{TE} is given by equation (6):

$$\eta_{TE} = \eta_C \left(\frac{\sqrt{1+ZT}-1}{\sqrt{1+ZT}+\frac{T_C}{T_H}} \right) \quad (6)$$

where η_C is the Carnot efficiency, and T_H and T_C are the hot and cold temperatures, respectively. The power obtained from a TE device is dependent on its efficiency, which is determined by the heat flux from the high temperature heat source, the temperature differential during TE power generation, and the TE properties of the elements. The theoretical generating efficiency is around 20–30 percent for a TE material with $ZT \approx 2 - 3$.

Figure 61 shows the compromise between a large Seebeck coefficient and high electrical conductivity in TE materials that must be met to maximize the electrical power factor ($S^2\sigma$) and, hence, the FoM (ZT). This peak typically occurs at carrier concentrations between 10^{19} and 10^{20} carriers per cm^3 (depending on the material system), which falls in-between common metals and semiconductors (i.e., concentrations found in heavily doped semiconductors). In addition, the thermal conductivity must be decreased, but this is difficult because of the mutual dependence of the electrical and thermal conductivities (i.e., both increase in a similar fashion). Therefore, it has been extremely difficult within the past 50 years to increase the performance ($ZT > 1$) of materials suitable for practical applications, but recent efforts have been made to produce new TE material designs that leverage nanotechnology in order to enhance their TE performance.

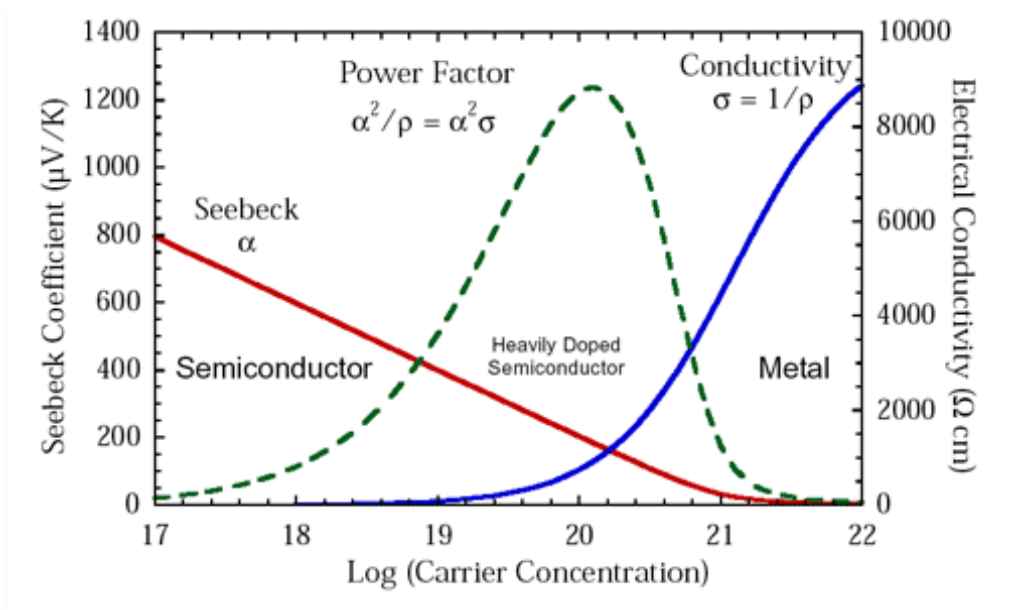


Figure 61. Optimizing ZT through carrier concentration tuning. Maximizing the efficiency (ZT) of a thermoelectric involves a compromise of increasing the Seebeck coefficient and electrical conductivity, while decreasing the thermal conductivity (ref. 52).

Figure 62 shows a graph of the current non-dimensional power generating performance index (ZT) values of low temperature (red), mid-temperature (orange), and high temperature (blue) TE conversion materials, including their expected values after five years of research. ZT of the respective materials tends to increase within their respective temperature range to a maximum value and then proceed to decrease with increased temperature. In the temperature region under 500 K, BiTe-based compounds display high ZT values with the power generating performance of Bi_2Te_3 peaking at $ZT \sim 1.2$. In the mid-temperature region of 500–900 K, AgTe-based compounds display high ZT values with $\text{AgSbTe}_2/\text{GeTe}$ having $ZT \sim 1.25$ and $\text{CeFe}_4\text{CoSb}_{12}$ having $ZT \sim 1.4$. In the high temperature range above 900 K, SiGe- and CoO-based materials show high ZT values, with $\text{Si}_{0.2}\text{Ge}_{0.8}$ displaying a $ZT \sim 0.8$.

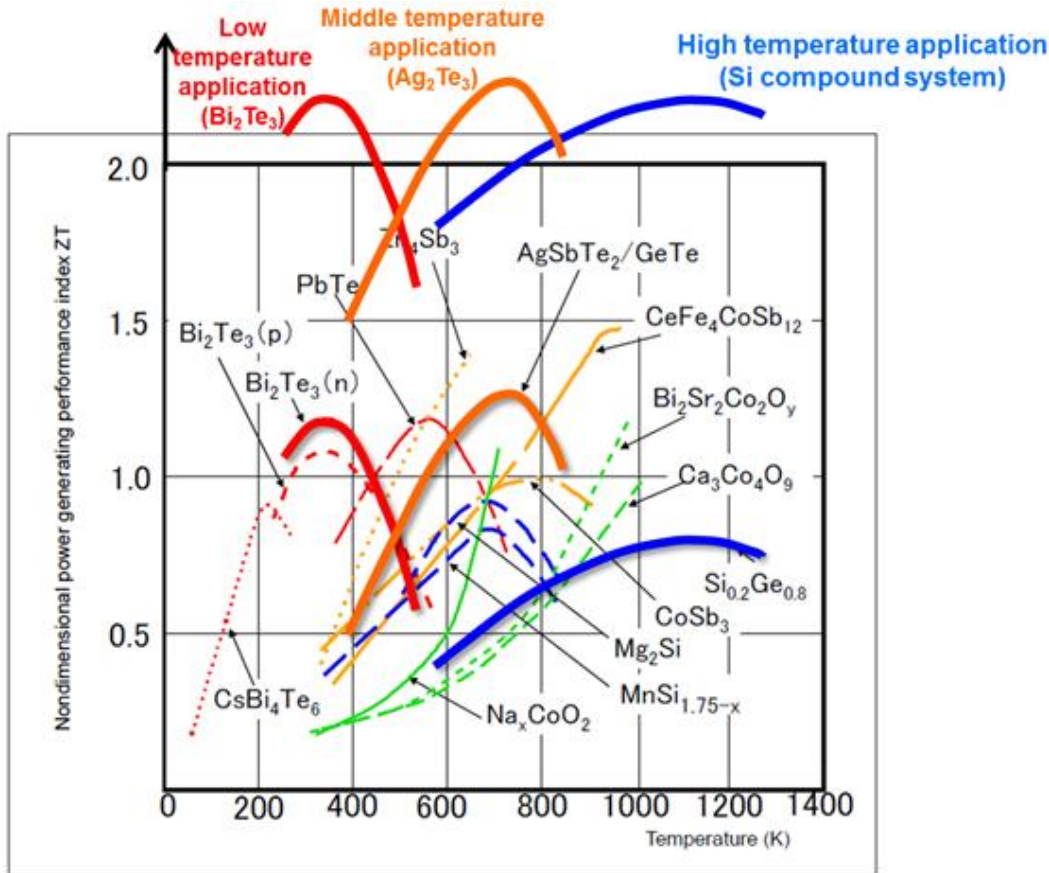


Figure 62. Current values and expected achievements after five years of the non-dimensional power generating performance index (ZT) of low temperature (red), mid-temperature (orange), and high temperature (blue) TE conversion materials (ref. 49).

The metallic nanoparticle decoration of grains of low to mid-temperature TE materials that already exhibit high ZT values has been explored to achieve a new type of material that pushes ZT even higher. Figure 63 illustrates this concept of an aggregated form of TE material in which each crystalline grain is surrounded by metallic nanoparticles. This morphological arrangement shows a significant performance improvement by reducing the thermal conductivity (κ) from one grain to another through the introduction of a separation gap greater than the phonon mean free

path (MFP). Thus, phonons scatter at such grain boundaries and remain within the morphological domain of the grain without conducting and contribute to a reduction of the thermal conductivity. Of course, these metallic bridges formed by the nanoparticles allow electrons to pass through, thus sustaining the level required for electrical conductivity (σ) but also allowing thermal transport by energetic electrons. However, much less than 30 percent of the total thermal energy is due to electron transport (the other 70 percent due to phonon transmission is now blocked) within the given low temperatures and morphological domain of grains.

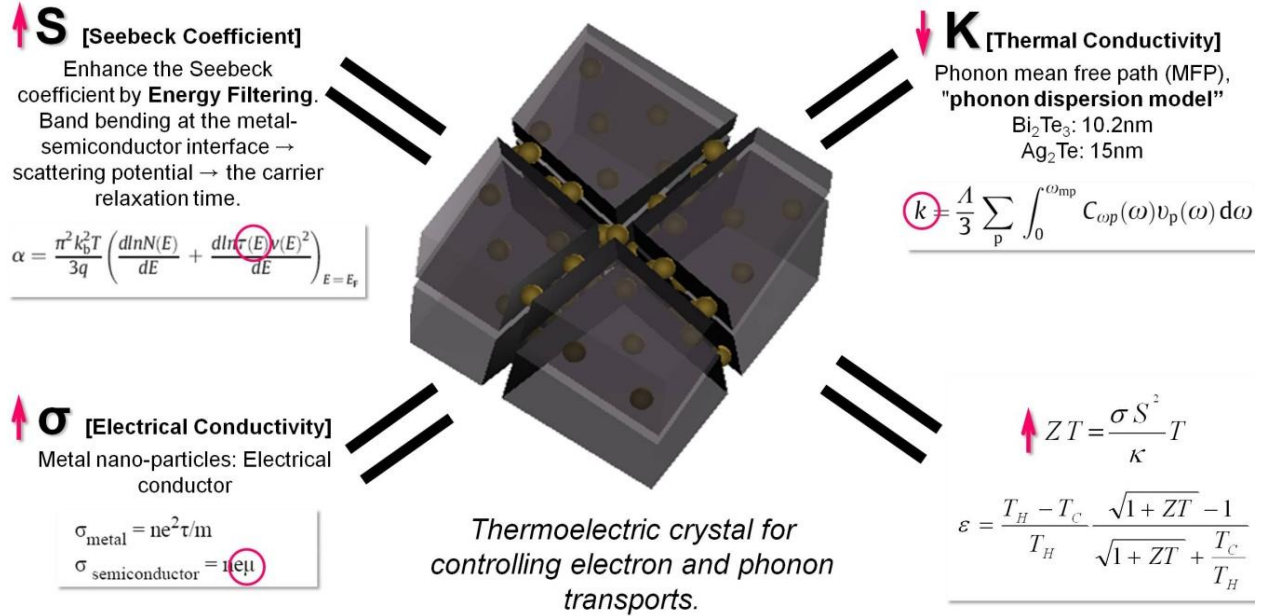


Figure 63. NASA developed TE material design by decorating grains with metallic nanoparticles in order to increase the Seebeck coefficient and electrical conductivity, while decreasing the thermal conductivity to increase the TE FoM.

The tailoring of these nanoparticle-decorated TE materials becomes critical because the overall FoM for these new TE materials can be determined by the nanostructure of a low-dimensional material. For example, the composition, size, and quantity of the nanoparticles, including the uniformity of their dispersion over the grain surfaces, are important factors that influence the reduction of the thermal conductivity (κ) through phonon scattering, while increasing the electrical conductivity (σ) through conduction pathways with possible engineering of the Seebeck coefficient (S).

A new method of preparing a range of micro- to nano-scale Bi₂Te₃ (for low temperature TEs) and Ag₂Te (for mid-temperature TEs) grains surrounded by metallic nanoparticles has been established through tailoring the nanostructure as discussed above and as shown in Figure 63. One of the key issues to developing these high FoM TE materials is to introduce metallic nanoparticles that are larger than the phonon MFP into bulk TE materials. The phonon MFPs of Bi₂Te₃ and Ag₂Te were calculated using both the Debye model (ref. 53) and phonon dispersion model (ref. 54). The calculated phonon MFPs of Bi₂Te₃ and Ag₂Te with the phonon dispersion model was found to be about 17 nm at room temperature. The phonon MFP obtained from the

Debye model was calculated to be much smaller than that of the dispersion model. Therefore, the size of the metallic nanoparticles was chosen to be larger than 17 nm (i.e., larger than the phonon MFP predicted by either model).

To maximize its TE performance, Bi_2Te_3 was first synthesized into a form of low-dimensional nanocrystals where good control over the size and shape of the nanoparticles is essential since phonon scattering depends on these parameters. Basically, nanometer-sized particles tend to aggregate because of a large surface-to-volume ratio and high surface energy. In the case of high energy ball milling, the particle size can be controlled by the milling speed and the diameters of the milling balls (Figure 64a). It is also possible to synthesize these powders with a chemical process in a simple beaker-system where the sizes and shapes of the synthesized particles can be precisely controlled. The solvothermal synthesis successfully produced dark grey powders of bismuth telluride nanocrystals after a separation procedure, which included filtering, washing, and drying (Figure 64b).

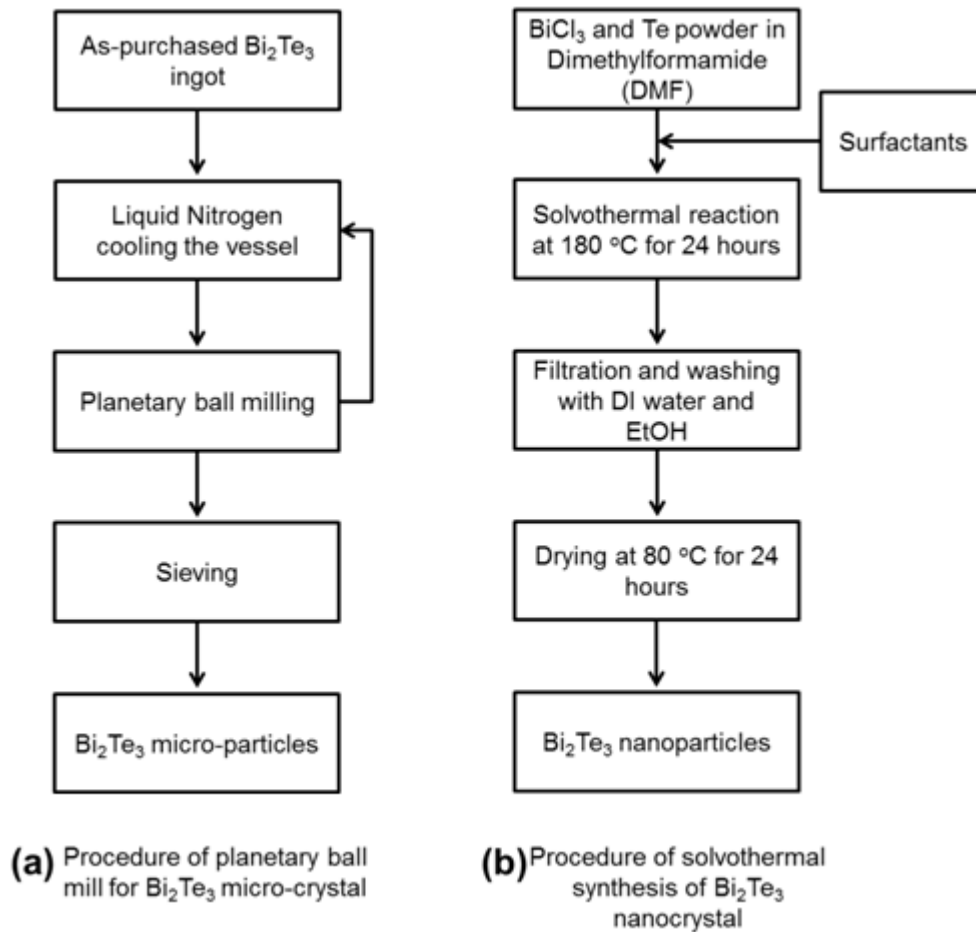


Figure 64. Two procedures for synthesizing Bi_2Te_3 crystals (ref. 55).

Figure 65a exhibits the x-ray diffraction (XRD) scans of bismuth telluride nanocrystals fabricated using potassium hydroxide (KOH) and ethylenediaminetetraacetic acid (EDTA). All peaks in the patterns correspond to the reflections of the rhombohedral phase $R\bar{3}m$ with lattice

constants $a = 4.28 \text{ \AA}$ and $c = 30.50 \text{ \AA}$, which are in agreement with the reported values $a = 4.3852 \text{ \AA}$ and $c = 30.4830 \text{ \AA}$ (JCPDS 15–0863) (ref. 56). No other diffraction peaks were detected such as Bi or Te crystalline phases. The nanoparticles have sheet shapes with a size distribution of fewer than 200 nm in the TEM bright-field image. The inset is the corresponding selected area electron diffraction (SAED) patterns of bismuth telluride. The SAED patterns (both indexing and intensity of patterns) are in agreement with the XRD results. The patterns do not show any additional diffraction spots or rings for any other phase (Figure 65b). The elemental analysis of bismuth telluride was measured by energy dispersive spectroscopy (EDS) analysis of field emission (FE) TEM (Figure 65c). The atomic ratios of Bi and Te are analyzed to be 39 and 61 percent, respectively. This reveals that the bismuth telluride nanocrystals are composed of the stoichiometric Bi_2Te_3 phase. The synthesized Bi_2Te_3 particles were used as a starting material for new TE crystal design including Bi_2Te_3 decorated with Au/Ag nanoparticles, Ag_2Te decorated with Bi nanoparticles, and Bi_2Te_3 ink.

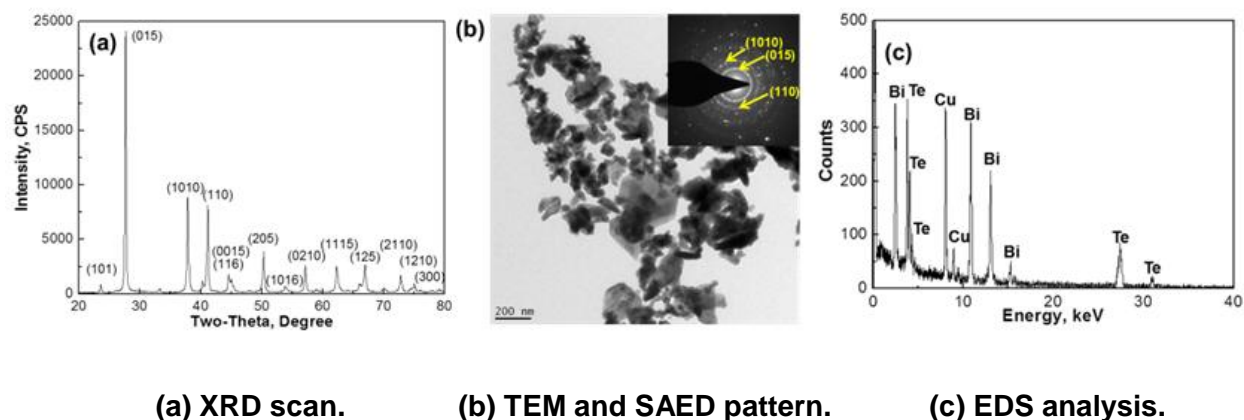
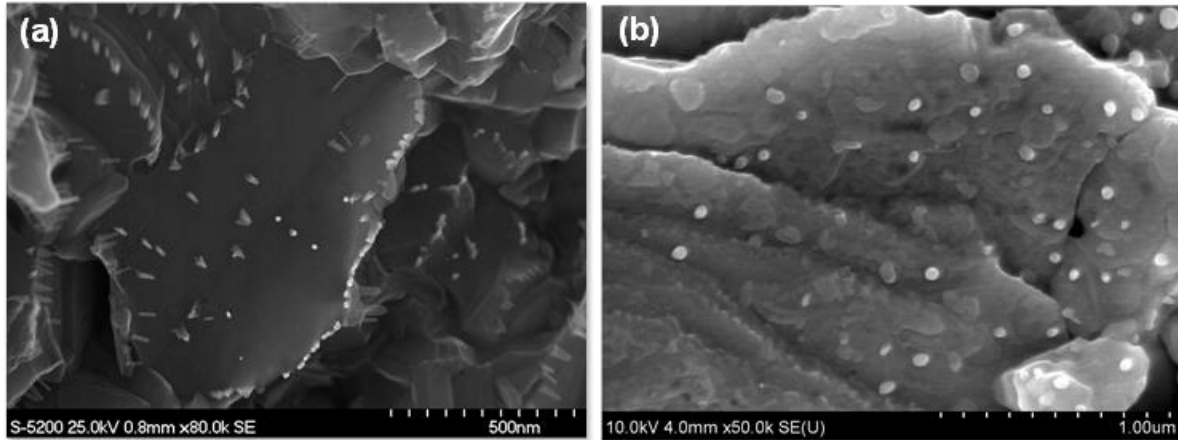


Figure 65. The solvothermally synthesized Bi_2Te_3 powders.

A cleavage surface of the Bi_2Te_3 grains coated with Au or Ag metallic nanoparticles was imaged using SEM; micrographs from which are shown in Figure 66. In these images, the metallic nanoparticles exhibit a uniform distribution on the Bi_2Te_3 grain surface. In Figure 66a, Au nanoparticles with a narrow size distribution in the 20–25 nm range are shown decorating Bi_2Te_3 grains. In Figure 66b, there are no aggregated Ag particles, and the sizes of Ag nanoparticles are fairly uniform with a range of 70–120 nm.



(a) 0.05 wt percent Au nanoparticles.

(b) 0.05 wt percent Ag nanoparticles.

Figure 66. Surface morphologies of the Bi_2Te_3 grains covered with nanoparticles.

Four samples were prepared in total. The amount of gold used to prepare the first, second, and third samples were 0, 0.001, and 0.05 percent of Bi_2Te_3 by weight, respectively. The amount of silver used to prepare the fourth sample was 0.05 percent of Bi_2Te_3 by weight.

The results show that the samples of the Bi_2Te_3 grains covered with 0.05 wt percent Au and 0.05 wt percent Ag metallic nanoparticles have lower thermal conductivity than the original Bi_2Te_3 (Figure 67d). Despite the decrease in the thermal conductivity, the electrical conductivity doubled with the 0.05 wt percent Au and Ag (Figure 67b). As the amount of Au and Ag increased, the power factor increased as well (Figure 67c), along with the FoM (Figure 67e). The Bi_2Te_3 decorated with 0.05 wt percent Au (blue triangle) and Ag (red triangle) particles demonstrated a higher FoM than that of the nanocomposite (NC) samples and zone-melted (ZM) sample (Figure 67f) taken from literature (ref. 57). The FoM of Au and Ag decorated Bi_2Te_3 samples are above unity, which is not only significantly higher than that of the NC or ZM samples, but also higher than SOA Bi_2Te_3 alloys. In general, the thermal conductivity and the electrical conductivity have a linear relationship, as indicated with the Wiedemann-Frantz law (ref. 58). However, the authors have developed and demonstrated a new material design to improve TE properties by using Au or Ag nanoparticle bridges that connect Bi_2Te_3 grains.

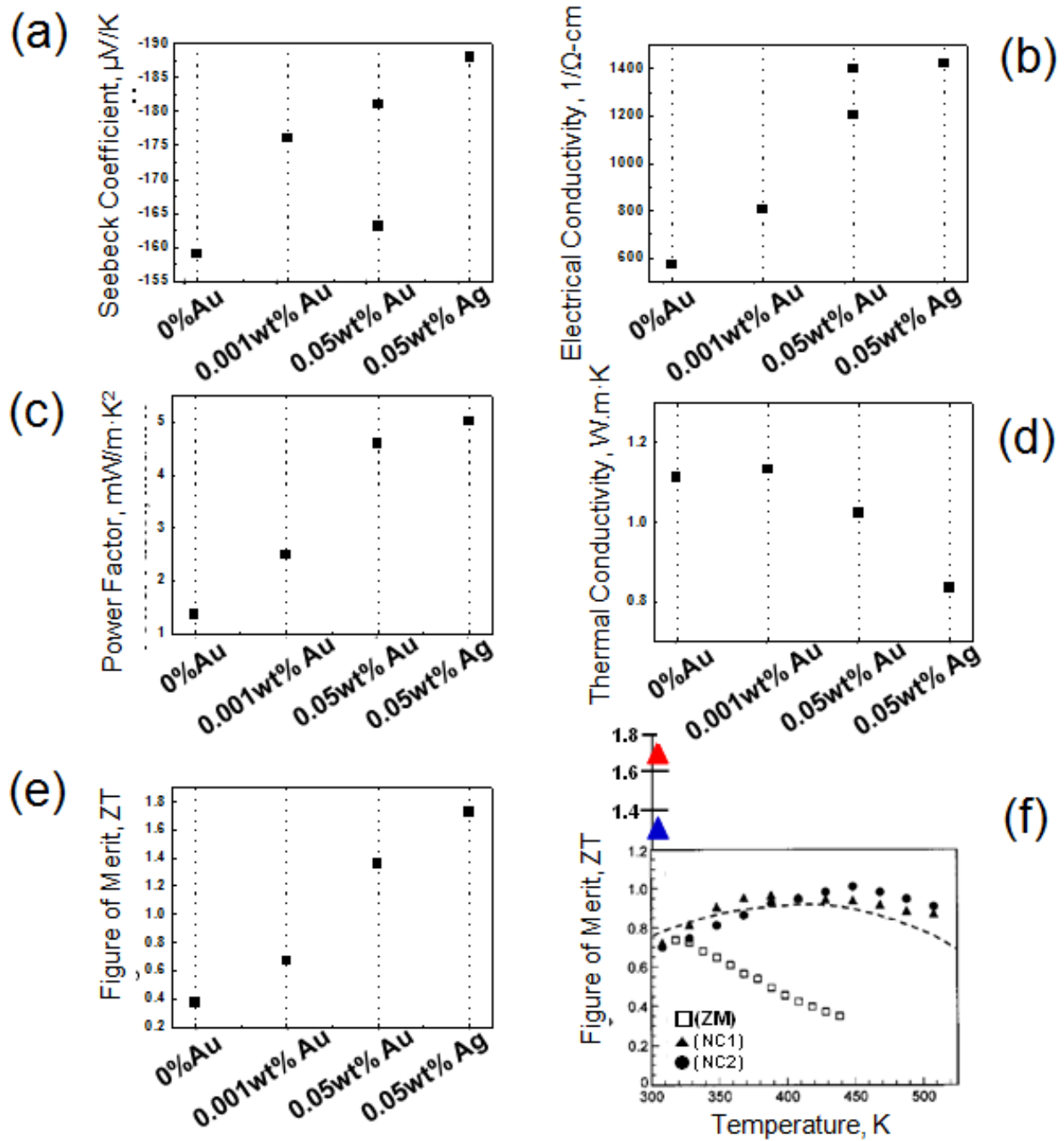
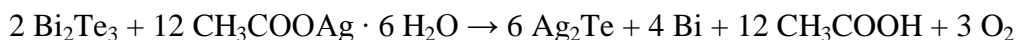


Figure 67. (a) The Seebeck coefficient, (b) the electrical conductivity, (c) the power factor, (d) the thermal conductivity, and (e) the dimensionless FoM of Bi_2Te_3 samples decorated with 0.001 wt percent / 0.05 wt percent Au or 0.05 wt percent Ag metallic nanoparticles using Bi_2Te_3 as the starting material at room temperature. (f) The dimensionless FoM of nanocomposite samples (NC1, NC2) and zone-melted (ZM) sample (ref. 57) compared with data measured for Bi_2Te_3 samples decorated with Au and Ag nanoparticles (blue and red triangles, respectively).

The authors have developed a simple method to create micro-sized silver telluride grain powders surrounded by bismuth-rich metallic nanoparticles. A thermal process for alloy formation of Ag_2Te was used with a mixture of bismuth telluride powders (Bi_2Te_3) and silver acetate (CH_3COOAg) powders. The chemical process during thermal loading for alloy formation can be described by



The mixture of two powders contains enough water molecules whose hydrogen replaces the silver in silver acetate. The silver atoms replaced by the hydrogen atoms form silver telluride molecules by tossing out bismuth atoms from Bi_2Te_3 . These tossed-out bismuth atoms aggregate together to form nano-sized particles, while the acetic acid and oxygen are vaporized away at the reaction temperature. This was an unknown process and a new discovery that during development of the bismuth nanoparticles, they position and anchor themselves over the surface of the micro-sized silver telluride grains as shown in Figure 68 (ref. 59).

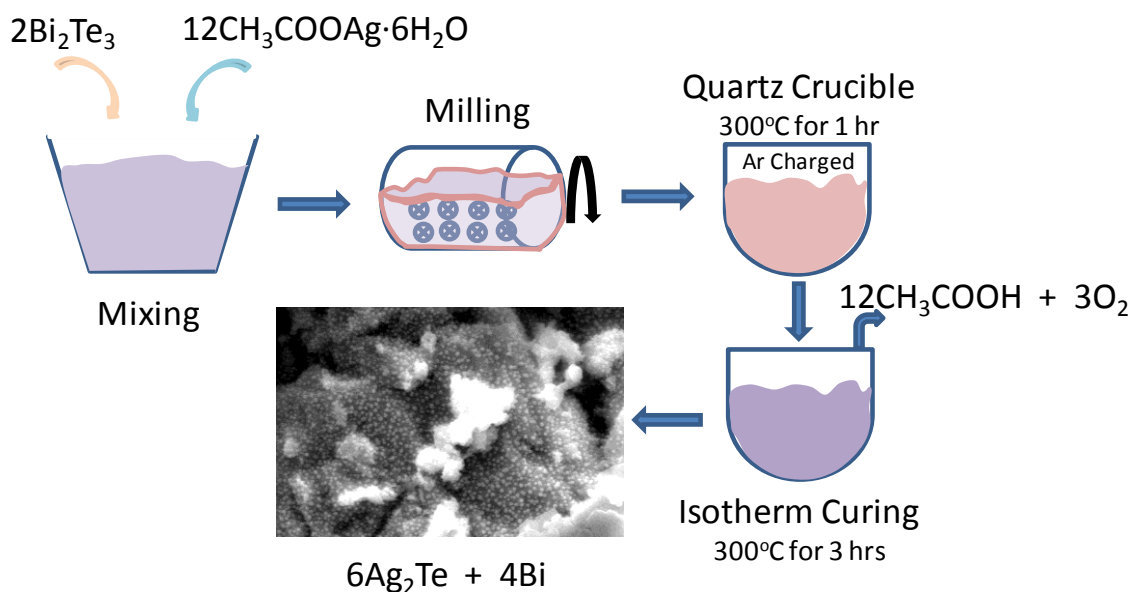


Figure 68. Synthetic process of Ag_2Te grains whose surfaces are covered with metallic bismuth nanoparticles.

A SEM image of the cleavage surface of a Ag_2Te grain coated with bismuth metallic nanoparticles is shown in Figure 69a. As shown in this SEM image, the Bi metallic nanoparticles are uniformly distributed on the Ag_2Te grain surface. The sizes of Bi nanoparticles are fairly uniform (sizes range between 50–100 nm). High resolution compositional maps of the sample were obtained from the backscattered electron (BSE) image to distinguish different phases (Figure 69b). Nanoparticles have brighter BSE intensities than other areas. A "brighter" BSE intensity correlates with a greater average proton number Z (Bi rich) in the sample, and "dark" areas have a lower average Z . This result confirmed the atomic number contrast (Z -contrast) imaging using a high-angle annular dark field (HAADF) detector (Figure 69c). A quantitative analysis of the nanoparticles from the EDS confirmed a stoichiometry ratio of Bi to Te of 9:1 (Bi-rich phase) (Figure 69d). The high resolution transmission electron microscope (HRTEM)

image of a nanoparticle (Figure 69e) demonstrates that it has the face centered cubic (fcc) structure (the zone axis of the fast Fourier transform (FFT) image is [011]) and is single crystalline. The TEM bright field (BF) image (Figure 69f) shows that Ag_2Te grain powders are coated with bismuth-rich metallic nanoparticles, which are positioned as bridges between thermoelectric Ag_2Te grains.

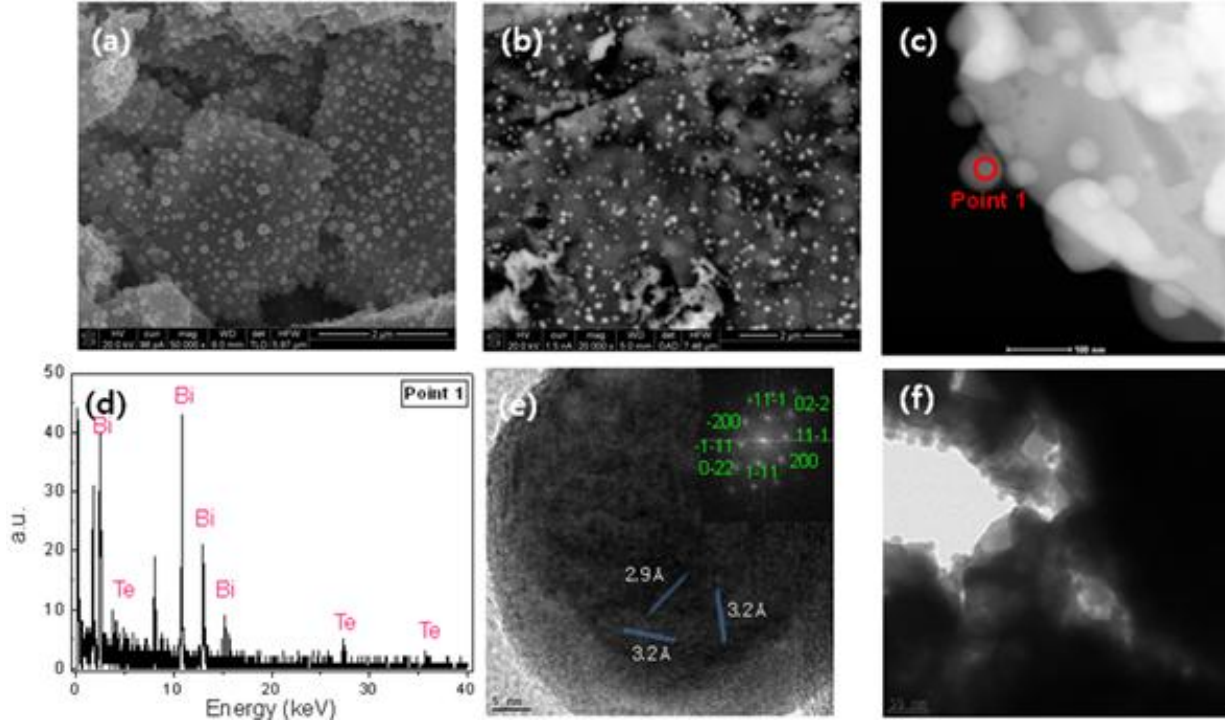


Figure 69. (a) A cleavage surface SEM image of the Ag_2Te grain covered by bismuth metallic nanoparticles, (b) BSE image, (c) HAADF STEM image (red circle: EDS point analysis area), (d) EDS spectra of nanoparticle (red circle area in c), (e) HRTEM image of nanoparticles, and (f) BF TEM image of the Ag_2Te grain covered by bismuth metallic nanoparticles.

It has been known that Ag_2Te has a characteristic metal-to-semiconductor transition around 400 K, as shown in Figure 70b (ref. 60). The author's sample shows the same phase transition around 400 K (Figure 70a).

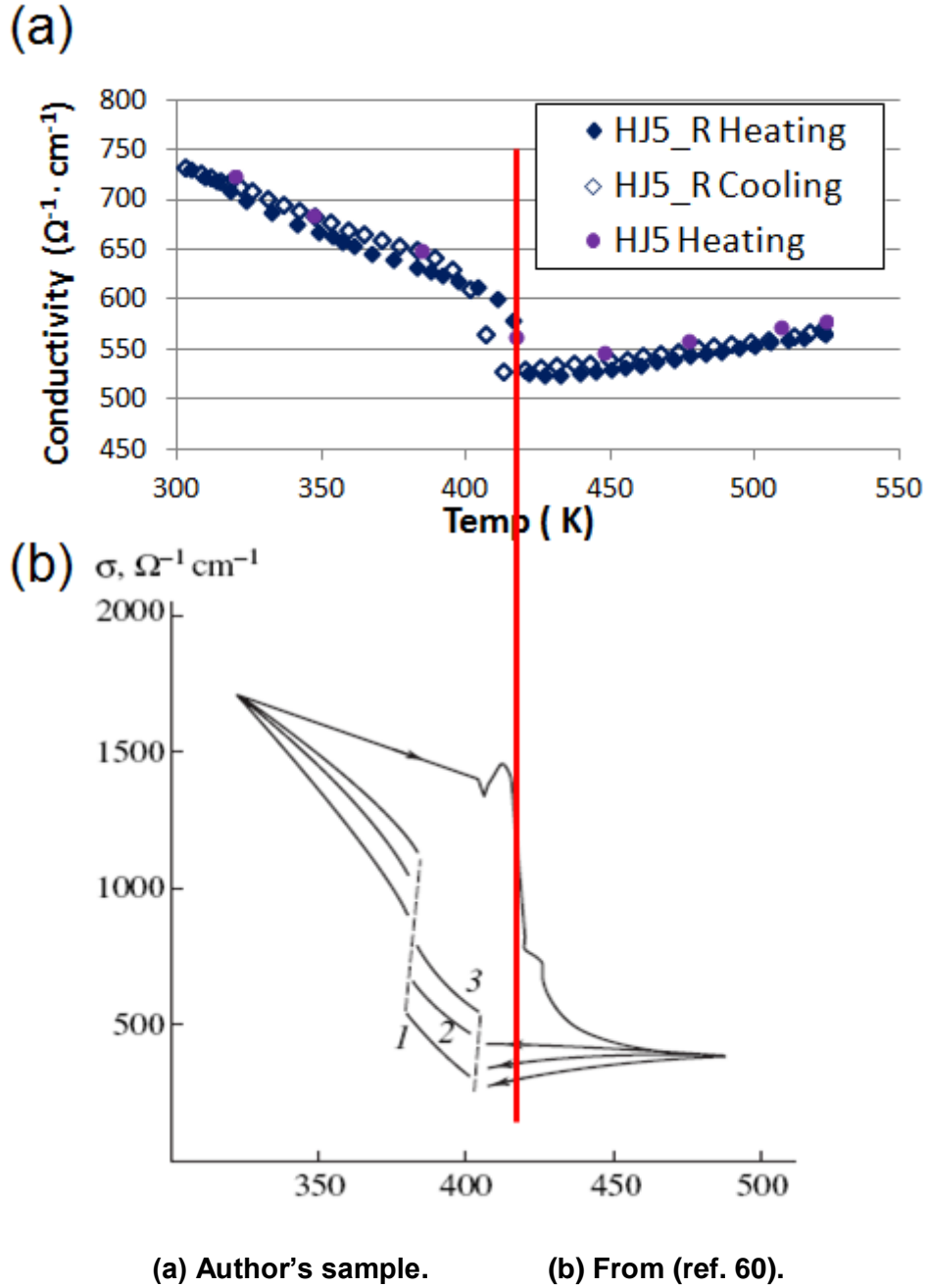
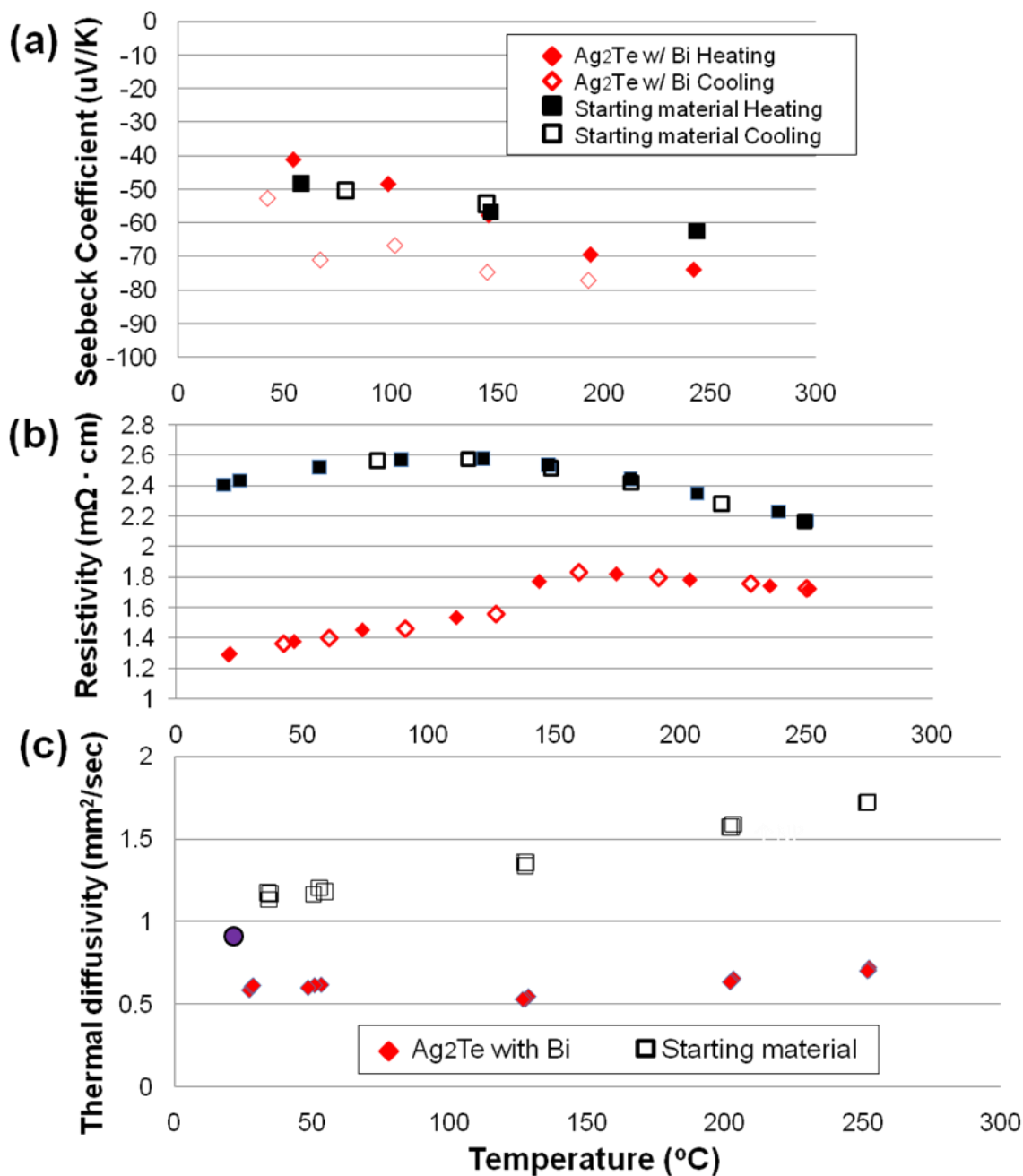


Figure 70. Temperature dependencies of electrical conductivity (σ).

In general, it is difficult to increase ZT because of the competing effects of the electrical and thermal conductivities. Here, the authors have developed a materials processing technique to create Ag_2Te powders coated with bismuth-rich metallic nanoparticles, and it has shown improved thermoelectric properties. Figure 71 shows (a) the Seebeck coefficient, (b) the electrical resistivity, and (c) the thermal diffusivity of the samples.



(a) Seebeck coefficient. (b) Electrical resistivity. (c) Thermal diffusivity.

Figure 71. Temperature dependencies of various TE parameters for a Ag_2Te sample decorated with Bi-rich metallic nanoparticles. The purple data indicated at room temperature is cited from Borca-Tasciuc et al. (ref. 61).

The Seebeck coefficient of Ag_2Te grains covered with Bi metallic nanoparticles was increased compared to that of Bi_2Te_3 (starting material) (Figure 71a). The thermal diffusivity was linearly related with the thermal conductivity. The test results showed that the sample of Ag_2Te grains covered with Bi-rich metallic nanoparticles had less than half of the thermal diffusivity of Bi_2Te_3 (Figure 71c). Further, despite the decrease in the thermal diffusivity, the electrical conductivity

doubled (i.e., electrical resistivity decreased by half) near room temperature (Figure 71b). These results suggest that the Bi metallic nanoparticles dangling on the Ag_2Te grain surface would play a major role in reducing the thermal conductivity by promoting phonon scattering while enhancing electron conduction.

The novel nanoparticle decorated TE materials discussed previously (Bi_2Te_3 and Ag_2Te) are not well suited to high speed and low cost assembly operations. This is because they are manufactured by dicing, extrusion, or sintering processes that are time consuming.

However, when the element thickness is less than 500 μm , it is very difficult to apply an automated manufacturing system, most notably with a low production yield. Meanwhile, current TE module technology requires that the substrates be thick enough to withstand cracking, and thicker substrates result in heavier TE modules and higher materials costs. In addition, the use of silicon or ceramic substrates limits the size and shape of TE module. Printing technology is expected to improve the limitations of the current TE manufacturing process because it enables high speed fabrication, direct patterning, low material consumption, low temperature process, and printing on flexible and rigid substrate with drastically increased throughput. The printed devices can be produced by the common printing equipment, such as screen, flexography, offset lithography, ink-jet, and gravure.

The ink is composed of filler, binder, solvent, and additives. Printing inks are fluid inks with very low viscosity that allow them to be drawn into engraved cells in the cylinder then transferred onto the substrate. In order to quick dry the ink and maintain the viscosity, organic solvent or water is used. For the manufacturing of flexible printable electronics, many types of substrates, such as polyethylene (PE), polypropylene (PP), polyethylene terephthalate (PET), cellulose, etc., can be printed in the gravure printing system. The resolution of the print is highly dependent on the quality of the patterns on the roll and the surface and shape properties of the non-patterned areas. The engraving patterns can be created with various methods such as knurling, electrical discharge texturing, shot blasting, film masking, and laser engraving or roll surfaces.

Polystyrene, polyaniline, and epoxy resin were used as a binder in order to obtain TE ink. Epoxy resin was prepared with bisphenol f diglycidyl ether, a hardener, and a catalyst. Its viscosity was controlled by diluents. The polystyrene was prepared by the solution polymerization method with styrene, toluene, and 2,2-azobis (isobutyronitrile). Molecular weight and conversion of polystyrene were controlled by varying the amount of the initiator and the monomer and the reaction temperature. As a result, white colored polystyrene powders were obtained with 150,000 (g/mol) number averages of molecular weight and 92 percent final conversion. Viscosity of purified polystyrene powder was controlled with toluene. The synthesized Bi_2Te_3 powder was added to the epoxy resin, polyaniline, and polystyrene to make three kinds of printable slurries. The slurry was mixed by an ultrasonicator for 1 hour. The TE slurries were then printed on a glass substrate to form 100–200 μm thick films and cured to form solid thick films (Figure 72). Figure 73 shows photographs and SEM images of the Bi_2Te_3 / epoxy resin, Bi_2Te_3 / polystyrene, Bi_2Te_3 / PMMA, and Bi_2Te_3 / polyaniline films. It was confirmed that the samples have a grey collar, and Bi_2Te_3 particles were well dispersed in the binder. Conductivities were affected by annealing time and Bi_2Te_3 contents. To improve the electrical conductivity of the TE inks, carbon nanotubes (CNT) and graphite were added to the samples.

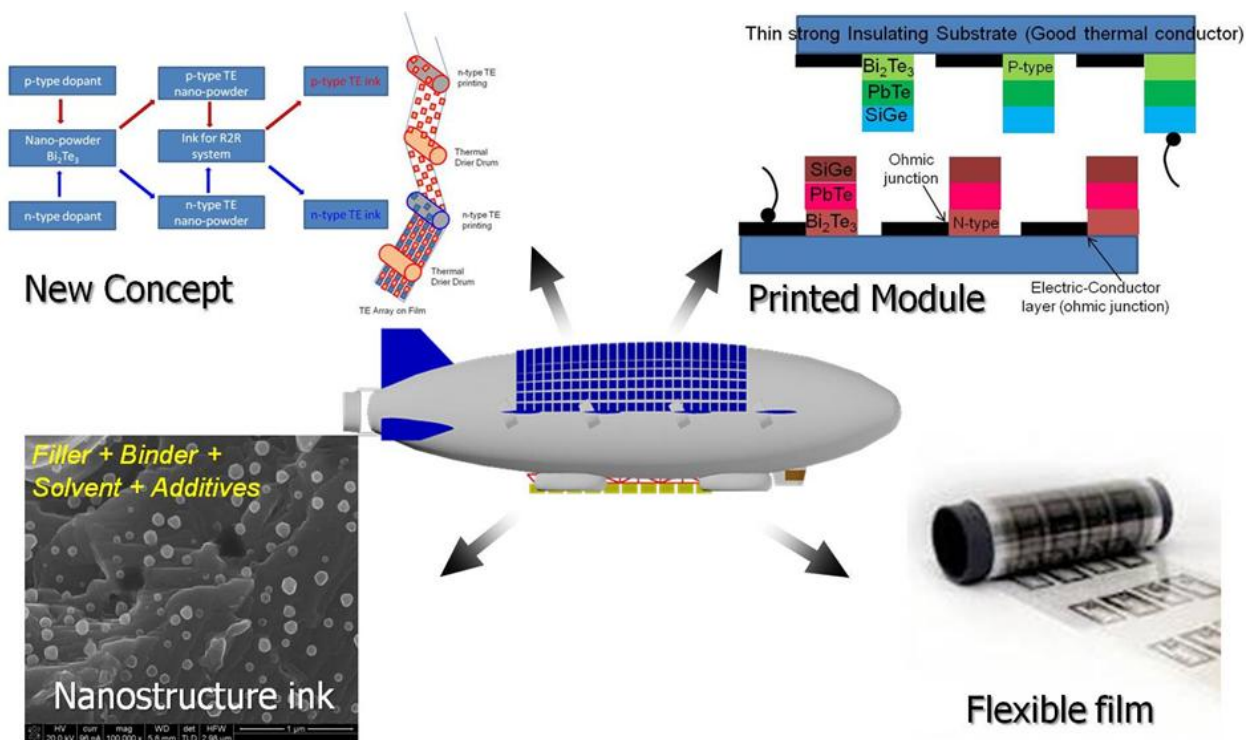


Figure 72. Concept for TE ink for airship application.

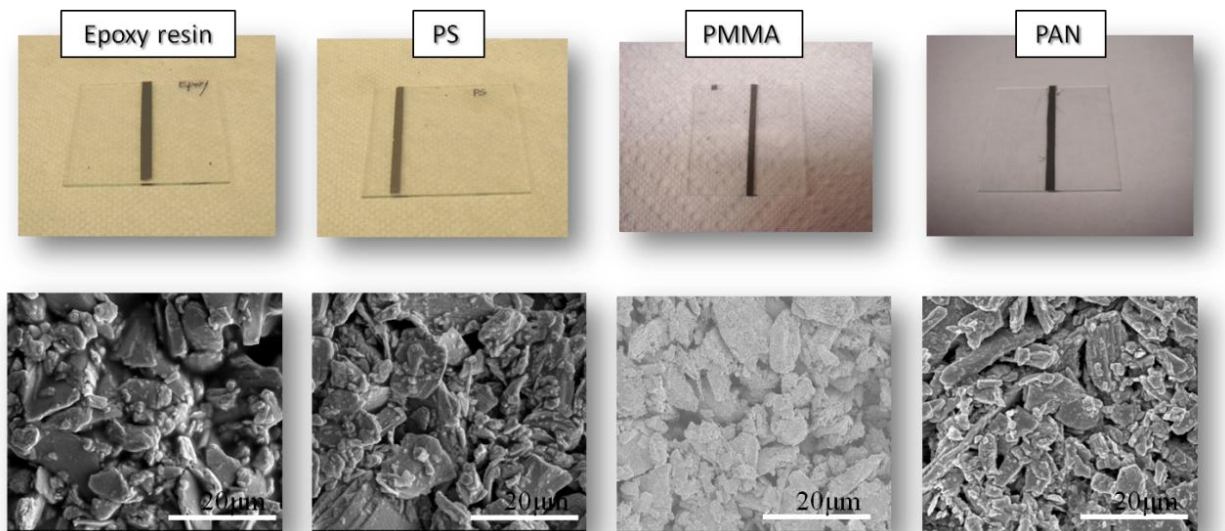


Figure 73. SEM images and photos for Bi_2Te_3 / epoxy resin, Bi_2Te_3 / polystyrene (PS), Bi_2Te_3 / PMMA, and Bi_2Te_3 / polyaniline (PAN) composites.

Figure 74 shows the measured material properties of the n-type Bi_2Te_3 /polyaniline, Bi_2Te_3 /polystyrene, Bi_2Te_3 /1% CNT, Bi_2Te_3 /2%, Bi_2Te_3 /1% graphite, and Bi_2Te_3 /2% graphite composites at 300 K. The epoxy composite materials appear to have relatively close Seebeck coefficients compared to the bulk materials. However, the electrical conductivities of the composites are two orders of magnitude less than that of bulk. This is likely due to the electrically insulating properties of the polymer and the contact resistance due to the fine particles. This presents trade-offs in the composite materials properties, and, as a result, both the

power factors and figure of merit (Z) values of the composites are at least one to two orders of magnitude less than that of bulk materials. The current limiting factor in the performance of the composite materials is the low electrical conductivity. The CNT and graphite were added to improve the electrical properties through composite optimization and additives.

These innovative methods of creating Bi_2Te_3 and Ag_2Te grains decorated with metallic nanoparticles significantly increase the TE efficiency compared to existing values. Further advanced TE materials research at NASA LaRC will hopefully reach a level that is able to support a TE power generation market.

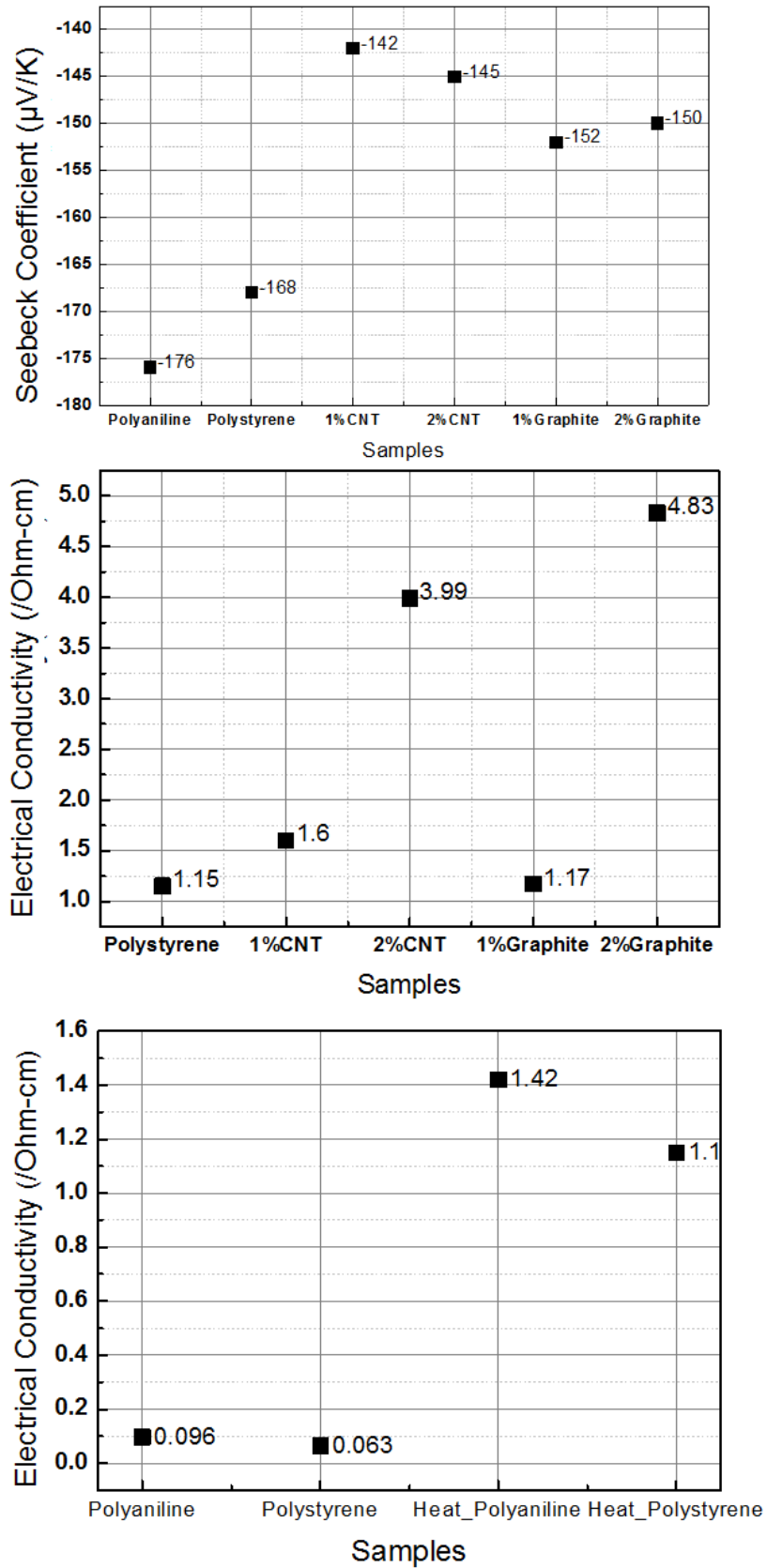


Figure 74. Material properties of printed TE composites at 300 K (ref. 62).

SECTION 11 THERMOELECTRIC DEVICE APPLICATIONS

These new TE materials (e.g., SiGe, Ag_2Te , Bi_2Te_3) that are being developed at NASA LaRC will be critical in producing viable commercial technologies with pronounced efficiencies. The goal is to attain a FoM (ZT factor) of 2.5 for these TE material concepts, which will require at least five years of further R&D efforts. Additional refinement of the TE devices that use these materials is possible by combining one TE material to another in a tandem mode (Figure 75 and Figure 76), thus compounding the recovery of waste energy.

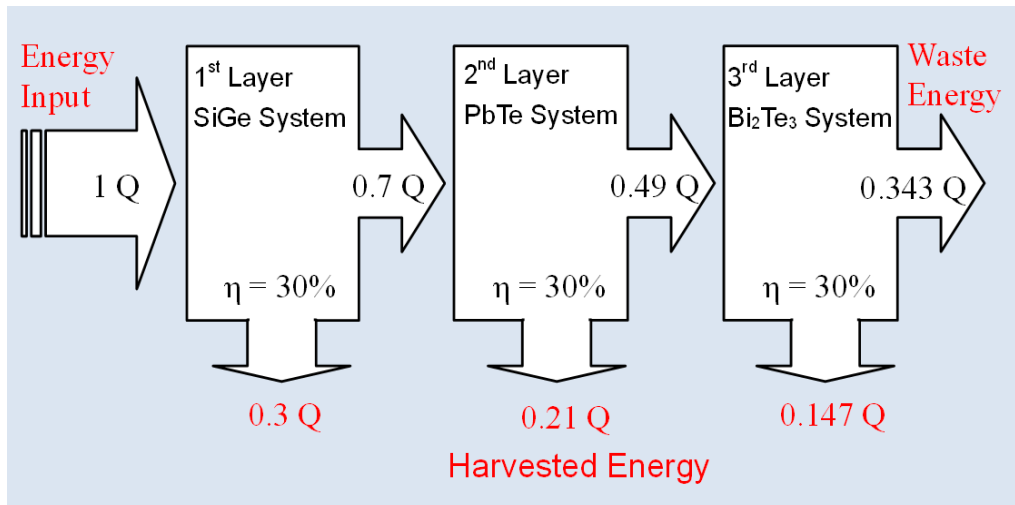


Figure 75. TE tandem system block diagram showing the potential energy savings assuming a 30 percent conversion efficiency of waste heat at each TE layer.

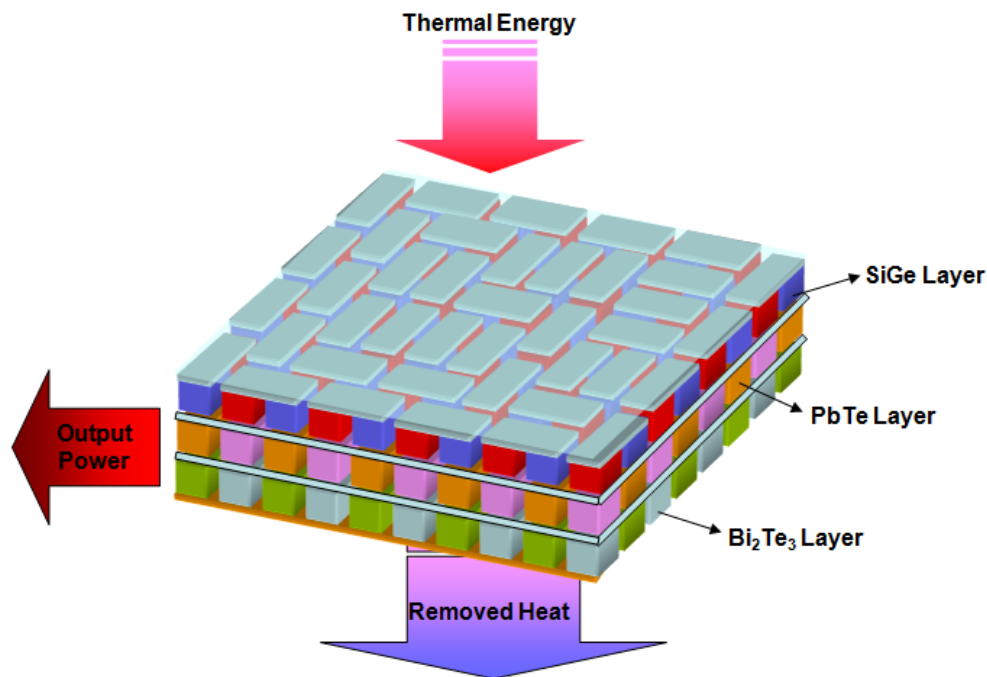


Figure 76. 3-D conceptual view of an advanced TE device in a tandem arrangement.

Figure 75 shows a block diagram of the energy that a TE tandem system could harvest if each TE material layer has 30 percent efficiency. The first TE layer converts a portion (0.3 Q) of the incident waste energy from a process (1 Q) at a high temperature, and the unconverted portion of energy (0.7 Q) goes into the next layer. This second layer converts this waste energy (0.7 Q) from the first layer at a mid-temperature range into usable energy (0.21 Q). The unrecovered portion (0.49 Q) of energy goes into the next layer at a lower operating temperature, and the process repeats itself. Thus, each of the layers is optimized for the temperature range of the application, establishing a regenerative cycle that maximizes the total (cascaded) conversion efficiency of the TE system. In this example, the TE tandem system would be 65 percent efficient.

Figure 76 shows a conceptual 3-D view of a three layer TE tandem system. Thermal energy, which is incident on the first layer, is converted into electrical power, and the waste heat from the first layer is passed to the second layer for conversion. This process is repeated as discussed before, where the performance of the tandem TE system is greatly influenced by the FoM of each material layer. Estimations of the TE regenerative cycle efficiencies are tabulated in Table 8 for various ZT factors and corresponding efficiencies, assuming that $T_C/T_H \sim 0.4\text{--}0.6$. The cascaded efficiency of a three layer TE tandem system can be very high, reaching 27 percent for a TE FoM ≥ 1.5 and further increasing far beyond the efficiency level of any conventional energy conversion system as the FoM increases to 3.5, 4.5, and beyond.

Table 8. Estimations of the TE regenerative cycle efficiencies for a three layer tandem system.

TE Tandem System	TE FoM ≥ 1.5 $\eta = 10\%$		TE FoM ≥ 3.5 $\eta = 20\%$		TE FoM ≥ 4.5 $\eta = 30\%$		Solar Cells
	Loaded Energy, Q	η	Loaded Energy, Q	η	Loaded Energy, Q	η	η
1 st Layer (HiT)	1Q in	10%	1Q in	20%	1Q in	30%	30% (?) for membrane PV
	0.9Q out		0.8Q out		0.7Q out		
2 nd Layer (Med T)	0.9Q in	10%	0.8Q in	20%	0.7Q in	30%	
	0.81Q out		0.64Q out		0.49Q out		
3 rd Layer (Low T)	0.81Q in	10%	0.64Q in	20%	0.49Q in	30%	
	0.729Q out		0.512Q out		0.343Q out		
Cascade Efficiency	0.271Q Harvested	27%	0.488Q Harvested	48%	0.657Q Harvested	65%	

Figure 77 shows the possible economic impact assessment of this TE device technology. The economic benefits may amount to several hundred billion dollars if the R&D efforts to increase the ZT factor hold. These benefits are due to a paradigm shift of energy technologies where advanced TE technology will replace steam cycle (i.e., Rankin cycle) technology, such as the steam turbine and powertrain of the conventional automotive cycle (i.e., Otto cycle). Therefore, the development of advanced TE materials is well-justified for continuous R&D with reasonable amounts of investment.

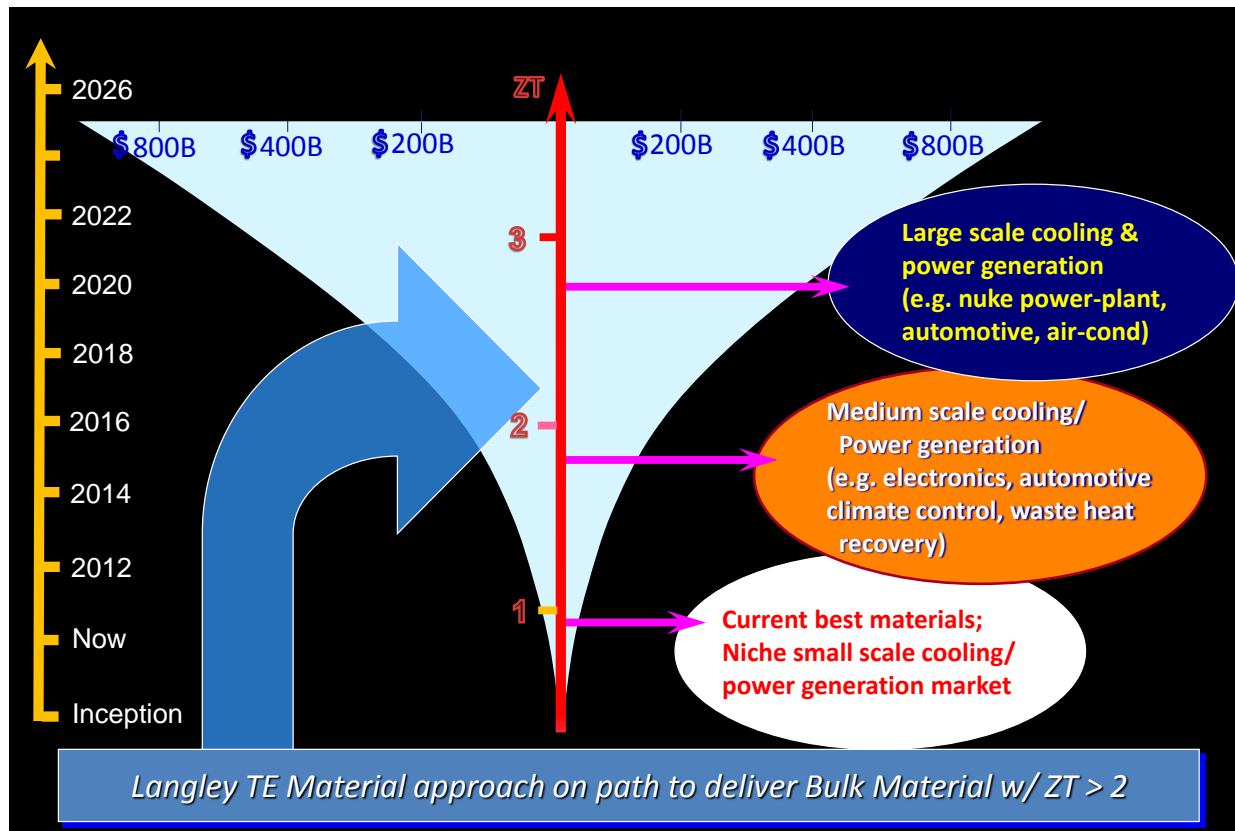


Figure 77. Possible economic impacts of more efficient TE device technology.

These tandem TE devices can be used in many existing power applications to recover waste heat energy. One primary example is the case of the internal combustion engine. Recent rises in fuel costs, along with environmental issues, have driven the auto industry to develop more fuel efficient automobiles. The proposed new concept cars are based on recouping wasted thermal energy into useful electrical energy. This wasted energy, which amounts to roughly 66 percent of the fossil fuel energy going into the engine, has typically been neglected in the past. The main reason for negligence has been due largely to the inexpensive fuel cost, but also partially to the lack of technology that converts thermal energy into useful (electrical) energy.

Most hybrid systems currently use a combination of an internal combustion engine, electric motor, and battery to increase the fuel efficiency of automobiles. The battery system for these electric or hybrid cars remains heavy, complex, and expensive. TE tandem systems, as discussed earlier, could be attached around the engine block and exhaust manifolds to recover the wasted thermal energy (~66 percent) generated by the fossil fuel combustion process. Recouping such losses is most desirable, not only for fuel efficiency reasons but also for increasing the overall powertrain performance.

A regenerative cycle for automobile powertrain applications to recover and deliver the converted wasted heat energy is shown in Figure 78. A high performance tandem TE device as shown in Figure 75 and Figure 76 is used to convert the wasteful thermal energy into electrical energy by integrating them around the engine block and exhaust manifolds. The efficiency of the TE devices is considered to be 27 percent by using a tandem system with a FoM ≥ 1.5 as shown in

Table 8. A sub-compact automobile engine with 150 horsepower (hp) will consume a total of 441 hp (i.e., 150 hp divided by 0.34). 441 hp is equivalent to 329,000 watts, of which 217,000 watts (~66 percent) is wasted as heat. Twenty-seven percent (the thermal efficiency of the tandem TE device) of this waste heat could be collected and converted to electrical power, which amounts to 58,600 watts (or 78.6 hp). This converted power from the wasted heat becomes just over one-half of the automobile driving power, which increases the total power system efficiency by 18 percent. This additional 79 hp obtained from the waste heat is a substantial improvement for the powertrain.

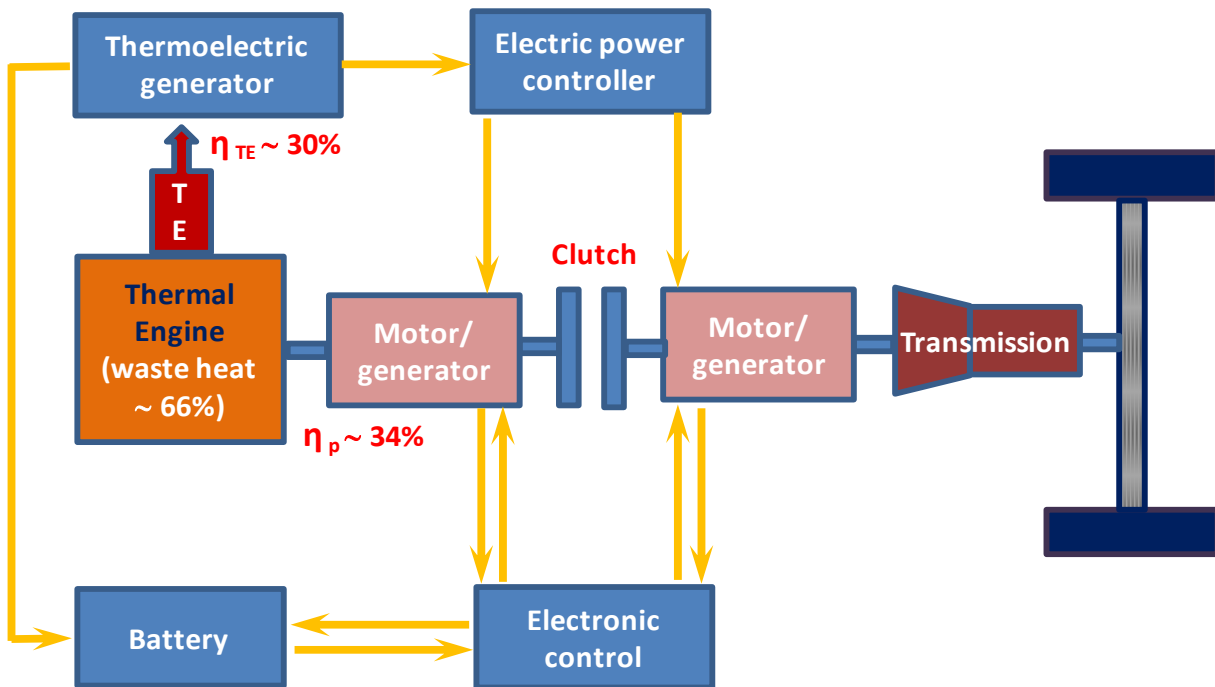


Figure 78. A new concept powertrain that recoups and converts wasted thermal energy into useful electrical energy.

This additional 79 hp is converted to DC electrical power and either stored in a battery for later use or run to the front and rear electric motors in the powertrain, which is distributed by an electric power controller unit. The thermal engine operates to generate a driving power and, at the same time, to generate electric power to store in the battery. Any excessive power from the engine is used to run the motor/generator unit to generate DC power. The clutch engages only when driving power is needed directly from the engine. Otherwise, the motor/generator, which is neighboring to the transmission, runs the driving while the clutch is disengaged. This driving mode is sustained by the DC power from the battery and the DC power from the motor/generator, which runs in a generator mode.

SECTION 12 SUMMARY

The feasibility of a new transportation system, the cargo airship, and the research and development of new green energy sources to power it were discussed within this NASA Technical Memorandum. These cargo airships offer complementary solutions to existing transportation problems through logistical efforts and would be fully powered by new green energy sources, thus diminishing reliance on non-renewable energy sources.

Two prototype cargo airships were successfully built and tested at LaRC demonstrating their future role in transportation. Solar and wireless microwave power were able to provide all of the energy to propel and maneuver the prototypes, thus offering a platform for the new green energy sources being developed within NASA and the Department of Transportation.

Wireless power transmission technology in the X- and V-bands was shown to be sufficient to power a heavy load cargo airship with an electrical propulsion system. The results for these rectennas suggest their practical use as a power receiver for effectively using microwave energy to power a cargo airship, but higher frequency rectennas are needed to increase power capabilities.

Rhombohedral SiGe on c-plane sapphire has opened up the possibility of creating hundreds of new hybrid crystal structures between cubic semiconductors and trigonal crystals. Two material designs of rhombohedral SiGe, single-crystalline and highly twinned, have been demonstrated in the laboratory to have important applications in quantum well solar cells (photovoltaics) and high temperature thermoelectric materials, respectively. Current efforts are focused on improving the efficiency of rhombohedral SiGe beyond the theoretical limits of silicon photovoltaic cells and creating operational devices.

In the area of thermoelectric (TE) materials, the improvement in efficiency for the low to mid-temperature materials has been demonstrated in the laboratory. This is achieved by decorating Bi_2Te_3 and Ag_2Te grains with metallic nanoparticles in order to increase the ZT factor by increasing the electrical conductivity while decreasing the thermal conductivity. ZT is the figure of merit for these TE materials, which equates to an increase in efficiency.

All of these technologies are important to further the country's energy policy and progress in developing new energy sources for transportation through research and development. NASA LaRC has complete in-house fabrication and characterization facilities to push these technologies to their theoretical limits and commercial realization.

SECTION 13

REFERENCES

1. Payne, Sarah, Dutzik, Tony, and Figdor, Emily, “The High Cost of Fossil Fuels: Why America Can’t Afford to Depend on Dirty Energy,” Environment America Research & Policy Center, June 2009.
http://www.environmentamericacenter.org/sites/environment/files/reports/The-High-Cost-of-Fossil-Fuels_0.pdf Accessed 11 February 2013.
2. U.S. Energy Administration, *Annual Energy Review 2011*, Department of Energy, EIA–0384(2011), September 2012. <http://www.eia.gov/totalenergy/data/annual/pdf/aer.pdf> Accessed 11 February 2013.
3. Khoury, Gabriel A. and Gillet, J. David, *Airship Technology*, Cambridge University Press, Cambridge, UK, 1999.
4. Brown, William C., George, Roscoe H., and Heenan, Neil I., assignors to Raytheon Company, Lexington, Massachusetts, a corporation of Delaware, “Microwave to DC Converter,” U.S. Patent 3,434,678, filed 5 May 1965 and issued 25 March 1969.
<http://www.google.com/patents/US3434678> Accessed 11 February 2013.
5. Tesla, Nikola, “Apparatus for Transmission of Electrical Energy,” U.S. Patent No. 649,621, filed 19 February 1900 and issued 15 May 1900.
<http://www.google.com/patents/US649621> Accessed 11 February 2013.
6. Tesla, Nikola, “The Transmission of Electric Energy without Wires” *Electrical World and Engineer*, 5 March 1904. <http://www.teslauniverse.com/nikola-tesla-article-the-transmission-of-electrical-energy-without-wires> Accessed 11 February 2013.
7. Tesla, Nikola, *Experiments with Alternate Current of High Potential and High Frequency*, New York, Cosimo, Inc., 2007 (originally published in 1904).
8. Hull, Albert W., “The Effect of a Uniform Magnetic Field on the Motion of Electrons between Coaxial Cylinders,” *Physical Review*, Vol. 18, No. 1, July 1921, pp. 31–57.
<http://dx.doi.org/10.1103/PhysRev.18.31> Accessed 11 February 2013.
9. Heil, O. and Elders, J. J., “A New Wide-Range High Frequency Oscillator,” *Proceedings of the Institute of Radio Engineers*, Vol. 38, No. 6, June 1950, pp. 645–650.
<http://dx.doi.org/10.1109/JRPROC.1950.232800> Accessed 11 February 2013.
10. Brown, W. C., “Experiments Involving a Microwave Beam to Power and Position a Helicopter,” *Institute of Electrical and Electronics Engineers Transactions on Aerospace and Electronic Systems*, Vol. AES–5, No. 5, September 1969, pp. 692–702.
<http://dx.doi.org/10.1109/TAES.1969.309867> Accessed 11 February 2013.

11. U.S. Department of Energy, "Satellite Power System (SPS) Program Summary," DOE/ER-0022, December 1978.
<http://www.nss.org/settlement/ssp/library/1978DOESPS-ProgramSummary.pdf> Accessed on 11 February 2013.
12. Dressler, Alan, Ed., "Exploration and the Search for Origins: A Vision for Ultraviolet-Optical-Infrared Space Astronomy; Report of the *HST & Beyond* Committee," The Association of Universities for Research in Astronomy, Washington, D.C., 15 May 1996.
13. Choi, Sang H., Song, Kyo D., Golembiewski, Walter, Chu, Sang-Hyon, and King, Glen C., "Microwave Power for Smart Material Actuators," *Smart Material and Structures*, Vol. 13, No. 1, February 2004, pp. 38–48. <http://dx.doi.org/10.1088/0964-1726/13/1/005> Accessed on 11 February 2013.
14. Song, Kyo D., Yi, Won J., Chu, Sang-Hyon, and Choi, Sang H., "Microwave Driven THUNDER Materials," *Microwave and Optical Technology Letters*, Vol. 36, No. 5, 5 March 2003, pp. 331–333. <http://dx.doi.org/10.1002/mop.10757> Accessed on 11 February 2013.
15. Kim, Jaehwan, Yang, Sang Yeol, Song, Kyo D., Jones, Sean, and Choi, Sang H., "Performance Characterization of Flexible Dipole Rectennas for Smart Actuator Use," *Smart Material and Structures*, Vol. 15, No. 3, June 2006, pp. 809–815.
<http://dx.doi.org/10.1088/0964-1726/15/3/017> Accessed on 11 February 2013.
16. Payne, Joshua E., Song, Kyo D., Yang, Sang Y., Kim, Jae Hwan, Park, Yeonjoon, Choi, Sang H., "Wireless Power Transmission for Medical Applications," *Society of Photographic Instrumentation Engineers Conference Proceedings 7291: Nanosensors, Biosensors, and Info-Tech Sensors and Systems 2009*, 72910X, 31 March 2009.
<http://dx.doi.org/10.1117/12.816020> Accessed on 11 February 2013.
17. Yoon, Hargsoon, Williams, Frances, Song, Kyo D., Yang, Sang Y., Kim, Jae Hwan, Lee, Kunik, and Choi, Sang H., "Rectennas Performance Based on Substrates for Bio-medical Applications," *Society of Photographic Instrumentation Engineers Conference Proceedings 7646: Nanosensors, Biosensors, and Info-Tech Sensors and Systems 2010*, 76460U, 30 March 2010. <http://dx.doi.org/10.1117/12.847706> Accessed on 11 February 2013.
18. Lee, Uhn, Song, Kyo D., Park, Yeonjoon, Varadan, Vijay, and Choi, Sang H., "Perspective in Nano-neural Electronic Implant Wireless Power-feed and Sensory Control," *Journal of Nanotechnology in Engineering and Medicine*, Vol. 1, No. 2 (021007), 6 May 2010. <http://dx.doi.org/10.1115/1.4001413> Accessed on 11 February 2013.
19. Yoon, Hargsoon, Song, Kyo D., and Choi, Sang H., "Near Field Effects of Millimeter-wave Power Transmission for Medical Applications," *Society of Photographic Instrumentation Engineers Conference Proceedings 7980: Nanosensors, Biosensors, and Info-Tech Sensors and Systems 2011*, 798012, 15 April 2011.
<http://dx.doi.org/10.1117/12.880526> Accessed on 11 February 2013.

20. Corkish, R., Green, M. A., and Puzzer, T., "Solar Energy Collection by Antennas," *Solar Energy*, Vol. 73, No. 6, December 2002, pp. 395–401. [http://dx.doi.org/10.1016/S0038-092X\(03\)00033-1](http://dx.doi.org/10.1016/S0038-092X(03)00033-1) Accessed on 11 February 2013.
21. Brown, W. C., Dickinson, R. M., Nalos, E. J., and Ott, J. H., "Rectenna System Design," *The Final Proceedings of the Solar Power Satellite Program Review*, U.S. Department of Energy and National Aeronautics and Space Administration Satellite Power System Concept Development and Evaluation Program, Conf-800491, Lincoln, Nebraska, 22–25 April 1980, printed July 1980, pp. 328–331.
<http://www.nss.org/settlement/ssp/library/1981DOESPS-FinalProceedingsOfTheSolarPowerSatelliteProgramReview.pdf> Accessed on 12 February 2013.
22. Kim, Jaehwan, Yang, Sang-Yeol, Song, Kyo D., Jones, Sean, Elliott, James R., and Choi, Sang H., "Microwave Power Transmission Using a Flexible Rectenna for Microwave-powered Aerial Vehicles," *Smart Materials and Structures*, Vol. 15, No. 5, October 2006, pp. 1243–1248. <http://dx.doi.org/10.1088/0964-1726/15/5/012> Accessed on 12 February 2013.
23. Lorenz, Ralph D., "Flight Power Scaling of Airplanes, Airships, and Helicopters: Application to Planetary Exploration," *Journal of Aircraft*, Vol. 38, No. 2, March–April 2001, pp. 208–214. <https://www.lpl.arizona.edu/~rlorenz/flightpower.pdf> Accessed on 12 February 2013.
24. Liao, Lin and Pasternak, Igor, "A Review of Airship Structural Research and Development," *Progress in Aerospace Science*, Vol. 45, No. 4–5, May–July 2009, pp. 83–96. <http://dx.doi.org/10.1016/j.paerosci.2009.03.001> Accessed on 12 February 2013.
25. Hall, Jeffery L., Kerzhanovich, Viktor V., Jones, Jack A., Cutts, James A., Yavrouina, Andre A., Colozza, Antony, and Lorenz, Ralph D., "Titan Airship Explorer," *Aerospace Conference Proceedings*, 9–16 March 2002, Institute of Electrical and Electronics Engineers, Vol. 1, 2002, pp. 1-327–1-336.
<http://dx.doi.org/10.1109/AERO.2002.1036852> Accessed on 12 February 2013.
26. Prentice, Barry E., PhD, Cohen, Sharon, Duncan, Douglas B., Ed., *Airships to the Arctic, Symposium III, Sustainable Northern Transportation Proceedings*, 31 May to 2 June 2005, Winnipeg, MB, Canada.
http://www.airshipstothearctic.com/docs/pr/isopolar_aaiii.pdf Accessed on 12 February 2013.
27. Brown, W. C., Brown, "A Microwave Powered Orbital Industrial Park System," *Proceedings of the Eighth Princeton/American Institute of Aeronautics and Astronautics/Space Studies Institute Conference on Space Manufacturing 6: Nonterrestrial Resources, Biosciences, and Space Engineering*, 6–9 May 1987, Princeton, pp. 242–251. <http://ssi.org/ssi-conference-abstracts/space-manufacturing-6/> Accessed on 12 February 2013.

28. Yoo, Tae-Whan, Chang, Kai, "Theoretical and Experimental Development of 10 and 35 GHz Rectennas," *Institute of Electrical and Electronics Engineers Transactions on Microwave Theory and Techniques*, Vol. 40, No. 6, June 1992, pp. 1259–1266. <http://dx.doi.org/10.1109/22.141359> Accessed on 12 February 2013.
29. McSpadden, James O., Fan Lu, and Chang, Kai, "Design and Experiments of a High-conversion-efficiency 5.8-GHz Rectenna," *Institute of Electrical and Electronics Engineers Transactions on Microwave Theory and Techniques*, Vol. 46, No. 12, December 1998, pp. 2053–2060. <http://dx.doi.org/10.1109/22.739282> Accessed on 12 February 2013.
30. Chiou, Hwann-Kaeo and Chen, I-Shan, "High-efficiency Dual-band On-chip Rectenna for 35- and 94GHz Wireless Power Transmission in 0.13- μ m CMOS Technology," *Institute of Electrical and Electronics Engineers Transactions on Microwave Theory and Techniques*, Vol. 58, No. 12 Part 1, December 2010, pp. 3598–3606. <http://dx.doi.org/10.1109/TMTT.2010.2086350> Accessed on 12 February 2013.
31. Shockley, William and Queisser, Hans J., "Detailed Balance Limit of Efficiency of $p - n$ Junction Solar Cells," *Journal of Applied Physics*, Vol. 32, No. 3, March 1961, pp. 510–519. <http://dx.doi.org/10.1063/1.1736034> Accessed on 12 February 2013.
32. Green, Martin A., Emery, Keith, Hishikawa, Yoshihiro, and Warta, Wilhelm, "Solar Cell Efficiency Tables (Version 33)," *Progress in Photovoltaics: Research and Applications*, Vol. 17, No. 1, January 2009 (First Published 17 December 2008), pp. 85–94. <http://dx.doi.org/10.1002/pip.880> Accessed on 12 February 2013.
33. Zhao, Jianhua, Wang, Aihua, Green, Martin A., and Ferrazza, Francesca, "19.8 % Efficient 'Honeycomb' textured multicrystalline and 24.4% monocrystalline silicon solar Cells," *Applied Physics Letters*, Vol. 73, No. 14, 5 October 1998. <http://dx.doi.org/10.1063/1.122345> Accessed on 12 February 2013.
34. Park, Yeonjoon, Choi, Sang H., King, Glen C., and Elliott, James R., assignors to the National Aeronautics and Space Administration, "Hybrid Bandgap Engineering for Super-hetero-epitaxial Semiconductor Materials, and Products Thereof," U.S. Patent 8,226,767, filed 20 October 2008 and issued 24 July 2012. <http://www.google.com/patents/US8226767> Accessed on 12 February 2013.
35. Park, Yeonjoon, King, Glen C., and Choi, Sang H., "Rhombohedral epitaxy of Cubic SiGe on Trigonal c -Plane Sapphire," *Journal of Crystal Growth*, Vol. 310, No. 11, 15 May 2008, pp. 2724–2731. <http://dx.doi.org/10.1016/j.jcrysgro.2008.02.010> Accessed on 12 February 2013.
36. Park, Yeonjoon, Choi, Sang H., King, Glen C., and Elliott, James R., assignors to the National Aeronautics and Space Administration, "Rhombohedral Cubic Semiconductor Materials on Trigonal Substrate with Single Crystal Properties and Devices Based on Such Materials," U.S. Patent 8,257,491, filed 20 October 2008 and issued 4 September 2012. <http://www.google.com/patents/US8257491> Accessed on 15 February 2013.

37. Park, Yeonjoon, Choi, Sang H., and King, Glen C., “Epitaxial Growth of Cubic Crystalline Semiconductor Alloys on Basal Plane of Trigonal or Hexagonal Crystal,” U.S. Patent 7,906,358, filed 20 October 2008 and issued 15 March 2011.
<http://www.google.com/patents/US7906358> Accessed on 15 February 2013.
38. Park, Yeonjoon, Choi, Sang H., King, Glen C., and Elliott, James R., assignors to the National Aeronautics and Space Administration, “Method of Generating X-ray Diffraction Data for Integral Detection of Twin Defects in Super-hetero-epitaxial Materials,” U.S. Patent 7,558,371 filed 20 October 2008 and issued 7 July 2009.
<http://www.google.com/patents/US7558371> Accessed on 15 February 2013.
39. Park, Yeonjoon, Choi, Sang H., King, Glen C., Elliott, James R., and DiMarcantonio, A L., assignors to the National Aeronautics and Space Administration, “X-ray Diffraction Wafer Mapping Method for Rhombohedral Super-hetero-epitaxy,” U.S. Patent 7,769,135, filed 20 October 2008 and issued 3 August 2010.
<http://www.google.com/patents/US7769135> Accessed on 15 February 2013.
40. Kim, Hyun Jung, Choi, Sang H., Bae, Hyung-Bin, and Lee, Tae Woo, “Transmission Electron Microscopy (TEM) Sample Preparation of $\text{Si}_{1-x}\text{Ge}_x$ in *c*-Plane Sapphire Substrate,” NASA/TM–2012–217597, August 2012.
<http://ntrs.nasa.gov/archive/nasa/casi.ntrs.nasa.gov/20120013304.pdf> Accessed on 15 February 2013.
41. d’Aragona, F. Secco, “Dislocation Etch for (100) Planes in Silicon,” *Journal of the Electrochemical Society*, Vol. 119, No. 7, 1972, pp. 948–951.
<http://dx.doi.org/10.1149/1.2404374> Accessed on 15 February 2013.
42. Golikova, O. A., Moizhes, B. Y., and Stil’bans, L. S., “Hole Mobility of Germanium as a Function of Concentration and Temperature,” *Soviet Physics, Solid State*, Vol. 3, April 1962, pp. 2259–2265.
43. Jacoboni, Carlo, Canali, C., Ottaviani, G., and Quaranta, A. Alberigi, “A Review of Some Charge Transport Properties of Silicon,” *Solid-State Electronics*, Vol. 20, No. 2, February 1977, pp. 77–89. [http://dx.doi.org/10.1016/0038-1101\(77\)90054-5](http://dx.doi.org/10.1016/0038-1101(77)90054-5) Accessed on 15 February 2013.
44. Yang, J., Hogan, T. P., Funahashi, R., and Nolas, G. S., Ed., “Materials and Technologies for Direct Thermal-to-Electric Energy Conversion, 2005 Fall Materials Research Society Fall Meeting,” MRS Symposium Proceedings, Vol. 886, Boston, Fall 2005.
45. Rowe, D. M., Ed., *Thermoelectrics Handbook: Macro to Nano*, Boca Raton, Florida, CRC Press, 2006.
46. Vining, C. B., “Summary Report on ICT ’99—The 18th International Conference on Thermoelectrics,” ZT Services, Inc., Auburn, Alabama, 1999.
<http://cvining.com/system/files/Vining-ETS99-Pardubice-1999.pdf> Accessed on 15 February 2013.

47. *Landolt-Bornstein: Numerical Data and Functional Relationships in Science and Technology*, Vol. 17a, edited by K.-H. Hellwege et al., Springer, Berlin, 1982, p. 453.
48. Stohr, H. and Klemm, W., *Zeitschrift für Anorganische und Allgemeine Chemie (Journal for Inorganic and General Chemistry)*, Vol. 241, 1954, p. 305.
49. Kawamoto, Hiroshi, “R&D Trends in High Efficiency Thermoelectric Conversion Materials for Waste Heat Recovery,” *Science & Technology Trends, Quarterly Review*, No. 30, January 2009, pp. 54–69.
<http://www.nistep.go.jp/achiev/ftx/eng/stfc/stt030e/qr30pdf/STTqr3004.pdf> Accessed on 19 February 2013.
50. Kribus, Abraham, “Thermal Integral Micro-generation Systems for Solar and Conventional Use,” *Journal of Solar Energy Engineering*, Vol. 124, No. 2, May 2002, pp. 189–197. <http://dx.doi.org/10.1115/1.1464879> Accessed on 19 February 2013.
51. U.S. Energy Information Administration, *Annual Energy Outlook 2011 with Projections to 2035*, DoE/EIA–0383, April 2011.
<http://www.eia.gov/forecasts/archive/aeo11/pdf/0383%282011%29.pdf> Accessed on 19 February 2013.
52. Snyder, G. Jeffrey and Toberer, Eric S., “Complex Thermoelectric Materials,” *Nature Materials*, Vol. 7, No. 2, February 2008, pp. 105–114.
<http://dx.doi.org/10.1038/nmat2090> Accessed on 19 February 2013.
53. Hochbaum, Allon I., Chen, Rekun, Delgado, Raul Diaz, Liang, Wenjie, Garnett Eric C., Najarian, Mark, AMajumdar, Arun, and Yang, Peidong, “Enhanced Thermoelectric Performance of Rough Silicon Nanowires,” *Nature*, Vol. 451, No. 7175, 10 January 2008, pp. 163–167. <http://dx.doi.org/10.1038/nature06381> Accessed on 19 February 2013.
54. Pattamatta, Arvind and Madnia, Cyrus K., “Modeling Heat Transfer in Bi_2Te_3 – Sb_2Te_3 Nanostructures,” *International Journal of Heat and Mass Transfer*, Vol. 52, No. 3–4, January 2009, pp. 860–869. <http://dx.doi.org/10.1016/j.ijheatmasstransfer.2008.09.004> Accessed on 19 February 2013.
55. Kim, Hyun Jung, King, Glen C., Park, Yeonjoon, Lee, Kunik, and Choi, Sang H., “Thermoelectric Performance Enhancement by Surrounding Crystalline Semiconductors with Metallic Nanoparticles,” *Ninth Annual International Energy Conversion Engineering Conference*, 31 July–03 August 2011, San Diego, California, AIAA 2011–5982, 2011. <http://dx.doi.org/10.2514/6.2011-5982> Accessed on 19 February 2013.
56. Deng, Yuan, Nan, Ce-Wen, and Guo, Lin, “A Novel Approach to Bi_2Te_3 Nanorods by Controlling Oriented Attachment,” *Chemical Physics Letters*, Vol. 383, No. 5–6, 15 January 2004, pp. 572–576. <http://dx.doi.org/10.1016/j.cplett.2003.11.090> Accessed on 19 February 2013.

57. Zhao, X. B., Ji, X. H., Zhang, Y. H., Zhu, T. J., Tu, J. P., and Zhang, X. B., “Bismuth Telluride Nanotubes and the Effects on the Thermoelectric Properties of Nanotube-containing Nanocomposites,” *Applied Physics Letters*, Vol. 86, No. 6, 3 February 2005, pp. 062111-1–3. <http://dx.doi.org/10.1063/1.1863440> Accessed on 19 February 2013.
58. Franz, R. and Wiedemann, G., “Ueber die Wärme-Leitungsfähigkeit der Metalle,” *Annalen der Physik*, Vol. 165, No. 8, 1853, pp. 497–531. <http://dx.doi.org/10.1002/andp.18531650802> (published online 15 March 2006) Accessed on 19 February 2013.
59. Kim, Hyun-Jung, Choi, Sang Hyouk, King, Glen C., Park, Yeonjoon, and Lee, Kunik, “Method of Creating Micro-scale Silver Telluride Grains Covered with Bismuth Telluride,” U.S. Patent Number 2012/0225513 A1, filed 5 March 2012 and issued 6 September 2012. <http://www.google.com/patents/US20120225513> Accessed on 19 February 2013.
60. Aliev, S. A., “Hysteresis in Ag₂Te Near and Within the Phase Transition Region,” *Semiconductors*, Vol. 38, No. 7, July 2004, pp. 796–799 (translated from *Fizika i Tekhnika Poluprovodnikov*, Vol. 38, No. 7, 2004, pp. 830–833). <http://dx.doi.org/10.1134/1.1777603> Accessed on 19 February 2013.
61. Borca-Tasciuc, D.-A., Chen, G., Prieto, A., Martin-Gonzalez, M. S., Stacy, A., Sands, T., Ryan, M. A., and Fleurial, J. P., “Thermal Properties of Electrodeposited Bismuth Telluride Nanowires Embedded in Amorphous Alumina,” *Applied Physics Letters*, Vol. 85, No. 24, 13 December 2004, pp. 6001–6003. <http://dx.doi.org/10.1063/1.1834991> Accessed on 19 February 2013.
62. Kim, H. J., Lee, J., Varadan, V. K., and Choi, S. H., “Printed Thermoelectric Generator for Hybrid Tandem Photovoltaic / Thermoelectric Device,” *Bentham Science Journal of Recent Patents on Space Technology*, Vol. 3, No. 2, 2013, pp.132–151. <http://benthamscience.com/journal/abstracts.php?journalID=rpst&articleID=115059> Accessed on 5 May 2014.

REPORT DOCUMENTATION PAGE				Form Approved OMB No. 0704-0188	
<p>The public reporting burden for this collection of information is estimated to average 1 hour per response, including the time for reviewing instructions, searching existing data sources, gathering and maintaining the data needed, and completing and reviewing the collection of information. Send comments regarding this burden estimate or any other aspect of this collection of information, including suggestions for reducing this burden, to Department of Defense, Washington Headquarters Services, Directorate for Information Operations and Reports (0704-0188), 1215 Jefferson Davis Highway, Suite 1204, Arlington, VA 22202-4302. Respondents should be aware that notwithstanding any other provision of law, no person shall be subject to any penalty for failing to comply with a collection of information if it does not display a currently valid OMB control number.</p> <p>PLEASE DO NOT RETURN YOUR FORM TO THE ABOVE ADDRESS.</p>					
1. REPORT DATE (DD-MM-YYYY) 01-04 - 2014		2. REPORT TYPE Technical Memorandum		3. DATES COVERED (From - To)	
4. TITLE AND SUBTITLE Feasibility Study of Cargo Airship Transportation Systems Powered by New Green Energy Technologies			5a. CONTRACT NUMBER		
			5b. GRANT NUMBER		
			5c. PROGRAM ELEMENT NUMBER		
6. AUTHOR(S) Skuza, Jonathan R.; Park, Yeojoon; Kim, Hyun Jung; Seaman, Shane T.; King, Glen C.; Choi, Sang H.; Song, Kyo D.; Yoon, Hargsoon; Lee, Kunik			5d. PROJECT NUMBER		
			5e. TASK NUMBER		
			5f. WORK UNIT NUMBER 833011.02.07.89Z5.13		
7. PERFORMING ORGANIZATION NAME(S) AND ADDRESS(ES) NASA Langley Research Center Hampton, VA 23681-2199				8. PERFORMING ORGANIZATION REPORT NUMBER L-20307	
9. SPONSORING/MONITORING AGENCY NAME(S) AND ADDRESS(ES) National Aeronautics and Space Administration Washington, DC 20546-0001				10. SPONSOR/MONITOR'S ACRONYM(S) NASA	
				11. SPONSOR/MONITOR'S REPORT NUMBER(S) NASA/TM-2014-218241	
12. DISTRIBUTION/AVAILABILITY STATEMENT Unclassified - Unlimited Subject Category 33 Availability: NASA CASI (443) 757-5802					
13. SUPPLEMENTARY NOTES					
14. ABSTRACT The development of transportation systems that use new and sustainable energy technologies is of utmost importance due to the possible future shortfalls that current transportation modes will encounter because of increased volume and costs. The introduction and further research and development of new transportation and energy systems by materials researchers at the National Aeronautics and Space Administration (NASA) Langley Research Center (LaRC) and the Department of Transportation are discussed in this Technical Memorandum. In this preliminary study, airship concepts were assessed for cargo transportation using various green energy technologies capable of 24-hour operation (i.e., night and day). Two prototype airships were successfully constructed and tested at LaRC to demonstrate their feasibility: one with commercially available solar cells for operation during the daytime and one with microwave rectennas (i.e., rectifying antennas) developed in-house for night-time operation. The test results indicate the feasibility of a cargo transportation airship powered by new green energy sources and wireless power technology. Future applications will exploit new green energy sources that use materials and devices recently developed or are in the process of being developed at LaRC. These include quantum well SiGe solar cells; low, mid-, and high temperature thermoelectric modules; and wireless microwave and optical rectenna devices. This study examines the need and development of new energy sources for transportation, including the current status of research, materials, and potential applications.					
15. SUBJECT TERMS Air cargo; Airships; Energy technology; Solar cells; Transportation					
16. SECURITY CLASSIFICATION OF:			17. LIMITATION OF ABSTRACT	18. NUMBER OF PAGES	19a. NAME OF RESPONSIBLE PERSON
a. REPORT	b. ABSTRACT	c. THIS PAGE			STI Help Desk (email: help@sti.nasa.gov)
U	U	U	UU	102	19b. TELEPHONE NUMBER (Include area code) (443) 757-5802